SYNTHESIS, PROCESSING AND MORPHOLOGICAL PROPERTIES OF HIGHLY POROUS SUPERCRITICALLY DRIED MESOPOROUS SILICON NANOSTRUCTURES FOR DRUG DELIVERY APPLICATIONS

By **Elida Nekovic**

A thesis submitted to The University of Birmingham for the degree of DOCTOR OF PHILOSOPHY

UNIVERSITY OF BIRMINGHAM

Nanoscale Physics Research Laboratory

School of Physics and Astronomy

University of Birmingham

Birmingham B15 2TT, UK.

Acknowledgements

My PhD journey has marked my last 4 years of life. It has been an incredible experience and taught me a lot about both science and life in general. Through my PhD programme, I learnt a lot about porous semiconductors overall. I made my very first silicon aerocrystal with the highest pore volume reported up-to-date. Furthermore, I was so lucky to get a chance to work with one of the biggest World's expert on porous silicon, Professor Leigh Canham. I had a chance to attend a few conferences, saw beautiful places and published several papers.

First and foremost I would like to thank my supervisor Professor Leigh Canham for allowing me to work with porous silicon. You have been supportive and keen on transferring me your knowledge since day one working with you. You have taught me to be patient and to keep working hard and learning more and more. I am also extremely thankful for very useful meetings with you and for all your time. I used to come to your office multiple times during the day to ask some questions and to show you our amazing porous silicon membranes. Thank you for all your patience with me, listening to me all the time and for providing me with very useful and good feedbacks. Thanks for allowing me to attend the PSST conference which has been one of the best parts of my PhD. Thank you for all your time and help in writing the publications and I understand it wasn't easy to deal with me. All in all, I am extremely grateful for having a chance to meet you. You helped me to progress a lot as a scientist and as a person. There are no words that can describe how grateful I am.

My work could not be carried out without the support of Catherine Storey, an experimental officer in our group. I cannot imagine my PhD days without Catherine. She has been the most understanding and helpful person all the time. We used to work long hours in the lab. She taught me experimental techniques needed for my projects. She helped me with my questions, queries as well as the papers and thesis writing. Thank you for all the dedicated time to me. Thanks for amazing Christmas gift you used to make for me. Thank you for being so nice and always available to me. You have been my shining star in this tunnel called PhD. I am so glad I made it to the end but nothing would be the same without you.

I would like to thank my supervisor, Dr Andre Kaplan, for allowing me to choose my PhD project and what I feel more comfortable with. Thanks for your help and time. Thanks for providing me needed equipment for the lab. Enormous thanks for sorting out my extension. Thanks for being patient and willing to help with my papers. Many thanks for providing me with feedback on this thesis.

Another acknowledgement goes to our Head of the group, Dr Wolfgang Theis. Many thanks for all your understanding and needed help. Thanks for the feedback on papers and is a co-author. Thanks for standing-out for all of the PhD students from our group. It means a lot to us.

I would also like to acknowledge all my colleagues and friends from my group. Thanks for your conversations and some nice occasional events we used to have. Thanks to Rihan Wu, Jack Collins and Dler Kareem for sharing office with me, having nice food and our tasty coffee. Thanks to Megan Grose for being nice friend, bringing me to lunches with the group from the beginning. Thanks for nice dinner rituals we had. I hope you will finish your PhD successfully. Thanks to Alexander Pattison for being very helpful and friendly to me. Wish you success in your career.

Thanks to my dear friend Suzanna Freer (Suzie), PhD student at the University of Birmingham, Metamaterials group, for being the most supportive friend I have. I remember the days we started doing teaching together. Later we started to play squash, tennis, go running together all the time. Your friendship means a lot to me and I would never forget how nice you were to me. Thanks for leaving nice cookies on my office desk as I used to stay late in the lab. Thanks for the coffee and lunch breaks-they were very relaxing and nice. As you are a PhD student yourself, I wish you all success in completing your PhD.

I would like to thank my family, my dad Erdan, mum Ajkuna and sisters Emina (MSc of Electrical Engineering) and Ajla (BSc of Electrical Engineering) for the huge support and all love provided during my PhD. Thanks for always believing and me and giving me wind to my back. You are the reason I believed that dreams can come true one day if you truly believe and if you work constantly in achieving them. Voli vas puno vasa doktorica!

Thanks to my aunt and uncle, Sanja and Senad Kozar for the kind support. Thanks to my cousins Ines (Doctor of Microbiology), Dado (Bsc of Sport Sciences) and Danis (Student) for great times in Luxembourg when I used to come for a shorter trip as a break from PhD.

Thanks to my friend Dr Sasa Gazibegovic for her advice and nice times during my PhD. Thanks for supporting me in my scientific beginnings. I hope we forever keep in touch. You have proved that everything is possible if we really want it.

Thanks to Olivera Vukovic for nice conversations and fun during my PhD. Thanks for the great time in the Netherlands and Belgium during my trip back in 2019.

Thanks to my friends from Bosnia: Arnela H., Jelena, Arnela S. and Amina for our friendship through all these years. Also to Jasmina and Nedzmija for our conversations and sharing interesting things from day to day life. Thanks to Estela for being there too for me.

A big thanks to my sister's best friend Dr Adriana Lipovac, Professor at the University of Dubrovnik for being so nice and supportive all the time. Thanks for listening to me. I really appreciate it.

Many thanks to my dear friend Dr Emina Hadziosmanovic for being so nice to me since I first time came to the UK. Thank you very much for all amazing times, trips we had together with Edina. I wish we stay friends forever.

Many thanks to my Physics teacher from high school Aida Agic for teaching me Physics with so much enthusiasm. I started to love Physics because of her classes. I wish you all the best in your career and I hope we stay in touch always.

Last but not the least, the biggest thanks to my Liam Landers for being my support and for coping with me. I know that I am not an easy-going person sometimes and that I worked long hours and weekends. Thanks for listening to my stories about work all the time. Thanks for the great memories travelling to different places. Thanks for playing tennis and going running, hiking with me. Thanks for great and delicious food during my extremely busy times. You have been the best!

Abstract

Over the last few decades, the interest in porous semiconductors increased dramatically. Porous silicon was discovered accidentally in the 1950s by Uhlir at the Bell Laboratories. Since then, pSi has been of focus for multiple applications, such as drug delivery, photonics, gas sensing, cosmetics industry, solar cells etc. This thesis focuses on the fabrication, processing and characterisation of highly porous silicon nanostructures with a possible application in drug delivery.

The thesis is ordered in such a manner that after introducing the motivation and all the background topics (chapter 1) , the reader is taken through the common sequence of material fabrication (chapter 2), processing (chapters 2& 3) and then characterization (chapter 4).

Chapter 1 gives an overview and background information about the topic. It is divided into separate sections named Fabrication, characterisation, properties of porous silicon, and applications.

Chapter 2 provides the results of Fabrication, processing and characterisation of the highly porous silicon membranes. This chapter is based on the author's three publications. The main achievements were the highest reported pore volume of free-standing porous silicon membranes reported up-to-date via optimised electrochemical anodisation of silicon wafers and supercritical drying; the first direct comparison of two processing techniques that generate particles (milling and sonication); and the first demonstration of how sedimentation can be used to tune microparticle size distribution.

Chapter 3 focuses on the importance of drying and supercritical fluid drying as the main processing technique utilized in this doctoral thesis. This specific type of drying avoids the capillary forces that can cause the pore collapse. Instead, the material is brought to a critical point (pressure and temperate) avoiding the evaporation of ethanol and further flushes using supercritical CO_2.

Chapter 4 describes in more detail the characterisation techniques used to investigate the fabricated structures. Fabricated porous silicon structures were characterised using several techniques, such as gas adsorption analysis, scanning electron microscope, particle sizing employing laser diffraction, gravimetric method.

Chapter 5 summarizes all the previous chapters as well as providing an outlook of possible future work. The proposed work includes electrochemical anodisation and supercritical drying of n-wafers as well as the pore impregnation using polymers in order to preserve the pore volume/porosity and surface area during the processing techniques.

Chapter 6 consists of Appendices regards standard operating procedures (SOPs).

Guidelines for the reader: Please note that some details on characterisation techniques and experimental methods in Chapter 4 would be helpful to read before or whilst reading Chapter 2 in order to provide a complete understanding of relevant topics.

List of Figures

Figure 1 (a) Routes to porous silicon via solid silicon: top-down. (b) Routes to porous silicon via chemical conversion: bottom-up. Adapted from (Canham 2014). 24

Figure 2 Figure Possible morphologies of different pSi layers (Korotcenkov 2010). 25

Figure 3 Types of anodisation cells: (a) lateral anodisation cell, (b) single-tank cell and (c) double-tank cell. Adapted from (Canham 1997). 28

Figure 4 (a) Double-tank anodisation cell. (b) Personal protective equipment PP(lab coat, safety glasses, face visor, apron, gloves, HF monitor) for work with HF. 30

Figure 5 SEM images of microporous, mesoporous and macroporous structures, respectively 34

Figure 6 Varied “physical colours” from ultrathin single layers of stain-etched mesoporous silicon (LHS-A. Loni unpublished 2009) and anodised mesoporous silicon photonic crystals (RHS-Gooding Group, Univ. New South Wales, Australia http://www.rsc.org/Publishing/ChemTech/Volume/ 2009/02/biosensors.asp) 39

Figure 7 TEM images of ultrahigh porosity Si structures (Canham 1994). 42

Figure 8 (a) Hysteresis loops from gas adsorption-desorption (IUPAC classification. (b) Schematic view of the pore morphology effect that give rise to H2 hysteresis curve (Thommes, 2010). 45

Figure 9 Process flow for electrochemically etched (porosified) silicon wafers with indicated structures fabricated and processed in this project. Adapted from (Canham 2014).....46

Figure 10 Shrinkage and crack development in a highly porous silicon film during air-drying, as revealed by sequential wide-field photoluminescence imaging (Mason et al. 2002) (Canham 2014). 48

Figure 11 Furnace used for oxidising porous silicon samples. 51

Figure 12 Methods for loading mesoporous materials.(Lehto et al. 2014).....57

Figure 13 A schematic of sensor fabrication processes. (a) Electrochemical anodisation setup used for fabrication of porous silicon substrate. (b) RF-magnetron sputtering setup used to deposit active layer of sensing electrode. 65

Figure 14 Optical images of Si wafer (thickness of 650 microns) and membranes of varying porosity but the constant thickness of 55 microns. (a) 0% (bulk Si) (b) 84% (c) 87% (d) 90% (e)

93%. The images (b-e) are from an anodized membrane of 81% porosity that was etched in 10% ethanoic HF for increasing periods of 1,2,3 and 5 hours, respectively. 74
Figure 15 Optical images of an ultrahigh porosity membrane (porosity 93%, thickness 55 microns) during in-situ etching in 10% HF for (a) 2hrs and (b) 5hrs.....75
Figure 16 Cracking and shrinking investigated via different magnifications used HRSEM plan view image of the upper face of a 91% porosity membrane (UOB30) subjected to air-drying via ethanol evaporation, (a) 1500 x magnification and (b) 500 x magnification.....75
Figure 17 Isotherms for air-dried (AD) structure and its supercritically-dried (SCD) equivalent of UoB 20. 77
Figure 18 Pore size distributions (incremental pore volume) for air-dried (AD) structure and its supercritically-dried (SCD) equivalent of UoB 20.....77
Figure 19 HRSEM plan view image of SCD UoB 20 membrane. 78
Figure 20 HRSEM plan view image of SCD UoB 30 membrane. 78
Figure 21 HRSEM cross-sectional images of SCD UoB 20 and UoB 60/61 membranes. 79
Figure 22 UoB 22/23/25 particle size distribution after 30 minutes USF or 1 minute BM. 90
Figure 23 Pore volume/pore size distribution in SCD pSi (Sample UoB 102) during repeated capillary condensation/evaporation (0-4 soak/dry cycles). 92
Figure 24 Graphical abstract consisting of the schematic diagram of the experimental procedure and optical image of individual UoB 101 samples during different sedimentation times in water. 100
Figure 25 Particle Size Distribution of air-dried UoB 101 for sedimentation times from 0 to 120 h. 101
Figure 26 The particle size distribution of SCD material UoB 99 before and after 2 hours sedimentation.....102
Figure 27 Phase diagram of water in (a) P-T plane and (b) P-V plane. (C.P. is an abbreviation for critical point) (Arai 2002).....111
Figure 28 Schematic diagram of SFC setup (Arai 2002).....113
Figure 29 Extraction procedure using supercritical carbon dioxide.....115
Figure 30 Scanning electron microscopy observation of 5-µm-thick p^+ type porous silicon layers of ~90% porosity after evaporation of different liquids: (a) water, (b) water plus surfactant (TACI), and (c) pentane; (d) exhibits a 20-µm-thick p^+ type PS layer ~porosity of 90% dried with pentane (Belmont 1996). 117

Figure 31 The phase diagram of carbon dioxide; a supercritical solvent (Canham 2014).....119
Figure 32 Supercritical dryers, (a) benchtop system (Quorum Technologies Ltd, UK) for processing stain-etched porous Si powders, (b) benchtop system (Quorum Technologies Ltd, UK) for processing an anodized 150 mm diameter silicon wafer, (c) cleanroom-compatible automated multiwafer system (Tousimis Corp., USA) (Canham 2014). 120
Figure 33 Fill level of a chamber. (From K850 Quorum Technologies Standard Operating Procedure). 121
Figure 34 Critical thickness as a function of porosity for water, ethanol and pentane. 129
Figure 35 Sample chamber of Micromeritics 3020 Tristar analyser. 129
Figure 36 Nitrogen adsorption isotherms for p+ porous silicon membranes. (a) Air-dried pSi and (b) supercritically-dried pSi. 131
Figure 37 Pore volume vs. pore diameter for p+ porous silicon membranes. (a) Air-dried pSi and (b) supercritically-dried pSi. 134
Figure 38 (a) Optical microscope vs. electron microscope (Goldestein et al. 2003). 137
Figure 39 High-Resolution SEM microscope. Philips XL30 ESEM-FEG microscope. 140
Figure 40 A plan view image of a pSi membrane BN21-R1270 R1283 etched for 80 mins...142
Figure 41 SEM image of sample UoB 20, showing a pore directionality. 143
Figure 42 Plan view image of porous silicon membrane and pore size analysis measurements. 144
Figure 43 A cross-section SEM image of porous silicon membrane UoB 20 145
Figure 44 A cross-sectional SEM image of the sample UoB 20.....147
Figure 45 Pore volume vs. pore diameter for p+ UoB 41 porous silicon membranes. (a & c) Air-dried pSi and (b & d) supercritically-dried pSi. 151
Figure 46 SEM image of the pSi membrane cractks during air-drying. 152
Figure 47 Plan view SEM image of the sample named UoB 41 152
Figure 48 Images from each processing step. 154
Figure 49 A graphical representation of the Malvern Mastersizer 2000. Identified features include (1) an Optical bench, (2) One or more sample dispersion units, and a (3) Computer system 158
Figure 50 Optical bench components. 159
Figure 51 An example of plot Volume (%) vs. particle diameter (um) from Mastersizer 2000.....163

Figure 52 Scattering efficiencies for pSi in KBr with particles sizes: 100 nm, 300 nm, 500 nm, 700 nm and 1 um 165
Figure 53 Absorption efficiencies for pSi in KBr with particles sizes: 100 nm, 300 nm, 500 nm, 700 nm and 1 um 165

List of Tables

Table 1 Wet etching routes of pSi formation. Adapted from (Canham 2014). Bold text in Table 1, marked with an asterisk denotes the main fabrication technique used in this doctoral thesis, which proceeds on the next section. References from this table can be found in the Handbook of porous silicon, ed. by Leigh Canham, (2014). 26

Table 2 Applications and the corresponding fabrication techniques of the membranes. References from this table can be found in the Handbook of porous silicon, ed. by Leigh Canham, (2014). 37

Table 3 Reported pore volume (porosity) of pSi values up-to-date. References from this table can be found in the Handbook of porous silicon, ed. by Leigh Canham (2014). 40

Table 4 The reported surface area of pSi values up-to-date. References from this table can be found in the Handbook of porous silicon, ed. by Leigh Canham (2014). 41

Table 5 Drying techniques survey. Adapted from (Canham 2014). References from this table can be found in the Handbook of porous silicon, ed. by Leigh Canham (2014). 49

Table 6 Table of relevant pSi properties required for some of the pSi applications. References from this table can be found in the Handbook of porous silicon, ed. by Leigh Canham (2014). 53

Table 7 Application areas of porous silicon. Adapted from (Canham 2014). 54

Table 8 A set of five AD vs. SCD pSi membranes. 76

Table 9 Processing times & yield data for generating nanoparticles from pSi membranes. SE: Standard Etching, PE: Perforation Etching, SCD: Supercritical Drying, AD: Air Drying, BM: Ball Milling, USF: Ultrasonic Fracture. 83

Table 10 Particle sizing data of SCD sample (UoB 99) after 1 min BM. UoBXX values are wafer batch codes representing distinct anodisation runs at the University of Birmingham (UoB). The d value represents particle diameter in microns, and the values shown in the table refer to the cumulative volume of particles below this size as a percentile. 86

Table 11 Degradation in surface area and porosity of SCD (UoB 99) & AD (UoB 100) samples before and after BM. Membrane thickness of 163 µm (AD material) 196-206 µm (SCD material). 86

Table 12 Pore characteristics of pSi material UoB 98. Membrane thickness of 182 µm. 87

Table 13 Particle sizing data of UOB 20. 87
Table 14 UoB20 - Comparison of pore characteristics. Membrane thickness of 195 µm. 88
Table 15 Particle sizing data of UoB 22/23/25 - 15A, 60 minutes. Membrane thickness: 190 µm, 187 µm &183 µm respectively. Membranes pooled together. 89
Table 16 Pore characteristics of UoB 22/23/25. 89
Table 17 Degradation in surface area and porosity of SCD pSi during repeated capillary condensation. 91
Table 18 Particle size range, settling velocity and settling time for different types of particles from prior sedimentation studies and the current study. 96
Table 19 Stokes' Law calculations of settling times for solid and porous silicon microparticles in water and ethanol. (maximum sedimentation distance s_d=5 cm as shown in Figure 31). .99
Table 20 Pore volume/porosity, surface area and mean pore size values for air-dried (AD) pSi UoB 101 and supercritically-dried pSi UoB 99, before and after ball milling (BM). 99
Table 21 Particle sizing and yield of pSi for air-dried UoB 101 after sedimentation over varying times. The d value represents particle diameter in microns and the values are shown in the table refer to the cumulative volume of particles below this size as a percentile. 100
Table 22 Particle sizing and yield of pSi data for supercritically-dried UoB 99 is presented in the table above. 101
Table 23 Comparison of gases, supercritical fluids and liquids. Adapted from (Zhang 2014). 112
Table 24 Calculated data of critical thickness for water, ethanol and pentane. 124
Table 25 Gas adsorption and gravimetric data of sample code UoB 40 supercritically dried (SCD) membranes and their air-dried (AD) equivalents. The thickness of the sample is 200 µm. 133
Table 26 Details about Optical microscope vs. electron microscope. Adapted from the (Website 6). 137
Table 27 Transmission electron microscope vs. Scanning electron microscope. 138
Table 28 BET analysis of the sample with identification code BN21 R1270-R1283 which was SEM imaged above. 142
Table 29 BET analysis of sample code UoB 20, SEM imaged. 143
Table 30 Thickness measurements of sample code UoB 20 obtained by ImageJ software. .146

Table 31 Gravimetric and Gas adsorption (BET) data of the sample UoB 41 which was subsequently used in JMicrovision 1.2.7. analysis of average pore diameter and porosity. 150
Table 32 Analysis data of the sample UoB 41 achieved by Software JMicrovision 1.2.7.....155
Table 33 Obscuration range notes and a relevant graph colour explained. 160
Table 34 Additional information about particle sizer (Mastersizer 2000). 167

List of Abbreviations

AD	Air-drying
BET	Brunauer–Emmett–Teller
BJH	Barrett-Joyner-Halenda
EDX	Energy Dispersive X-ray spectroscopy
HF	Hydrofluoric acid
PPE	Personal protective equipment
pSi	Porous silicon
SCF	Supercritical fluid
SCD	Supercritical drying
SEM	Scanning Electron Microscope
STEM	Scanning Transmission Electron Microscopy
TEM	Transmission Electron Microscopy
USF	Ultrasonic fragmentation

List of Symbols

d	Particle diameter
d_{Si}	Density of silicon
E_p	Young's modulus of pSi
E_{Si}	Young's modulus of Si
h_c	Critical thickness of the layer
I_0	Initial light intensity
m	Mass of the material
n	Refractive index of the particle
P	Porosity of the material
Pr	Pressure
Δp	Pressure difference
P_0	Saturation pressure
r	Radius of the spherical meniscus
R	Gas constant
S	Wafer area
T	Temperature
V	Volume of the liquid
x	The particle's size parameter
γ_{LV}	Surface tension of the fluid
γ_{Si}	Average values for crystallographic orientations
ε	Dielectric constant
Θ	Scattering angle

Table of Contents

Acknowledgements 5

Abstract 8

List of Figures 9

List of Tables 13

List of Abbreviations 16

List of Symbols 17

Author's Publications 22

Chapter 1. Introduction and Background 23

1.1. Porous silicon formation routes 24

1.1.1. Porous silicon formation by anodisation 27

1.1.2. Classification of Etching 32

1.1.2.1. Chemical etching 32

1.1.2.2. Electrochemical etching 33

1.1.3. Porous silicon classification 34

1.1.3.1. Microporous silicon 34

1.1.3.2. Mesoporous silicon 35

1.1.3.3. Macroporous silicon 35

1.1.4. Porous silicon membranes 36

1.1.5. Tuning the properties of porous silicon 38

1.1.6. Colour of porous silicon 39

1.1.8. Pore Volume (Porosity) in Porous Silicon 40

1.1.7. Surface area of Porous Silicon 41

1.2.1. Characterisation challenges with porous silicon 42

1.2.1.1. Microscopy of porous silicon 42

1.2.2. Gas adsorption analysis of pSi 44

Processing of porous silicon 46

1.3.1. Processing procedure with pSi 46

1.3.2. Drying techniques applied to pSi 47

1.3.3. Oxidation of pSi 50

1.3.4. Melt intrusion in pSi 51

1.4. Applications of porous silicon 52

1.4.1. Applications survey based on relevant pSi properties 53
1.4.2. Drug delivery with Porous Silicon 55
1.4.2. Gas sensing with Porous Silicon 64
1.5. References 66
Chapter 2 Fabrication and processing of porous silicon 71
2.1. Porous silicon formation by anodisation 72
2.2. Formation of pSi particles (Ball milling and Ultrasonication) 81
2.3. Effects of drying and humidity variations during storage 91
2.4. Particle size selection 94
2.4.1. Size select sedimentation 94
2.5. Conclusions 104
2.6. References 105
Chapter 3. Supercritical fluids and supercritical drying 110
3.1. Introduction 110
3.2. Supercritical fluids and their properties 111
3.3. Applications of supercritical fluids 113
3.4. Air Drying of porous silicon 116
3.5. Supercritical drying: process 119
3.6. Impregnation using supercritical fluids 122
3.7. Critical thickness study 123
3.8. Conclusions 125
3.9. References 126
Chapter 4. Characterization of porous silicon (pSi) with results and discussion 128
4.1. Gas adsorption analysis 128
4.2. Electron microscopy 136
4.3. Porosity determination by JMicrovision software 149
4.4. Particle size measurements 157
4.4. Conclusions 169
4.5. References 170
Chapter 5 Conclusions and Future work 171
5.1. Conclusions 171
5.2. Future work (Outlook) 175
Chapter 6. Appendices 176

To my loved ones

Author's Publications

Published:

1. ***A gentle sedimentation process for size-selecting porous silicon microparticles to be used for drug delivery via fine gauge needle administration, Journal of Silicon,* pp. 1-8 (2020)**
   Elida Nekovic *, Catherine J. Storey, Andre Kaplan, Wolfgang Theis and Leigh T. Canham

2. **Preserving surface area and porosity during fabrication of silicon aerocrystal particles from anodized wafers*, Journal of Porous Materials*, pp. 1-6. (2020)**
   C.J.Storey*, **E.Nekovic**, A.Kaplan, W.Theis, L.T.Canham

3. **Supercritically-dried membranes and powders of >90% porosity silicon with pore volumes exceeding 4cm^3/g, *ECS Journal of Solid State Science and Technology*, *9*(2), p. 024016 (2020)**
   Elida Nekovic, Catherine J.Storey, Andre Kaplan, Wofgang Theis and Leigh T.Canham

4. **Tuning porosity and surface area in air dried and supercritically dried porous silicon membranes**
   (CONFERENCE UK SEMICONDUCTORS 2019)
   Elida Nekovic, Catherine J. Storey, Andre Kaplan, Leigh T. Canham and Wolfgang Theis

5. **Processing techniques for supercritically dried porous silicon**
   (CONFERENCE POROUS SEMICONDUCTORS SCIENCE AND TECHNOLOGY 2018)
   Catherine J. Storey, **Elida Nekovic**, Andre Kaplan, and Leigh T. Canham

6. **Atmospheric plasma-enhanced spatial-ALD of InZnO for high mobility thin-film transistors, *Journal of Vacuum Science & Technology A: Vacuum, Surfaces, and Films*, *36*(4), p. 04F401 (2018)**
   Andrea Illiberi, Ilias Katsouras, Sasa Gazibegovic, Brian Cobb, **Elida Nekovic**, Willem van Boekel, Corne Frijters, Joris Maas, Fred Roozeboom, Yves Creyghton, Paul Poodt, and Gerwin Gelinck

In preparation:

7. **An effect of the oxidation and recombination times on the porous silicon membranes varying the porosity (2020)**
   Rihan Wu, **Elida Nekovic**, Catherine J. Storey, Andre Kaplan and Leigh T. Canham

Chapter 1. Introduction and Background

In this chapter, background information on the various topics covered in this thesis is provided, namely: the fabrication routes and types of porous silicon films, their uses, their processing, tunable properties and specific characterization techniques used (see chapter 4). The detail is provided on the equipment and safety measures needed to porosify silicon wafers via electrochemical etching in HF-based electrolytes and additional tuning of porosity by chemical etching (see chapter 2). Further detail is also given on the importance of the drying step (see chapter 3) after wet etching techniques.

Introduction

In the mid-1950s, porous silicon was accidentally discovered by Uhlir at Bell Laboratories (Uhlir 1956). Whilst trying to develop an electrochemical machine for use in microelectronics circuits, he found that under certain currents and solution compositions, silicon did not dissolve uniformity. Instead, holes were formed in the (100) direction of the wafer. This was reported in a Bell labs technical note (Uhlir 1956) but the material did not gain any interest.

In the 1970s and 1980s, interest in porous silicon arose because the high surface area of porous silicon was very useful as a model of the crystalline Si surface in microscopic studies (Gupta 1988; Gupta 1991; Dillon 1990; Dillon 1992).

In the late 1990s, the quantum confinement effects of room-temperature photoluminescence were discovered by two research groups: Leigh Canham at the Defense Research Agency in England (Canham et al. 1990) and Ulrich Goesele and Voelker Lehmann at Duke University in the United States (Lehmann et al. 1991). Both groups showed that if made thin enough, the porous silicon material can display quantum confinement effects. Canham managed to thin the pore walls of the electrochemically etched material to a thickness of less than 5 nm, whereby the material displayed a bright orange-red colour when illuminated with ultraviolet light (Canham 1990).

Furthermore, porous silicon (pSi) is a nanostructured material fabricated via electrochemical etching of crystalline silicon. The tunable properties that porous silicon displays are: a large surface and free volume, controllable pore size from a few nanometers to a few hundreds of nanometers and microns, depending on the conditions of preparation.

Moreover, the surface of porous silicon can be modified with a variety of molecules, such as: organic, inorganic and biological. In the body, porous silicon dissolves into silicic acid, which is present in human tissue (Canham 2014). Porous silicon can offer very attractive chemical and morphological properties for a variety of applications.

Background

Fabrication of porous silicon

1.1. Porous silicon formation routes

Porous silicon can be formed using numerous fabrication techniques, which can be broadly divided into two main groups: *"top-down"* and *"bottom-up"* (Canham 2014). This section aims to provide an overview of available formation routes and to relate them to their possible applications (later in this Chapter). Figure 1a represents a traditional "top-down" route, where porous silicon is fabricated from solid silicon, which is in turn derived from solid silica. Using this route highly porous structures can be etched based on acidic fluoride chemistry (Canham 2014) for example via electrochemical etching. Various "top-down" and "bottom-up" routes from silicon atoms and molecules have been illustrated in Figure 1 (a) and 1 (b).

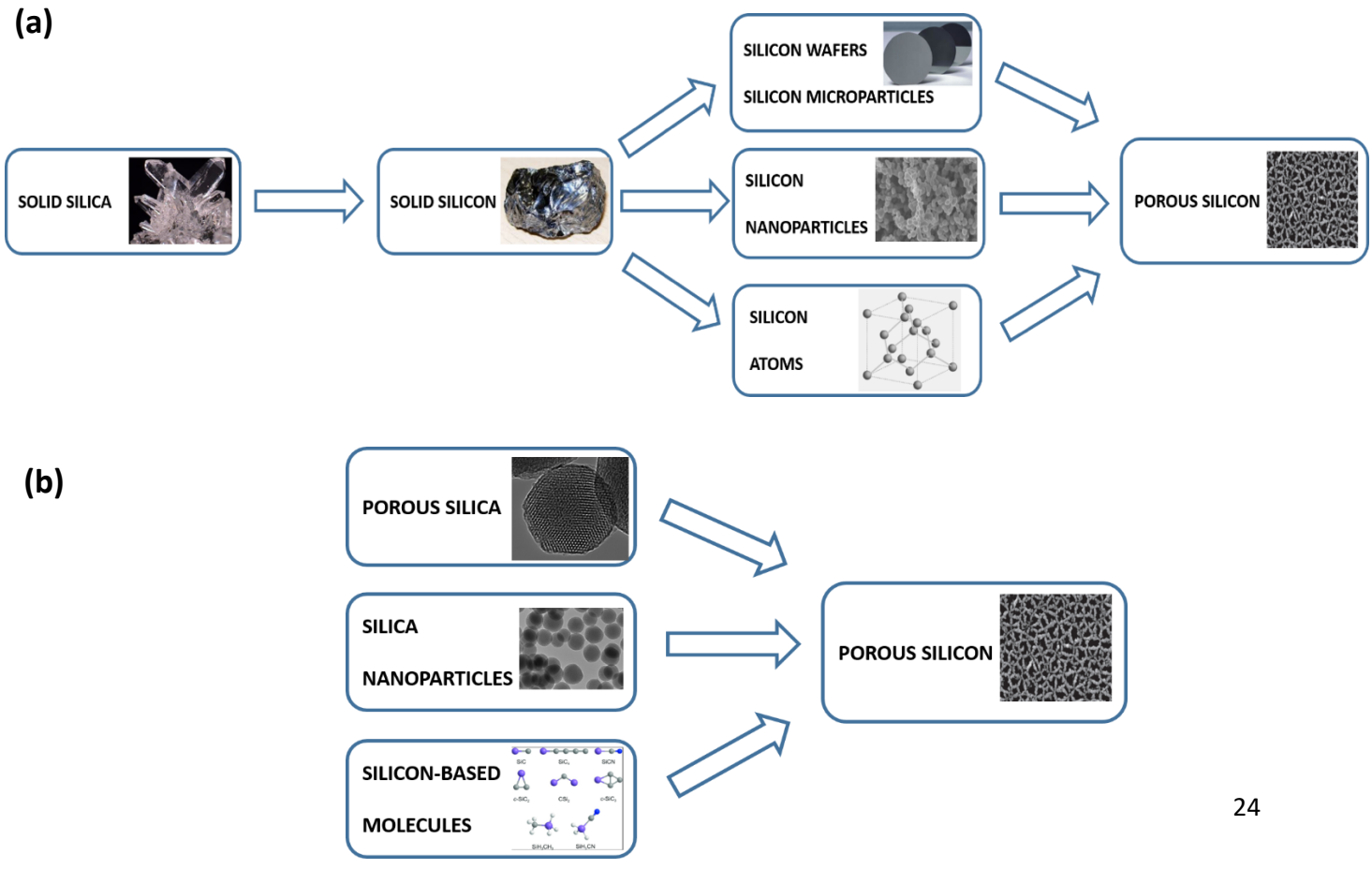

Figure 1 (a) Routes to porous silicon via solid silicon: top-down. (b) Routes to porous silicon via chemical conversion: bottom-up. Adapted from (Canham 2014).

When porous silicon is fabricated, it is interesting to observe the pore morphology. A “pore” is defined as an etch pit of a defined depth *d* and width *w*. For most pSi layers, pores are often interlinked and closed at one end. A cylindrical pore shape with a degree of “branching” is the most frequent in the literature, Figure 2 (c). Figure 2 illustrates the different geometries and morphologies of pSi layers (mainly macroporous). The following factors are considered when describing pore morphology: layer thickness and porosity, the distance between pores and branching parameters, such as branch orientation.

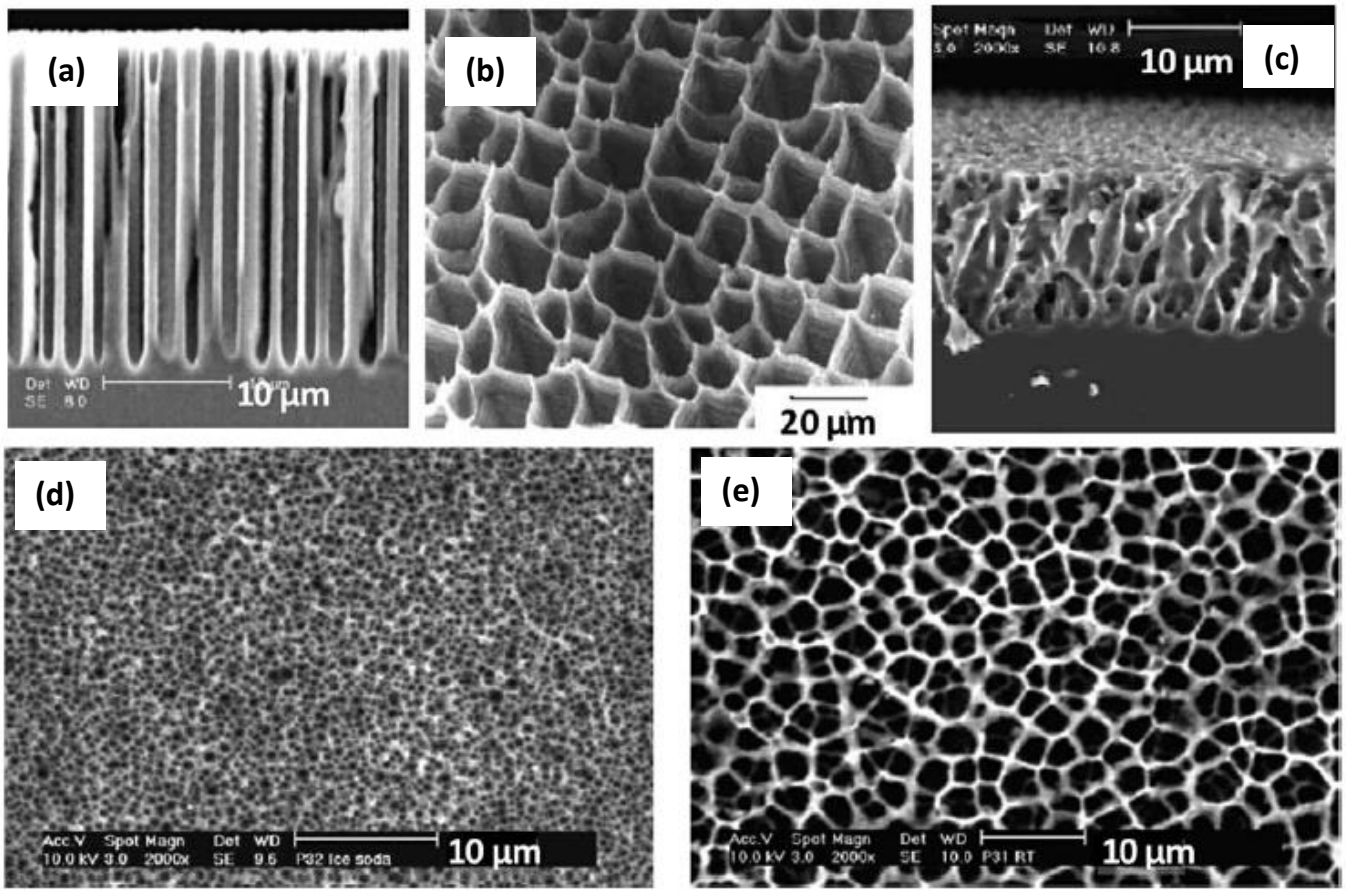

Figure 2 Figure Possible morphologies of different pSi layers (Korotcenkov 2010).

Porous silicon consists of a silicon skeleton comprised of a network of pores. When using an etching fabrication technique, the silicon is etched away to form a skeletal framework and free carriers are depleted. Ongoing chemical dissolution of a pSi skeleton reduces the thickness of the silicon branches. For higher porosities, thin branches disappear completely leaving the structure mechanically weak.

Table 1 provides an overview of all wet-etching fabrication techniques used to create porous silicon. They are classified based on the porosity type: microporous, mesoporous and macroporous. From the table below, we can see that anodisation has been used to generate microporous and mesoporous structures, as well as macroporous materials (considered separately in section 1.1.3. Porous silicon classification).

Fabrication technique	*Class of porosity*	*An early paper on this technique*	*Year*
*** Anodisation**	**Mesoporous**	**Uhlir**	**1956**
Stain etching	Mesoporous	Archer	1960
Anodisation	Macroporous	Theunissen et al.	1972
Anodisation	Microporous	Canham and Groszek	1992
Photoetching	Mesoporous	Noguchi and Suemune	1993
Hydrothermal etching	Mesoporous	Chen et al.	1996
Metal ion-assisted chemical etching (MACE)	Mesoporous	Dimova-Malinovska et al.	1997
Galvanic etching	Mesoporous	Ashruff et al.	1999
Vapour etching	Mesoporous	Saadoun et al.	2002
Dealloying	Mesoporous	Fukatani et al.	2005
Anodisation (alkali)	Macroporous	Abburi et al.	2010
Ultrasonic etching	Mesoporous	Skorb et al.	2012
Micromachining and wet etching	Macroporous	Deng et al.	2013
Platinum NP-assisted etching (PaCe)	Mesoporous	Li et al.	2013
Ion track template etch	Mesoporous	Kaniukov et al.	2016

Table 1 Wet etching routes of pSi formation. Adapted from (Canham 2014). Bold text in Table 1, marked with an asterisk denotes the main fabrication technique used in this doctoral thesis, which proceeds on the next section. References from this table can be found in the Handbook of porous silicon, ed. by Leigh Canham (2014).

Specifically, as listed chronologically in Table 1, together with relevant early papers on each technique, around 15 different wet-etching pSi fabrication techniques have been reported to date. The classification was based on wet etching as the most relevant class of technique to this thesis.

For the last five decades, electrochemical etching has been the most established fabrication approach due to highly directional mesoporosity and macroporosity as well as high tunability of pore sizes. N.B. Porosity classification will be covered in section 1.1.3. Porous silicon classification.

1.1.1. Porous silicon formation by anodisation

The formation route predominantly used in this doctoral thesis is anodisation. Via anodisation, a network of pores is formed in the silicon as a consequence of the electrochemical dissolution of silicon in hydrofluoric acid (HF). This process is achieved by applying a constant current to the silicon in an anodisation cell in the presence of a hydrofluoric acid electrolyte.

The anodisation procedure takes place in an anodisation cell, which consists of electrodes; cathode and anode, a substrate and an electrolyte. There are different types of anodisation cells. The simplest one is a *lateral anodisation cell*, where the silicon wafer acts as the anode and the cathode is made of platinum (or other conductive and HF resistant material) Figure 3(a). This type of anodisation station is very simple but the non-uniformity in porosity and thickness experienced due to a lateral potential drop is a drawback.

The second type of anodisation cell is a *single-cell,* Figure 3(b). Low resistivity wafers are used with no need for metallisation at the back of the wafer. This cell promises good porosity and thickness uniformity.

The third cell type is a *double-tank cell*, Figure 3(c), which was used in this doctoral research. This cell uses an electrolytic backside contact. It consists of two half-cells where Pt electrodes are immersed into the electrolyte and a silicon wafer separates the two half cells. The second cathode is the backside of Si wafer. Compressed air pumps continuously circulate the

electrolyte and remove any hydrogen gas bubbles generated during etching from settling on the wafer and preventing localised etching. Good uniformity is obtained due to the same size of the platinum electrode and silicon wafer, which supports an even distribution of the current. Figure 3 displays all mentioned types of anodisation cell.

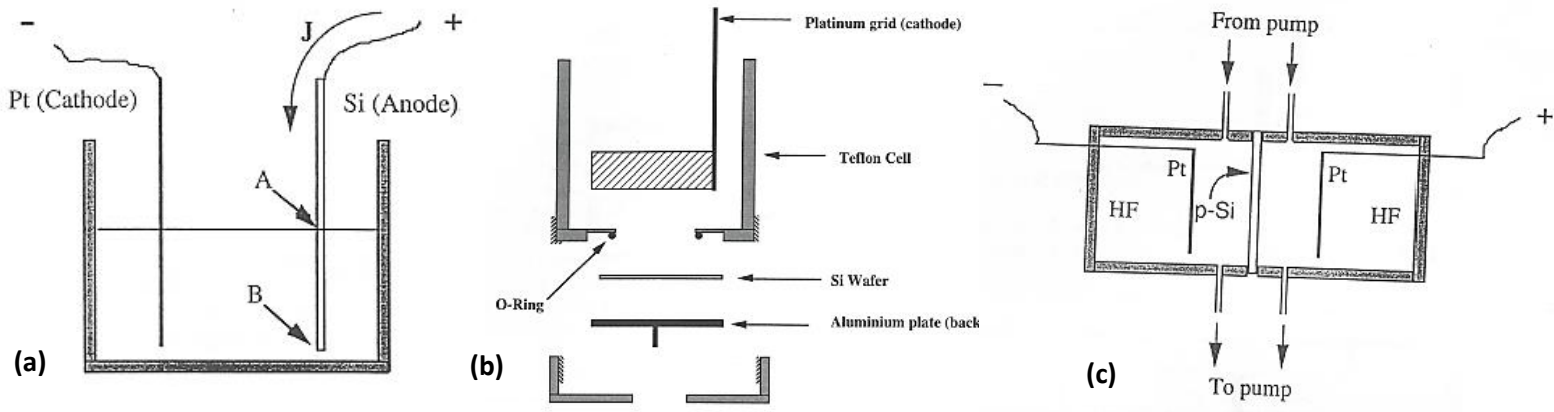

Figure 3 Types of anodisation cells: (a) lateral anodisation cell, (b) single-tank cell and (c) double-tank cell. Adapted from (Canham 1997).

Solution composition

If a purely aqueous HF solution is used, hydrogen bubbles stick to the surface and cause inhomogeneity in the etched surface. The solution is to add a surfactant to the electrolyte which prevents the bubbles from sticking. In this project, ethanol was used as a surfactant to improve the uniformity of the pSi membranes.

Determination of porosity and thickness

Porous silicon membranes can be obtained from a variety of types of silicon, such as: amorphous, microcrystalline and polycrystalline. Using different types of silicon, different electrochemical behaviours during anodisation are observed. Related to the electrochemical etching, the most important parameters that characterize porous silicon are *porosity* and *thickness*. First, we need to record the weight of a bulk silicon wafer (m_1) before anodisation, the weight after anodisation (m_2) and the weight of porous silicon membranes after the dissolution of a completely porous layer in NaOH (m_3).

The formula for calculating porosity (gravimetric method) is as follows:

$$P(\%) = \frac{(m_1 - m_2)}{(m_1 - m_3)} \quad (1)$$

Membrane thickness is calculated using the formula below:

$$W = \frac{(m_1 - m_3)}{S\ x\ d} \quad (2)$$

where *d* is the density of bulk silicon and *S* is the wafer area that is exposed to HF electrolyte during the anodisation process.

Another method of thickness determination is using SEM micrograph cross-sectional imaging which will be shown in the Results chapter. Porosity can also be determined using the software 'JMicrovision 1.27' (https://jmicrovision.github.io/contact.htm) regardless of the thickness of the layers. This method is suited to layers of uniform thickness with unbranched pores and assumes that the ratio between open areas of pores and the scanned area represents the ratio between the total volume of voids to the entire layer volume (Elia et al. 2016).

Electrode Materials

The most commonly used material for the cathode is platinum as it is highly chemically resistive. As a consequence, minimal platinum deposits build up in the electrolyte over time due to its very small corrosion rate. Other materials that have been used for electrodes are doped diamond, doped silicon, silicon coated with doped diamonds and vitrified carbon.

Safety

Hydrofluoric acid (HF) penetrates the skin and dissociates into fluoride ions that can destroy deep tissue layers together with bone. Pain experienced due to skin exposure might not happen for 1-24 hours. If HF is not rapidly neutralized and fluoride ions bind, tissue destruction can continue for days resulting in limb loss or death. HF vapours are also an inhalation hazard. Furthermore, it is also very necessary that the electrolyte reservoirs (Figure 3 a) are vented as the volume of hydrogen gas produced during anodisation can be significant (Motohashi et al. 1995).

Careful handling of stored anodised membranes must be considered, especially when in large quantities. Appropriate personal protective equipment (PPE) is required when working with HF acid to protect our skin, eyes and lungs and it is demonstrated in Figure 4. Required PPE (Figure 4b) includes goggles, face shield (plastic), acid resistant apron, long trousers and sleeves, closed-toe shoes and gloves. Thin disposable gloves (blue nitrile gloves) are used to provide a contact barrier only and should be worn together with a thicker PVC or neoprene gloves which provides better resistance. An HF monitor can also be worn.

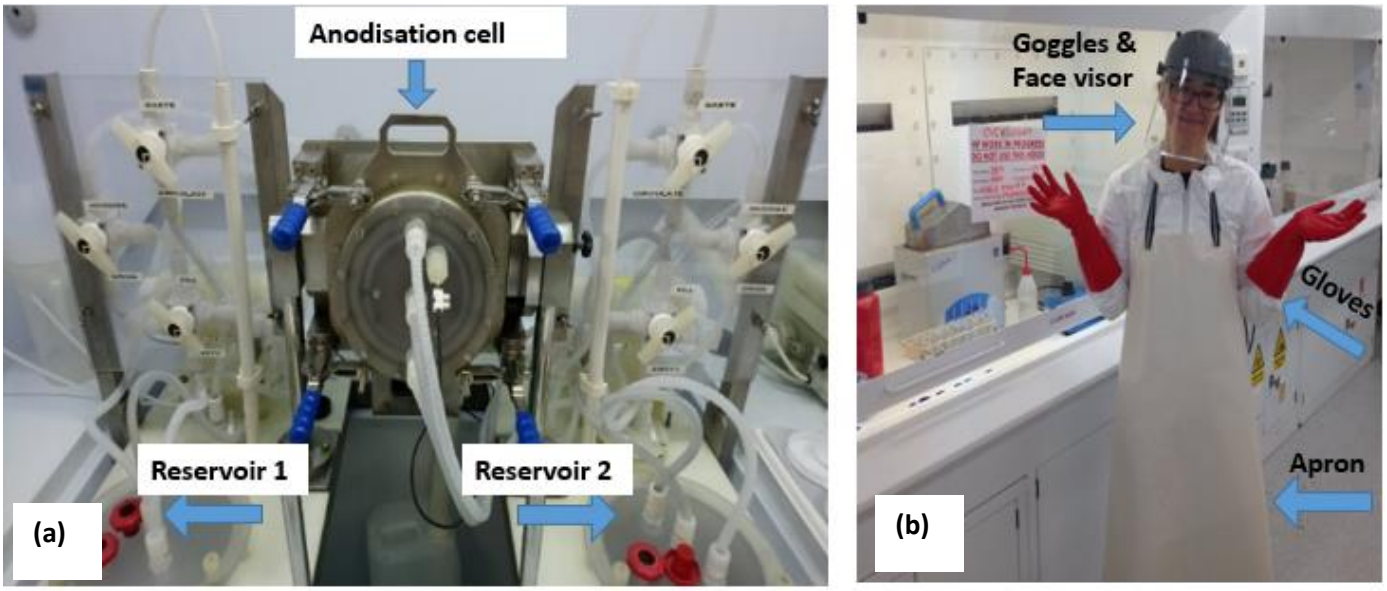

Figure 4 (a) Double-tank anodisation cell. (b) Personal protective equipment PP (lab coat, safety glasses, face visor, apron, gloves, HF monitor) for work with HF.

In the event of skin or eye exposure to HF:

- Call emergency.
- Remove all exposed clothing and immediately wash all exposed areas of the body with water from the safety shower/eyewash.
- After flushing the skin with water for 15 minutes, apply calcium gluconate directly to an exposed area.

In the event of spills:

- Absorb the spill with the sodium carbonate first and then wash the area with water. Small spills of up to 100 ml need to be covered with dry sodium carbonate and absorbed

using spill pads. For minor spillages outside the fume cupboard: wear appropriate PPE, minimum face shield, apron, gloves and toxic dust respirator (toxic sodium fluoride will be produced). Scatter an excess (10:1) of solid sodium carbonate (soda ash) over the spilt HF and leave to stand for a few minutes. Scoop up residue and transfer to a lidded container for disposal as hazardous waste. Wash spillage site with copious amounts of water. (Reference: '*Enhanced Good Chemical Practice for Work with Hydrogen Fluoride and Hydrofluoric Acid*' document UHSP/15/HS/05 Schedule 3.5/06)

- If the spill happens in a confined area or area without ventilation, evacuate the room immediately. In the event of a major spillage outside of the fume cupboard leave the laboratory immediately and do not re-enter. Inform the emergency services.

In the event of ingestion:

- If swallowed, do not induce vomiting.
- Take large quantities of water and get medical attention as soon as possible.

1.1.2. Classification of Etching

Table 1 outlined various etching fabrication techniques, including chemical and electrochemical etching, developed in this thesis which will be described in this section.

1.1.2.1. Chemical etching

In contrast to electrochemical anodisation, chemical etching does not involve the exchange of free charge but only the redistribution of electron density among surface bonds. Wet chemical etching is an inexpensive and straightforward technique.

Acid etching will first dissolve the protective oxide layer to expose and enable the etching of the silicon substrate and is anisotropic. This type of etching is very selective as to what materials can be etched. Semiconducting materials work best in this case. The (111) plane of the crystalline silicon has the lowest etch rate and acts as an etch stop for the dissolution procedure (Tsuboi 1999). Contrary to this, a material with a crystallographic orientation of (100) has the highest etch rate.

Heterogeneities can also exist in a material and this can result in non-uniform etching profiles and etch rate changes. The etch rate is defined as the depth etched per unit of time. It is very difficult to control very high etch rates, however high etch rates are desirable for deep pore formation or substrate removal. The etch rate is controlled by the etchant concentration, which in turn also influences the temperature of the etchant and the production rate (ratio of the number of the material produced and the time spent producing them).

1.1.2.2. Electrochemical etching

In the 1950s, whilst electrochemical polishing of silicon in aqueous HF, Uhlir discovered that porous silicon had been formed. Since then, anodic etching has become the most successful technique for porous silicon fabrication in semiconductors. In comparison to chemical etching, the exchange of free charge occurs during electrochemical etching.

Dissolution of pSi can occur homogeneously during electropolishing (at high current densities and high potential) and the double-tank cell used in this thesis (figure 4) is the most preferable type to use because it provides a good (uniform and low contact resistance) Si backside contact (Canham 1997).

A double-tank cell consists of two platinum electrodes; one electrode in each cell (front and back). There is no need for backside metallization and it avoids potential metal contamination of the porous silicon. The drawback is that the pSi is electrically floating and therefore the potential at the surface is not well defined. The porosity is affected by the local current density.

During electrochemical etching, hydrogen bubbles are generated, which can stick to the silicon surface and cause pore degeneration.

Pore geometry in Si is varied and a large variety of morphologies are obtained. Oxidation occurs at the same time as dissolution.

There are different methods explaining pore growth beginnings, for example at structural defects or in mechanically strained areas (Canham 2014). It is quite important to supply the holes locally by local above-bandgap photoexcitation. This is possible to achieve in n-doped material, as the holes are the minority carriers.

In conclusion, one of the biggest challenges in the production of porous silicon is creating lateral homogeneity of the pSi layer, as already mentioned in the previous section.

1.1.3. Porous silicon classification

The main aim of this section is to classify porous silicon-based on pore size range and possible applications. There are three size classifications: microporous silicon (pore size < 2 nm), mesoporous silicon (2-50 nm) and macroporous silicon (> 50 nm) (Canham 2014).

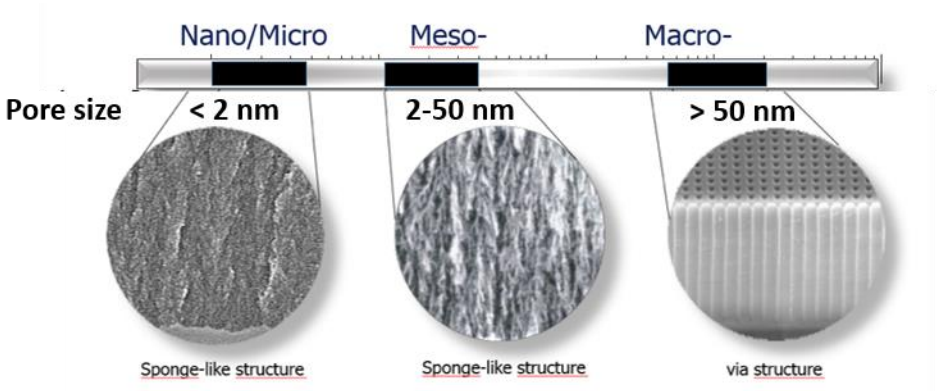

Figure 5 SEM images of microporous, mesoporous and macroporous structures, respectively.

Figure 5 presents SEM images of each of these classifications. The main interest of this PhD project is mesoporous silicon, due to its highly tunable properties and wide applications.

1.1.3.1. Microporous silicon

This type of *porous* silicon has not received as much attention as mesoporous silicon or macroporous silicon. However, microporous silicon has an advantage in applications such as explosives, gas sensing and hydrogen storage. These nanostructures have the highest surface areas and the highest pore densities and as a consequence, they are extremely reactive and sensitive to the ambient.

Porous silicon structures of very high surface areas (540-840 m^2/g) are achieved by wafer anodisation, metal-assisted etching, galvanic etching and silica reduction. The smallest generated pores via electrochemical etching are in the range of 1-2 nm (Canham and Groszek 1992).

1.1.3.2. Mesoporous silicon

One of the most important properties of mesoporous silicon is the geometry of the pore network and also it's surface chemistry.

Different types of silicon wafers can be used for the fabrication of pSi such as; highly doped p-type or n-type wafers of different resistivity. During anodisation, increasing the current density will increase porosity, whilst using low HF concentrations will slow etch rates but increase porosity. Variations in electrolyte compositions lead to different pore structures. If the fabrication of thicker pSi samples is desirable, the stop-etch method can be used (Billat et al. 1997). Etch-stop is defined as a technique that allows termination of the etching process at a controllable depth (Billat et al. 1997). The disadvantage of the stop-etch method is very long fabrication times. In this doctoral thesis, the stop-etch method was not used.

A very important part of the process when fabricating mesoporous silicon is the potential for tuning porosity and pore size. This will be further explained in the Results chapter, within the fabrication of pSi. To perform structural characterisation of mesoporous silicon there are two most used approaches: gas adsorption and electron microscopy. Using gas adsorption, pore size distributions can be obtained. The range of the pore sizes obtained via electrochemical etching is typically 3-20 nm.

1.1.3.3. Macroporous silicon

The term macroporous is related to cylindrical pores with pore sizes in the order of microns. Macroporous silicon is used in several applications, such as X-ray imaging, chemical reactor, capacitors, as an antireflection layer in solar cells, metallic barcodes, in lithium-ion batteries, microelectronics (Canham 2014).

To fabricate macropore arrays, the pre-structuring of Si substrate via lithography, as well as the alkaline etching, are required (Canham 2014).

1.1.4. Porous silicon membranes

The main aim of this section is to present the most popular pSi membrane fabrication methods and to highlight some issues with characterizing them. Potential applications are also discussed. Fabricated membranes are free-standing membranes, membranes suspended above silicon chips and membranes transferred to and supported on a substrate of a different material (Canham 2014).

Three top-down techniques for fabrication of porous silicon membranes from solid silicon are electrochemical etching (anodisation), (see section 1.1.1.2 for more detail) micromachining and thin film deposition/annealing.

Electrochemical etching: different routes of realization are (Canham 2014):

1. Anodisation through entire silicon wafers of specific thickness.
2. Anodisation through solid thin silicon membranes.
3. Anodisation of part of the thickness of a wafer and afterwards "lift-off" via raising the current density. The lift-off method (electropolishing) is observed at high potential and current densities, releasing the layer from the substrate as the interface between the layer and the wafer dissolves completely.
4. Pre-thinning of selected areas of the wafer with subsequent anodisation (Canham 2014). There is likely to be a porosity gradient across the thickness of the membrane due to the long etching times.

Micromachining

Micromachining involves creating porosities with highly defined mesopore diameters at lower concentrations. Very good mechanical stability is achieved. These structures are supposed to have similar properties to the bulk silicon and they are not as biodegradable as the electrochemically etched porous silicon (Canham 2014).

Deposition/Annealing

Creating silicon films of thickness in the range of 10-50 nm is available using this technique. High values of porosities are achieved using silicon nitride in comparison to using oxide as the barriers layers.

Applications of pSi membranes

Some of the possible applications using membranes are listed in table 2 below.

Application	*Type of porosity*	*Fabrication technique*	*Thickness (microns)*	*Reference*
Gas sensors	Mesoporous	Anodisation	70	Taliercio et al. 1995
Humidity sensors	Mesoporous	Anodisation	1	O'Halloran et al. 1998
Medical implants	Mesoporous	Micromachining	5	Desai et al. 2000
UV optical filter	Macroporous	Anodisation	50	Avutsky et al. 2003
Waveguide sensors	Macroporous	Anodisation	1	Rong et al. 2008
Optical sensors	Mesoporous	Anodisation	30, 64	Alvarez et al. 2011
*** Drug delivery**	**Macroporous**	**Anodisation**	**50**	**Chau and Melvin 2012**

Table 2 Applications and the corresponding fabrication techniques of the membranes. References from this table can be found in the Handbook of porous silicon, ed. by Leigh Canham, (2014).

Bold text in Table 2, marked with an asterisk denotes the foremost application of pSi membranes fabricated in this PhD project.

1.1.5. Tuning the properties of porous silicon

Porous silicon properties are highly tunable via the surface chemistry, through manipulation of structural parameters or via impregnation with other materials. Such tunable properties include: optical refractive index, optical reflectivity, surface wettability, thermal conductivity, mechanical stiffness and optical bandgap; and each property can be finely tuned according to the chosen application. Some properties require the optimisation of more than one parameter. For example, the surface wettability of some materials with high surface areas can be dramatically affected by manipulating both the surface chemistry and specific structural morphologies. Alternatively, optimisation of porosity is an important factor which can be fine-tuned to aid medical biodegradability (Canham 1997). Furthermore, three approaches to tuning the properties of porous silicon properties mentioned above are:

- Pore impregnation (polymer, metal etc.)
- Structural parameters (such as porosity, skeleton size or surface area) and
- Surface chemistry (Si-O, Si-C and Si-N bonding).

In terms of mesoporous silicon, the tunable range for each property is listed below (Canham 2014).

Structural properties: porosity - 20-95 %; density - 0.12 to 1.9 gcm^{-3}; pore diameter - 2-50 nm; surface area - 100-800 m^2g^{-1}; and lattice constant - 0.54 to 0.59 nm.

Mechanical properties: Young's modulus - 1-100 GPa, Hardness - 0.2 - 10 GPa (layers); fracture toughness – 1-4 MPa.

Optical properties: bandgap - 1.1-3.2 eV; infrared refractive index - 1.1-3.0; colour from brown to yellow and reflectivity - 0.1 to 10%.

Electrical properties: resistivity - 10^3-10^{12} Ωcm; electron mobility - 0.1-30 cm^2/Vs. hole mobility - 2-6 cm^2/Vs and dielectric constant – 2-8.

Thermal properties: conductivity - 0.03-20 $Wm^{-1}K^{-1}$; melting point – 800-1414 ˚C.

The values listed above are extracted from reference (Canham 2014).

1.1.6. Colour of porous silicon

This section aims to explain how the colour of porous silicon can be tuned. Specific colours can relate to certain applications, which are mentioned.

Porous silicon can exhibit a variety of colours depending on the physical form and the contents of the pore. Solid silicon is grey, but by tuning the properties of the material, the colour can also be tuned. It is also interesting that the colour of pSi powders can be chemically changed in the way that some food nutrients which have vivid colours provide pigments to food.

In 1956, Uhlir reported that the colour of the surface of his pSi material ranged in colour from "matte black" to "brown/red deposit". Uhlir recognized that optical interference effects are induced with the lower refractive index values of pSi.

The addition of a solvent can change the colour of the material. For example, the addition of a drop of ethanol followed by its evaporation on the pSi surface, will change the colour immediately and return. In Figure 6, the varied physical colours of ultrathin porous silicon layers (made by stain etching) are presented.

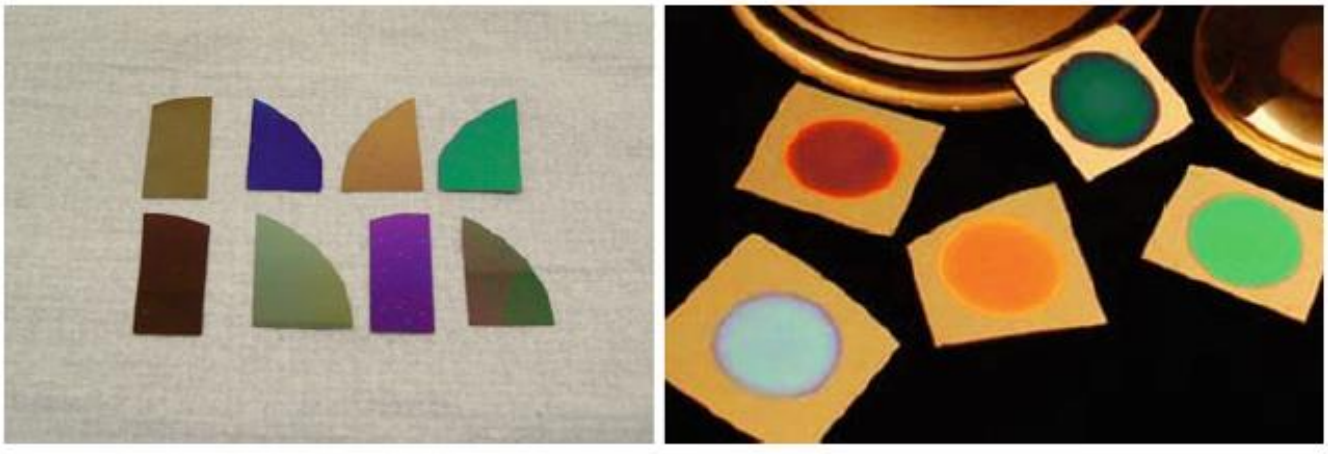

Figure 6 Varied "physical colours" from ultrathin single layers of stain-etched mesoporous silicon (LHS-A. Loni unpublished 2009) and anodised mesoporous silicon photonic crystals (RHS-Gooding Group, Univ. New South Wales, Australia http://www.rsc.org/Publishing/ChemTech/Volume/ 2009/02/biosensors.asp)

Furthermore, some multilayers of mesoporous silicon (with modulated porosity) can look like "glitter" or "gold-leaf" due to its porosity, once it is detached from the Si wafer. These can be used in cosmetics. Porosity change affects the refractive index.

One colour silicon samples have shown some potential in various applications. The example of a suppressed optical reflectivity is "black" silicon. The first black silicon was made between the 1950s and 1960s. It is an unwanted by-product of reactive ion etching (Canham 2014).

In several applications, the colour of porous silicon is important to be accepted by the customer.

1.1.8. Pore Volume (Porosity) in Porous Silicon

Reported values of pore volume (porosity) up-to-date are presented in Table 3.

Pore volume (ml/g)	*Porosity from pore volume (%)*	*Form of pSi structure*	*Reference*	*Year*
0.02	5.0	Macroporous wafer	N/A	N/A
0.23	35.0	Membrane	Tang et al.	2010
0.29	40.0	Photonic crystal	Muller et al.	2000
0.65	60.0	Mesoporous microparticles	Chiappini et al.	2010
1.00	70.0	Mesoporous nanowire	Qu et al.	2010
1.70	80.0	Silicon nanotubes	Wu et al.	2012
5.13	**92.3**	**Mesoporous aerocrystal thick membranes**	*** Nekovic et al.**	**2020**
8.10	95.0	Mesoporous aerocrystal thin films	Canham et al.	1994

Table 3 Reported pore volume (porosity) of pSi values up-to-date. References from this table can be found in the Handbook of porous silicon, ed. by Leigh Canham (2014).

1.1.7. Surface area of Porous Silicon

Surface area values achieved to-date as a function of porosity class are listed in Table 4.

Surface area (m^2/g)	*Form of pSi*	*Reference*	*Year*
86	Meso- Film	Hai et al.	2009
280	Powder	Loni and Canham	2013
356	Meso- Powder	Batchelor	2012
500	Meso-/Micro- Film	Bao et al.	2007
549	**Membrane**	*** Nekovic et al.**	**2020**
700	Film	Becker et al.	2010
864	Powder	Loni et al.	2015
890-910	Layer	Becker et al.	2011
1125	Powder	Loni et al.	2015

Table 4 The reported surface area of pSi values up-to-date. References from this table can be found in the Handbook of porous silicon, ed. by Leigh Canham (2014).

1.2.1. Characterisation challenges with porous silicon

The properties of mesoporous silicon depend on its surface area and the distribution and size of the pores. Hence, the characterisation of porous silicon is key to optimising fabrication processes and linking them to specific properties. This section focuses on the characterisation of pSi, including some of the possible challenges.

1.2.1.1. Microscopy of porous silicon

To determine the structure of porous silicon, a variety of electron microscopy techniques have been performed to date in the literature. Techniques of interest to this thesis are briefly introduced in this section and will be further explained in the experimental methods chapter.

Transmission electron microscopy (TEM)

For achieving detailed morphological analysis at the nanoscale, the combination of TEM and high-resolution TEM (HRTEM) with a high degree of precision can be used (Figure 7). HRTEM will detail the lattice parameter, crystalline size and the orientation of the silicon nanocrystals in the pSi. TEM also enables a cross-sectional analysis of pSi and can analyse the in-depth porosity profile of pSi multilayers.

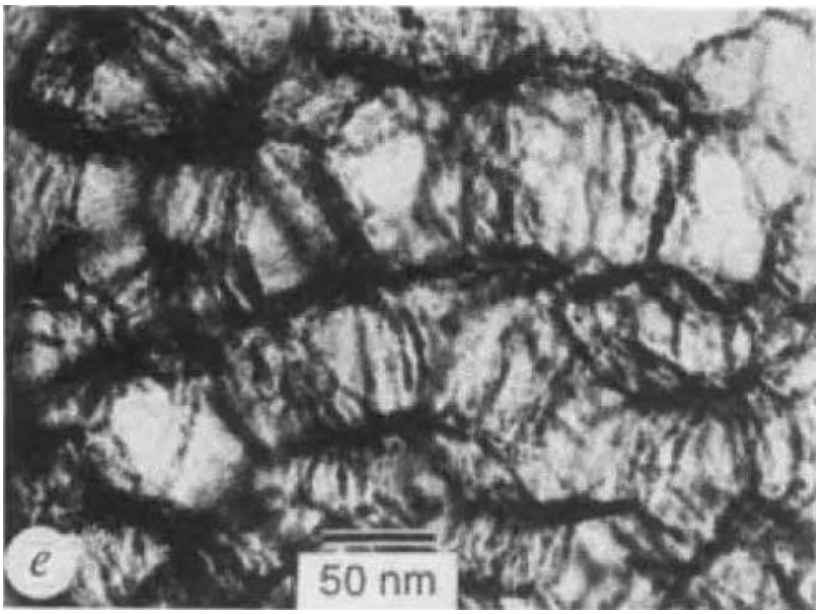

Figure 7 TEM images of ultrahigh porosity Si structures (Canham 1994).

Scanning electron microscopy (SEM)

SEM and high-resolution SEM (HRSEM) are used for studying the morphology of porous silicon e.g. pore size, layer thickness, distribution of pores. Cross-sectional and plan view images can both be obtained. SEM examples will be given in Chapter 4, Characterisation of porous silicon.

Atomic force microscopy (AFM)

AFM is used for measuring surface roughness and is important for biomedical and optical applications. For optics, the low surface roughness of the external surface is needed for achieving good quality optical layers. When fabricating pSi via anodisation, a low surface roughness allows for easier, more convenient detachment of pSi from the Si substrate.

PSi is a very demanding material to characterize. The microscopy techniques above allow determination of the morphology and properties of pSi from micro- to nano-scale.

1.2.2. Gas adsorption analysis of pSi

The key parameters for applications using porous silicon are pore volume (porosity) and surface area. In particular, for medical applications, tuning surface area and pore size are vital.

Pore volume is defined as the open volume (ml) per unit weight (g) of the material. Surface area is described as the exposed internal surface (m^2) per unit weight of the material (Sailor 2010). These two important parameters can both be measured using adsorption-desorption analysis (Gregg and Sing 1982). Pore size and pore shape information can also be obtained using this methodology.

Analysis principles

The gas adsorption-desorption process relates to nitrogen adsorption via capillary condensation from the gas phase and adsorption-desorption after the pore filling. There are different types of equipment used, but the sample preparation procedure is common to all of them.

Sample preparation steps and analysis steps:

- A known amount of the porous material is placed in a glass sample tube;
- Degassing is carried out before gas adsorption analysis;
- Weight of the sample before and after degassing is recorded;
- The sample is then placed into the instrument;
- The sample tube is evacuated;
- The free space is measured by helium dosage because it is very unreactive and used to provide an inert protective atmosphere for the materials to be characterised;
- After the helium is evacuated, the tube is then immersed in cryogenic fluid;
- The adsorbate gas is dosed in incremental volumes with the pressure being measured in situ;
- Capillary condensation: dosing continues until a plateau is reached indicating complete filling of pores ;
- The pressure is then reduced and liquid starts to desorb;
- The porous structure is empty again.

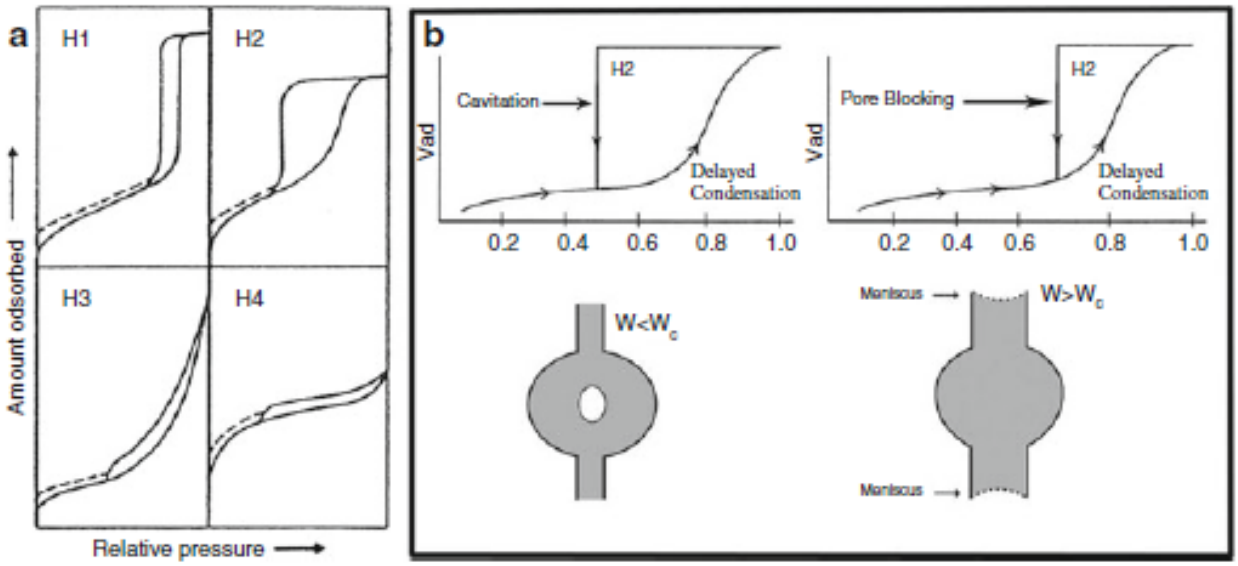

Figure 8 (a) Hysteresis loops from gas adsorption-desorption (IUPAC classification. (b) Schematic view of the pore morphology effect that give rise to H2 hysteresis curve (Thommes, 2010).

Figure 8 (a) is an example of the hysteresis loops from the gas adsorption-desorption. Surface area is obtained from the adsorption branch of the isotherm (area of the relative low vapour pressure) following the complete coverage of the pore walls.

Figure 8 (b) shows an asymmetric type H2 hysteresis loop of mesoporous silicon with an ordered network of parallel, straight mesopores with no lateral interconnection.

Further discussions with suitable results will be considered in the Results chapters.

Processing of porous silicon

1.3.1. Processing procedure with pSi

Silicon wafers that have been electrochemically etched, require a set of different supplementary processing steps preceding their use. This can include drying, comminution, manipulation of surface chemistry, impregnation and coating to optimise membranes, layers, nanoparticles or substrates for their intended application.

Figure 9 shows a process flow for electrochemically etched wafers. Different subsequent processing steps offer different advantages, for example, if the pores are impregnated before drying, the mechanical strength of the delicate pore structure can be improved and the effects of capillary forces during drying are reduced. Using electrochemical etching ultrahigh porous silicon can be processed too. In this project, membranes and particles have been fabricated and processed using relevant processes from Figure 9.

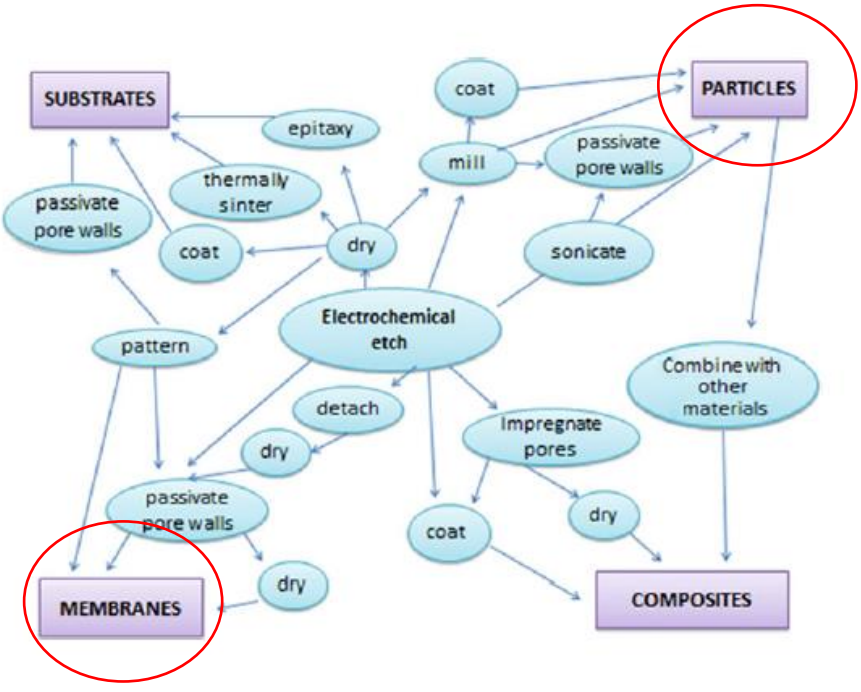

Figure 9 Process flow for electrochemically etched (porosified) silicon wafers with indicated structures fabricated and processed in this project. Adapted from (Canham 2014).

A second example is a very common processing step, chemical passivation of pSi surfaces. This step is performed after particle sizing or some patterning processes. Related to the previously mentioned, some of the applications can derivatise the pore walls during anodisation (Mattei and Valentini 2003). The third example considers a choice of the optimum process route for a target structure and its application area. A fourth example is patterning which can be performed before or after etching. A further processing technique is microwave processing (Bykov et al. 2000). It is used for accelerating the impregnation and chemical reactions.

Another important processing step is supercritical fluid processing of porous silicon. It is based on the removal of residues from small mesopores and micropores in silicon. Usage of such fluids implies faster processing than with conventional solvent rinsing.

Sonication is a route for achieving porous silicon nanoparticles and microparticles (Park et al. 2009, Kale et al. 2012, Thakur et al. 2012) which help maximize yield and is, therefore, an interesting topic for the future. It is also worth mentioning that photolithography is an elegant way to generate porous silicon microparticles of highly defined size and shape. Furthermore, by repeating sedimentation and centrifugation or filtration processing steps, nanoparticle size selection can be improved (Valenta et al. 2011).

A variety of different processing steps are employed to achieve desirable physical forms as well as surface properties of pSi. For example, to maximise surface areas a combination of optimized etching, drying and passivation are required.

1.3.2. Drying techniques applied to pSi

Drying of porous silicon layers of high porosity is a very important step in the fabrication procedure. When water is evaporated from the pores, cracking can often be immediately observed, as it can been seen in Figure 10. Cracking is caused by large capillary stresses upon the nanometric sizes of the pores. Critical thickness studies showed that cracking occurs for layers thicker than a critical thickness (Bellet et al. 1998). Critical thickness depends on the porosity of the layer, as well as the surface tension of the drying liquid, with different solvents

having different surface tensions. Water has the highest surface tension (72 mJ/m^2), while pentane has the lowest (14 mJ/m^2) (Canham 2014).

Capillary tensions appear as the liquid evaporates from the pores. In-situ measurements of these stresses can be performed by using optical techniques, such as measuring the wafer's curvature (Canham 2014).

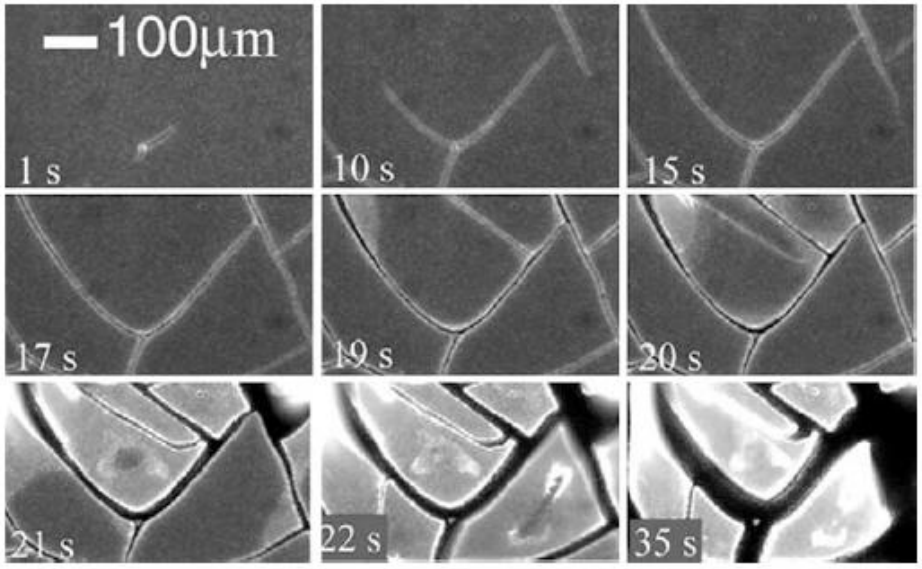

Figure 10 Shrinkage and crack development in a highly porous silicon film during air-drying, as revealed by sequential wide-field photoluminescence imaging (Mason et al. 2002) (Canham 2014).

As-anodised mesoporous silicon is usually dried in the air, but this limits the porosities and surface areas that can be achieved since delicate pore walls can collapse during drying. This is discussed in more detail in Chapter 3-Supercritical fluids and supercritical drying.

The following subsection explains how porous silicon membranes degrade during air-drying and outlines the other types of drying that can be applied to porous silicon. The focus is on pentane and supercritical drying.

Air drying

Mesoporous silicon films on a wafer, after anodisation, can become crazed and also disintegrate during air-drying. Shrinkage, cracking and peeling of the layers increases the higher the porosity. This is because the capillary forces are building up from the pore liquid evaporation.

Drying Techniques Survey

There are different types of drying techniques such as vacuum drying, slow controlled drying, microwave drying, derivatisation with subcritical drying, spray drying etc. These drying types do not avoid capillary forces.

In the table 5, relevant drying techniques are listed, together with the basis for each technique and the advantages, as well as the usage with pSi. Supercritical drying is the most powerful technique and it is used in this doctoral thesis. It will be explained in more detail in Chapter 3-Supercritical fluids and Supercritical drying. This type of drying enables ultrahigh porous luminescent material to be obtained, with a porosity of 95% called aerocrystal. Such highly porous samples are optically flat and have homogeneous surfaces, which allows for optical investigation.

Drying technique	*Basis*	*Advantages*	*Use with pSi*
*** Drying in air**	**Fluid from the pores evaporates in the air.**	**Convenient.**	**Majority of studies.**
Vacuum drying	The wet structure is transferred into the evacuated chamber.	Exposure to air is avoided.	Koizumi et al. 1996.
Freeze-drying	Pore fluid is frozen and further sublimed in the evacuated chamber.	Industrial process.	Amato and Brunetto 1996, Amato et al. 1997
*** Supercritical drying**	**Fluid from the pores is removed after conversion to a supercritical state.**	**Capillary stresses are avoided.**	**Canham et al. 1994. Nekovic et al. 2020**
Derivatization and subcritical drying	Chemical surface modification before air-drying.	The network is mechanically stronger.	Linsmeier et al. 1997.
Pentane drying	Fluid from pores is replaced by liquid pentane which then evaporates in the air.	Capillary stresses are minimized.	Bellet 1998 Oton et al. 2002
Slow controlled drying	The evaporation rate is controlled and therefore lowered.	Capillary stress effects are reproducible.	Pellegrini et al. 1995
Microwave drying	Increased evaporation rate.	Industrial process. Lower drying times.	N/A
Spray drying	Very useful for nanocomposite particle formation or microencapsulation	Industrial process in widespread use	Jung et al. 2013

Table 5 Drying techniques survey. Adapted from (Canham 2014). References from this table can be found in the Handbook of porous silicon, ed. by Leigh Canham (2014).

Highlighted text in bold with an asterisk from the table above denotes drying techniques of interest to this PhD thesis.

Drying of porous silicon samples has to be considered a key fabrication step to avoid cracking of the porous silicon layers due to the very large capillary forces. Drying methods such as supercritical drying, freeze-drying, drying with pentane, slow evaporation has allowed a "safe" drying of pSi layers.

1.3.3. Oxidation of pSi

Porous silicon will form a native oxide at ambient atmospheric conditions. This oxidation can be investigated using Fourier transform infrared spectroscopy (FTIR), (Gupta et al. 1991, Unagami 1980b, Borghesi et al. 1994, Ogata et al. 1995b, Lucovsky 1979).

Different absorption bands can appear due to oxidation and some of the silicon-hydrogen bands remain in some cases. The oxidation effect is very fast at saturated humidity and high-temperature conditions. Three frequency regions of interest are:

- a broad absorption around 3600 cm^{-1} which corresponds to 2.7 µm → O-H stretching vibrations;
- stretching due to the back-bond oxidation around 2080-2150 cm^{-1}, which is from 4.80 µm to 4.65 µm;
- the strongest absorption at 1000 to 1200 cm^{-1} (10 to 8.33 µm).

Thermal oxidation is employed for producing high-quality oxides on silicon surfaces. It also works well with porous silicon. A common approach for oxidizing silicon is heating it in a tube/pockels furnace for several minutes to up to 16 hours. The furnace is shown in Figure 11.

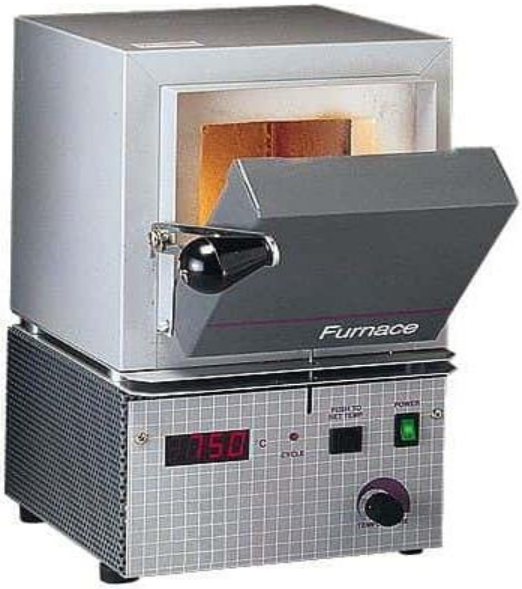

Figure 11 Furnace used for oxidising porous silicon samples.

The furnace controls the reproducibility of the process. Sample cracks are caused by thermal stresses so samples need to be placed and taken from the hot furnace carefully. The sample should be loaded at room temperature and then ramped up to the process temperature (10 ˚C/min) where it is held for the required time. Afterwards, the furnace needs cooling down before removing the sample (5 ˚C/min). A rapid thermal oxidation procedure (RTO) is better in preserving the crystalline silicon domains in pSi (Sailor 2010). RTO uses high-intensity light for heating the sample at precise temperatures for very short periods (< 1 minute) (Sailor 2010).

1.3.4. Melt intrusion in pSi

Melt intrusion is defined as pore-filling via capillary action when porous silicon is in contact with a molten substance (Canham 2014). In this section, a brief overview of methodologies used for the loading of pSi powders and free-standing membranes will be given.

Loading methodology depends on the properties of the active to be loaded, for example, some actives can be dissolved in a solvent before loading. Other actives can be loaded in the form of a concentrated liquid at room temperature or when molten at elevated temperatures. Furthermore, high payloads can be attained via dosing and drying.

Many pSi applications require pore filling with a substance of interest and it will be covered in section 1.4. Applications of porous silicon, more specifically 1.4.2. Drug delivery with porous silicon.

1.4. Applications of porous silicon

Porous silicon was first used as a mobile chip in 1969 by the Nippon Telegraph and Telephone Public Corporation (NTT) and the Sony Corporation (Canham 1997). Then, in the mid-1970s, new routes for dielectric isolation based on pSi were developed. The possible enhanced oxidation of pSi in comparison with bulk silicon allowed oxidation of porous layers within a "sandwich" structure. Since then the number of applications using pSi has proliferated and can now be divided into twelve groups: electronics, optoelectronics, optics, diagnostics, energy conversion, catalysis, filtration, adsorbents, medical, food, cosmetics, and consumer care.

The main aim of this section is to list the applications of porous silicon and relate them to their desirable properties and forms.

1.4.1. Applications survey based on relevant pSi properties

A variety of porous silicon applications are often classified based on the relevant property of pSi. Table 6 presents the required relevant pSi properties for some pSi applications. This thesis concentrates on fabrication and processing conditions optimized to achieve ultrahigh porosity for drug delivery and high surface area for gas sensing (highlighted in bold).

pSi application area	***Required pSi property***	***The desired value of pSi property***	***Reference***
Active (drug) delivery	Pore volume (porosity)	high >60% mesopores	Salonen et al. 2005 Canham 2007 Chiappini et al. 2010 Canham 2014
	Surface area	low	
Solar cells	Porosity	high >50% mesopores	Yonehara et al. 1994 Terheidin et al. 2011
Biosensing	Porosity	high >50% mesopores	Deloiuse and Miller 2004
Tissue engineering	Porosity	high >90% mesopores	Coffer et al. 2005 Sun et al. 2007
	Surface area	low	
Photocatalysis	Porosity	high >50% mesopores	Qu et al. 2010
Thermal isolation	Porosity	high >80% as-etched	Boarino et al. 1999 Nassiopoulu and Kaltas 2000
Light emission	Porosity	high >80% as-etched	Canham et al. 1994; Gelloz et al.2005; Chen et al. 2012
Gas sensing	Surface area Porosity	high low	Barillaro et al. 2003
Catalysis	Surface area Porosity	high low	Buriak 2002

Table 6 Table of relevant pSi properties required for some of the pSi applications. References from this table can be found in the Handbook of porous silicon, ed. by Leigh Canham (2014).

In Table 7, porous silicon applications together with the specific pSi forms required are listed. Applications from the left-hand side of the table require mainly powdered samples.

The central column combines all three types of pSi: powders, membranes and films. The right-hand column is mainly for chip-based pSi layers.

Porous silicon Powders	***Traditional applications of porous silicon (powders, membranes and films)***	***Porous silicon chip-based layers***
Medical	Energy conversion	Electronics
Food & nutrition	Catalysis	Optoelectronics
Cosmetics	Filtration	Optics
Consumer care	Adsorbent	Diagnostics

Table 7 Application areas of porous silicon. Adapted from (Canham 2014).

The dominant physical forms for medical applications are microparticles, nanoparticles and chips and they have been used in drug delivery, orthopaedics and tissue engineering imaging.

- Food and nutrition employ microparticles where they are used in nutrient protection, as an additive for gum and as functional foods.
- The cosmetics industry use microparticles and nanoparticles in sunscreens, foundation excipient and also for drug delivery.
- In the consumer sectors pSi microparticles are also used in oral hygiene products, shampoo and antibacterial surfaces.
- Energy conversion: batteries, solar cells, fuel cells, explosives, photoelectrodes and used all three forms: microparticles, nanoparticles and chips.
- Catalysis is used for organic pollutant removal and also for noble metal salt reduction and it requires membranes and powders.
- Electronics uses chips for RF isolation, thermal isolation and micromachining gettering.

- Diagnostics uses chips for gas sensing, mass spectrometry, biosensors and also for chemical sensors. In optoelectronics; LEDs, lasers, waveguide modulators and chips are used (Canham 1997).

1.4.2. Drug delivery with Porous Silicon

Introduction

A major application of porous silicon requiring high pore volumes is drug delivery, which can, for example, be used in particle formulations for cancer treatments. We introduce here the most relevant issues and how they are addressed with porous silicon: key properties of a drug delivery matrix, fabrication methods to tune porosity and biodegradability, surface chemistry, biocompatibility, drug loading techniques, types of drugs that have been loaded and some of the drug delivery fields explored to date.

Characteristics of an ideal controlled drug delivery matrix are: very low toxicity, complete biodegradability, tunable timescales of drug release, high drug payloads. Furthermore, reliable, inexpensive and scalable fabrication techniques are needed, such as electrochemical anodisation followed by ball milling or ultrasonication.

Required parameters

During fabrication, specific parameters can be adjusted to optimise for drug loading potential. The most important parameters are pore volume and pore size of the porous silicon. These parameters can be controlled by adjusting the current density or the concentration of electrolyte during electrochemical anodisation (see chapter 2). Pore size, for example, can be tailored by varying the current density, with larger pores being produced using higher current densities. In this way, pore size can be matched to the size of the drug molecules, which need to be smaller than the pores in order to fill them. Alternatively, the type of dopant and the

crystalline orientation of the wafer can also have a dramatic effect on pore morphology and pore size and therefore on the drug payload.

Other properties or parameters of interest for drug loading within a porous silicon matrix are the low toxicity of pSi, and surface chemistry. The level of drug affinity of pSi, for instance, is controllable by surface chemistry.

Another example of how altering the surface chemistry can better prepare the porous silicon for drug loading is via oxidation. As-anodised porous silicon has a hydride-terminated surface, which is very hydrophobic, very reactive and can quickly denature a drug. This is not favourable for a slow-release drug delivery system. Oxidation can hence help lower the reactivity by lowering the hydride concentration. In addition, oxidized pSi is hydrophilic making it compatible with water-based formulations. However, there is a trade-off as pore volume is reduced (Canham 2014).

Methods of drug loading

Before the loading procedure, pSi is oxidized and the volume of pores expands to accommodate the extra oxygen atoms. Volume expansion shrinks the pores and traps anything that is within the pores during that time.

When combined with a vinyl group polymer, control over drug release is improved and also the stability is improved. Thermodynamically speaking, the sum of the energies of the polymer is less than the sum of the energies of the individual monomers. Therefore, single bonds in the polymeric chain are more stable than the double bonds of the monomer (Canham 2014). The polymers created have relatively high molecular weights. Drug delivery applications require biocompatible polymers.

To load a drug into porous silicon a solution or liquid is required which is often in a molten state. The drug can then be loaded using a procedure such as impregnation that requires the mixing of the mesoporous material with the drug-loaded solution.

This type of loading can be performed manually. Immersion is also a widely used method for the loading of guest molecules into pSi. During immersion, load molecules are dissolved into

an appropriate solvent and are adsorbed to the pore walls. Through the careful calculation of the drug volume required to fill the pores, the molecules can be efficiently impregnated with a minimal coating of the external surfaces.

The degree of loading depends on the methods used and the molecules to be loaded, as well as how much drug is adsorbed onto the pore walls, and how much drug is left in the pores after centrifugation and filtration. Very high loadings are the most beneficial when using pSi as a drug carrier. For achieving high degrees of loading, very high concentrations of the drug have to be used (Lehto et al. 2014).

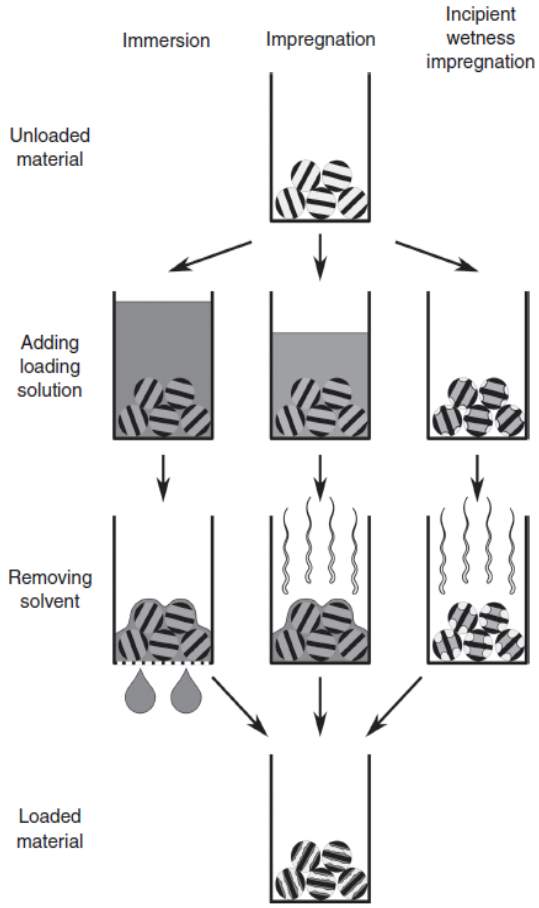

Figure 12 Methods for loading mesoporous materials (Lehto et al. 2014).

In Figure 12, methods for loading mesoporous material, such as immersion, impregnation and incipient wetness impregnation are shown. Impregnation of drugs into pSi membranes is perceived within the future work and outlook section (see chapter 5).

Having in mind the chemical view, pSi is a desirable carrier for developing drug delivery systems since surface chemical modifications are possible. Loading molecules into pSi can be achieved via different methods, such as drug/particle entrapment, covalent and noncovalent bonding etc. (Anglin et al. 2008, Tamayo et al. 2015).

Furthermore, once porous silicon has been fabricated, the resultant films need to be reduced to small particles in the order of nanometres or micrometres. Ultrasonication is the most commonly used technique for the preparation of small pSi particles.

Sonication radiation fractures the porous silicon layers/films into very small particles ranging from a few micrometres to roughly a few hundreds of nanometers (Heinrich et al. 1992). Very high power sonication can further reduce particle sizes to roughly 50 nm.

The size distribution of the resultant particles is however relatively broad and centrifugation or filtration is often additionally used for narrowing the spread (Qin et al. 2014). Psi films/membranes can alternatively be milled into powders using techniques such as rotor milling, ball milling and jet milling.

Polymers introduction

One of the main drawbacks of porous silicon is its mechanical instability. Therefore, polymers can be used to improve the mechanical stability of the porous membrane during processing. When a drug is combined with a vinyl group polymer, control over drug release is improved and the stability is likewise improved.

In addition to combining pSi with a medical drug, pSi can also be combined with polymers to form pSi-based composites for additional functionality. This has been demonstrated in the medical field of cancer therapy. For example, the surface modification of pSi nanoparticles with temperature-responsive polymers has enabled controlled drug release induced by infrared radio-frequency radiation (Li et al. 2017) and the physical encapsulation of pSi nanoparticles in pH-responsive polymers has protected GLP-1 and insulin from the harsh

conditions of the gastrointestinal tract and provided site-specific drug release in small intestines for enhanced absorption (Li et al. 2017).

Moreover, porous silicon has enormous potential and excellent loading capacity together with versatile surface chemistry, which makes it a unique candidate for chemo-immunotherapy (Shahbazi et al. 2015).

The porous layer is removed from the silicon substrate by applying electric pulses, called "electropolishing". The current after the anodisation run is elevated to detach the layer. For example, if the anodisation current used is 5 A (corresponding current density is 36 mA/cm^2), the electropolishing current is 23 A (165 mA/cm^2). At this current, the dissolving of the interface pSi layer-Si wafer occurs. The free-standing porous silicon is further rinsed with ethanol and removed using tweezers (Canham 2014).

After the anodisation procedure, gravimetric calculations of porosity and thickness are performed. Afterwards, another analysis method such as gas adsorption is carried out to characterize the samples and to compare the results.

Other parameters of interest for drug loading within a porous silicon matrix are the low toxicity of pSi, high pore volume/porosity and surface chemistry.

Afterwards, the drug has been loaded the pSi materials need to be characterised. The methods used include thermoanalytical analysis, chromatography, spectroscopy, microscopy and X-ray diffraction. This section will not investigate these methods further.

Optical methods for detection of polymers in porous silicon have been developed. A shift in the optical reflectivity corresponds to a change in refractive index and is different for each material. For example, a shift will occur after removal of a drug or from the dissolution of the pSi particle but also through oxidation of the porous silicon, which is visible from the wavelength value change (Canham 2014).

Additional drug loading methods

The simplest method for drug loading is via physical adsorption and it relies on the adsorption between the payload and pSi. This relates to the surface nature of pSi as it tends to be hydrophobic. Surface charge plays another key role. (Wu et al. 2015) is an example of a study, which has explored the role of surface charge using protein loaded into thermally oxidised pSi. Furthermore, they measured the loading efficiency of the samples. To improve stability of the pSi layer, carbonisation can be implemented, as the carbonized films show improved stability against thermal oxidation due to the full coverage of the original silicon hydride surface (Makara et al. 2003). A further advantage of this process too is the fact that after this treatment there is not a significant reduction of the specific surface area of pSi (Bjorkqvist et al. 2004). Unfortunately, one drawback is that the characteristic luminescence of pSi disappears (Kostishko et al. 2004). Other methods used to stabilize pSi are hydrosilylation and silanization chemistry (Buriak et al. 1998).

Applications

As discussed earlier in this section, pSi has proven an excellent material for applications such as loading and drug delivery of therapeutics. One therapy class is immunotherapy, effective in cancer treatments (Dai et al. 2017) and for example, micro and nanoparticles show different immunogenic profiles on the cells of the immune system (Shahbazi et al. 2014) and hence can target different cells within the body.

Nanoparticles have a potential application with vaccines since they fit into the same size ranges of the bacteria and viruses. They can also directly deliver the antigens to the blood molecules in the body (DCs population-Dendritic cell lineage).

Porous silicon can be tuned depending on its specific application and can exhibit controlled release behaviour, pH triggered release, thermal-sensitive release and photodynamic release. Different surface properties of pSi can also be adjusted by surface modification.

The range of therapy classes that use drug delivery are chemotherapy, wound repair and immunotherapy. The biodegradable nature of porous silicon is ideal for such cell therapy

applications (Canham 2014). First, the cells are delivered into the host and they directly contribute to the structure and the function of new tissues. The cells used in these therapies are usually autologic or allogenic and are typically differentiated cells that can still maintain proliferative capacity (Mao et al. 2015).

Subsequently, after delivery, the carrier should then biodegrade. PSi is a promising candidate for the treatment of ocular surfaces, where human cells are kept isolated and the cornea is extended on pSi membranes/carriers and furthermore used to demonstrate the cell growth in the animal model (Canham 2014). The immunotherapy field with nanoparticulate carriers also continues to evolve, whilst pSi is showing promise as a platform in biomedical applications with some pSi structures encouraging further exploration within drug delivery and cancer immunotherapy.

Routes of administration

There are many different routes of administration that can be used for drug delivery. The most commonly used administration routes are: intravitreal, nasal, oral, pulmonary, intra- and transdermal, subcutaneous/intramuscular and intravenous (Canham 2014). These are discussed in more detail below.

Oral delivery-Delayed release of the loaded drug from pSi microparticles is the consequence of the high rate of the unloaded drug. Some drugs cannot be used in oral delivery due to their poor pharmacokinetic properties and also due to poor solubility (Canham 2014). Poorly water-soluble drugs are common choices for contemporary drug delivery. On the other hand, the formulations which contain natural or synthetic lipids are more of interest due to their viability for enhancing the oral bioavailability of some poorly water-soluble, highly lipophilic drugs.

Subcutaneous delivery-Some peptides have promising applications in subcutaneous delivery. Furthermore, peptides and protein deliveries, in general, are challenging and current delivery systems are not particularly useful. By contrast, drug loading in pSi is a very gentle procedure and it can be performed at room temperature. Promising results for pSi based on peptide delivery systems have been obtained using pSi (Canham 2014).

Intravenous delivery-pSi can be used intravenously as a simple drug carrier, for actively targeted delivery (Canham 2014) and also for imaging options. The particles can release their payload after being captured in the liver or spleen.

Intravitreal delivery-To confirm whether pSi was a benign and biodegradable material for intravitreal use, pSi particulates were injected into the eyes of test animals and were observed over a few weeks. The results showed that pSi is non-toxic, noninflammatory and suitable biodegradable material for intravitreal drug delivery (Canham 2014).

This thesis focused its application to the intravitreal drug delivery via needle administration (see chapter 2).

The first reference of pSi being used in drug delivery applications was by Foraker et al. (2003). Here, microfabricated pSi particles were used for enhancement of insulin permeability into cell monolayer. Insulin loading into pSi was observed.

Since then, the range of drugs that have been loaded into pSi has proliferated and now comprises small hydrophobic molecules, DNA and antibodies, or more specifically: ibuprofen, griseofulvin, ranitidine, antipyrine, doxorubicin, papain, gramicidin A, peptide siRNA, ketoconazole, triclosan, ethionamide and indomethacin.

The release rate of pSi is affected by surface chemistry (Anglin et al. 2004). The drug release also depends on the behaviour of drug's dissolution (Salonen et al. 2005). The values for oral delivery are much faster than the ones for the intravitreal injections regards different kinetics achieved between the intravitreal and oral delivery. Water-soluble drugs display much faster release kinetics, where poorly soluble drugs show slow kinetics (Salonen et al. 2005). pSi particles have the ability of moderation of the drug release kinetics (Wang et al. 2009).

Conclusions

Biodegradable pSi is a very suitable material for controlled drug release particularly due to its potential to realise high pore volumes and consequentially high payloads. For example, for drug delivery applications, this thesis reported that supercritically dried porous silicon of ultrahigh porosity (90%) can preserve large pore volumes (up to 4 ml/g) and larger surface areas (600 m^2/g) than can be achieved with air-dried materials (Loni 2014).

In this section, an overview of the drug delivery and the biomedical applications, such as cancer immunotherapy, was provided. Because of its controllable geometry, tunable structure and versatile surface properties, porous silicon has unique properties that make it an ideal material for clinical applications within disease therapies. Within fabrication, there is a variety of possible techniques for producing pSi particles. Comminution of pSi is one of them and it will be discussed in Chapter 2.

1.4.2. Gas sensing with Porous Silicon

A second major application of porous silicon requiring the high surface areas fabricated in this thesis is gas sensing (see tables 6 and 7). Gas sensors are a type of the chemical sensor and this subsection focuses on two types - electrical and optical pSi gas sensors, as the state of the art. The ideal gas sensor will include the following: high sensitivity, low detection limit, high accuracy, resolution and linearity, short response time, null hysteresis and long operation time. Currently, none of the pSi gas sensors meets all these criteria simultaneously.

Some gases of interest for gas sensing with pSi are: CO_2, N_2, NO_2, SO_2, H_2S, PH_3, O_2 (Ozdemir and Gole 2007).

In the latest studies, pSi is integrated into the sensor structure, such as into Field-effect transistors (FET). Alteration to surface chemistry through carbonization, as well as metallization, can also be performed to improve the sensitivity, selectivity and reliability of performance.

All three types of porous silicon, micro-, meso- and macroporous have shown to be very effective for integrated gas sensors fabrication with low-cost processes (Miszei et al. 2007, Ozdemir and Gole 2007, Saha et al. 2008). The increased surface areas of pSi contribute to the gas sensing performance which is up to 10^7 times larger than bulk materials. It ensures a stronger interaction between the material surface and gas molecules and allows high sensitivity and a low detection limit to be achieved (Canham 2014).

Figure 13 is a schematic representation of a gas sensor fabrication process and consists of electrochemical anodisation followed by an RF-magnetron sputtering setup for depositing the active layer of the sensing electrode (Mourya et al. 2019).

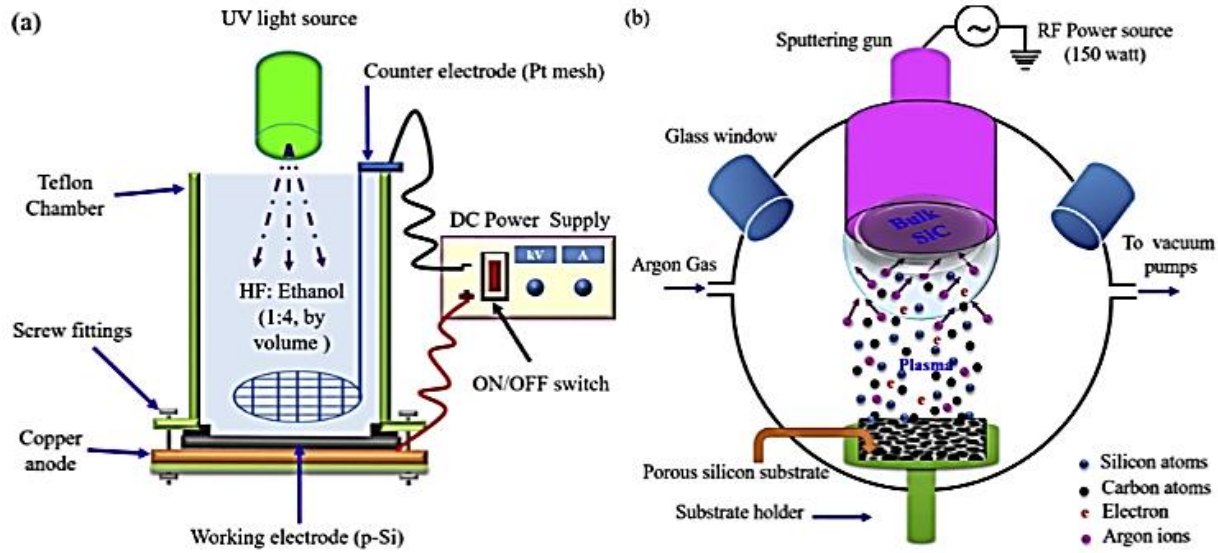

Figure 13 A schematic of sensor fabrication processes. (a) Electrochemical anodisation setup used for fabrication of porous silicon substrate. (b) RF-magnetron sputtering setup used to deposit active layer of sensing electrode.

Furthermore, gas concentration as a function of refractive index, recombination processes, dielectric constant, photoluminescence spectrum and current has been investigated (Canham 2014). In conclusion, different electrical and optical systems are used for improving gas sensor performance. For the last two decades, pSi based gas sensors have improved significantly in terms of architecture and performance.

1.5. References

Anglin EJ, Cheng L, Freeman WR, and Sailor MJ (2008) Porous silicon in drug delivery devices and materials, Advanced Drug Delivery Reviews August 17, 60(11), pp. 1266–1277.

Bellet D and Canham LT (1998) Controlled Drying: The Key to Better Quality Porous Semiconductors, Advanced Materials, *10*(6), pp. 487-490.

Billat S, Thonissen M, Arens Fischer R, Berger MG, Kruger M and Luth H (1997) Influence of etch stops on the microstructure of porous silicon layers, Thin Solid Films, 297(1-2), pp. 22-25.

Bjorkqvist M, Salonen J, Laine E (2004) Humidity behaviour of thermally carbonized porous silicon, Applied Surface Science, 222(1-4), pp. 269-274.

Borghesi A, Guizzetti G, Sassella A, Bisi O. and Pavesi L (1994) Induction-model analysis of Si-H stretching mode in porous silicon, Solid state communications, 89(7), pp. 615-618.

Buriak JM, Stewart MP, Allen MJ (1998) Lewis acid mediated functionalization of porous silicon with substituted alkenes and alkynes, Materials Research Society Symposium Proceedings, 120(6), pp. 1339-1340.

Bykov IP, Laguta VV, Glinchuk MD and Slipenyuk AM (2000) Light-induced intrinsic defects in PLZT ceramics, Physics of the Solid State, 42(12), pp. 2258-2264.

Canham LT (1990) Silicon quantum wire array fabrication by electrochemical and chemical dissolution of wafers, Applied physics letters, 57(10), pp. 1046-1048.

Canham LT (1997) Properties of Porous Silicon, INSPEC.

Canham LT (2014) Handbook of Porous Silicon. Zug: Springer International Publishing.

Canham LT, Groszek AJ (1992) Characterization of microporous silicon by flow calorimetry: comparison with a hydrophobic silica molecular sieve, Journal of Applied Physics 72(4), pp. 1558–1565

Dai W, Wang X, Song G, Liu T, He B, Zhang H, Zhang W (2017) Combination antitumor therapy with targeted dual-nanomedicines, Advanced Drug Delivery Reviews, 115, pp. 23-45.

Dillon AC, Gupta P, Robinson MB, Bracker AC and George SM (1990) FTIR studies of water and ammonia decomposition on silicon surfaces, Journal of Electron Spectroscopy and Related Phenomena, 54, pp. 1085-1095.

Dillon AC, Robinson MB, Han MY and George SM (1992) Diethylsilane decomposition on silicon surfaces studied using transmission FTIR spectroscopy, Journal of The Electrochemical Society, 139(2), p. 537.

Elia P, Nativ-Roth E, Zeiri Y, Porat Z (2016) Determination of the average pore size and total porosity in porous silicon layers by image processing of SEM micrographs, Microporous and Mesoporous Materials, *225*, pp. 465-471.

Gregg SJ, and Sing KSW (1982) Adsorption, Surface Area and Porosity (Translated into Russian) Mir, Moscow, Academic Press.

Gupta P, Colvin VL and George SM (1988) Hydrogen desorption kinetics from monohydride and dihydride species on silicon surfaces, Physical Review B, 37(14), p. 8234.

Gupta P, Dillon AC, Bracker AS and George SM (1991) FTIR studies of H2O and D2O decomposition on porous silicon surfaces, Surface Science, 245(3), pp. 360-372.

Heinrich JL, Curtis CL, Credo GM, Sailor MJ, Kavanagh KL (1992) Luminescent colloidal silicon suspensions from porous silicon, Science, 255(5040), pp. 66-68.

Kale PG, Pratibha S and Solanki CS (2012) Synthesis and characterization of Si nanoparticles obtained on sonication of porous silicon multilayer films, Journal of Nano Research Trans Tech Publications Ltd. (17), pp. 13-25.

Korotcenkov G and Cho B K (2010) Silicon Porosification: State of the Art, Critical Reviews in Solid State and Materials Sciences, 35(3), pp. 153-260.

Kostishko BM, Nagornov YS, Salomatin SY, Atazhanov SR (2004) The interface mechanisms of photoluminescence in carbonized porous silicon, Technical Physics Letters, 30 (2), pp. 88-90.

Lehmann V and Gösele U (1991) Porous silicon formation: A quantum wire effect. Applied Physics Letters, 58(8), pp. 856-858.

Lehto VP and Riikonen J (2014) Drug loading and characterisation of porous silicon materials, In Porous silicon for biomedical applications, Woodhead Publishing, pp. 337-355.

Loni A (2014) 'Porous Silicon Formed by Anodisation', in Handbook of Porous Silicon, Springer, Switzerland, pp. 163-170.

Lucovsky G, Nemanich RJ and Knights JC (1979) Structural interpretation of the vibrational spectra of a-Si: H alloys, Physical Review B, 19(4), p. 2064.

Makara VA, Klyui KI, Rozhin AG, Litovchenko VG, Piryatinskii YP, Korneta OB (2003) Porous silicon photoluminescence modification by surface treatments and impregnation of carbon based nanoclusters, Physica Status Solidi, 197(2), pp. 355-359.

Mao AS and Mooney DJ (2015) Regenerative medicine: current therapies and future directions, *Proceedings of the National Academy of Sciences*, *112*(47), pp. 14452-14459.

Mattei G and Valentini V (2003) In situ functionalization of porous silicon during the electrochemical formation process in ethanoic hydrofluoric acid solution. Journal of the American Chemical Society, 125(32), pp. 9608-9609.

Mizsei J (2007) Gas sensor applications of porous Si layers. Thin solid films, 515(23), pp. 8310-8315.

Motohashi A, Kawakami M, Aoyagi H, Kinoshita A and Satou A (1995) Gas identification by a single gas sensor using porous silicon as the sensitive material, Japanese journal of applied physics, 34(10R), p. 5840.

Mourya S, Kumar A, Jaiswal J, Malik G, Kumar B and Chandra R (2019) Development of Pd-Pt functionalized high-performance H2 gas sensor based on silicon carbide coated porous silicon for extreme environment applications. Sensors and Actuators B: Chemical, 283, pp.373-383.

Nekovic E, Storey CJ, Kaplan A, Theis W and Canham LT (2020) Supercritically-dried membranes and powders of >90% porosity silicon with pore volumes exceeding 4cm^3/g, Journal of the Electrochemical Society, 9, p. 024016.

Noguchi N, Suemune I (1993) Luminescent porous silicon synthesized by visible light irradiation. Appl Phys Lett 62(12), pp. 1429–1431.

Ogata Y, Niki H, Sakka T. and Iwasaki M (1995b) Hydrogen in porous silicon: vibrational analysis of SiH x species. Journal of the Electrochemical Society, 142(1), p. 195.

Ozdemir S and Gole JL (2007) The potential of porous silicon gas sensors. Current Opinion in Solid State and Materials Science, 11(5-6), pp. 92-100.

Park JH, Gu L, Von Maltzahn G, Ruoslahti E, Bhatia SN and Sailor MJ (2009) Biodegradable luminescent porous silicon nanoparticles for in vivo applications. Nature materials, 8(4), pp. 331-336.

Qin Z, Joo J, Gu L, Sailor MJ (2014) Porous Films: Size Control of Porous Silicon Nanoparticles by Electrochemical Perforation Etching, Particle & Particle Systems Characterization, 31 (2), pp. 252-256.

Saha H (2008) Porous silicon sensors-elusive and erudite, International journal on smart sensing and intelligent systems, 1(1), pp. 34-56.

Sailor MJ (2010) Porous silicon in practice, Wiley-VCH.

Salonen J, Laitinen L, Kaukonen AM, Tuura J, Björkqvist M, Heikkilä T, Vähä Heikkilä K, Hirvonen J, Lehto VPJ (2005) In Vivo Evaluation of Porous Silicon and Porous Silicon Solid Lipid Nanocomposites for Passive Targeting and Imaging, Journal of Controlled Release, 108, pp. 362–374.

Ed: Santos HA (2014) Porous Silicon for Biomedical Applications, 1st ed., Woodhead Publishing, Cambridge, UK.

Shahbazi MA, Fernandez TD, Makila EM, Guevel XL, Mayorga C, Kaasalainen MH, Salonen JJ, Hirvonen JT, Santos HA (2014) Surface chemistry dependent immunostimulative potential of porous silicon nanoplatforms, Biomaterials, 35(33), pp. 9224-9235.

Shahbazi MA, Shrestha N, Makila E, Araujo F, Correia T, Ramos T, Sarmento B, Salonen J, Hirvonen J, Santos HA (2015) A prospective cancer chemo-immunotherapy approach mediated by synergistic CD326 targeted porous silicon nanovectors, Nano Research, 8, p. 1505.

Tamayo A, Mazo MA, Ruiz-Caro, Martin-Illana A, Bedoya LM, Veiga-Ochoa MD, J. Rubio (2015) Mesoporous silicon oxycarbide materials for controlled drug delivery systems. Chemical Engineering Journal, 280, pp. 165-174;

Thakur M, Sinsabaugh SL, Isaacson MJ, Wong MS, Biswal SL (2012) Inexpensive method for producing macroporous silicon particulates with pyrolyzed polyacrylonitrile for lithium-ion batteries, Scientific reports, 2(1), pp. 1-7.

Thommes M (2010) Physical adsorption characterization of nanoporous materials, Chemie Ingenieur Technik, 82(7), pp. 1059-1073.

Tsuboi T, Sakka T, Ogata Y (1999) Chemical etching of porous silicon in diluted hydrofluoric acid, Solid State communications, 109(3), pp. 195-199.

Uhlir A (1956) Electrolytic shaping of germanium and silicon, The Bell System Technical Journal, 35(2), pp. 333–347.

Unagami T (1980b) Formation mechanism of porous silicon layer by anodization in HF solution, Journal of the electrochemical society, 127(2), p. 476.

Valenta R, Linhart B, Swoboda I and Niederberger V (2011) Recombinant allergens for allergen-specific immunotherapy: 10 years anniversary of immunotherapy with recombinant allergens, Allergy, 66(6), pp. 775-783.

Wu CC, Hu Y, Miller M, Aroian RV, Sailor MJ (2015) Protection and delivery of anthelmintic protein Cry5B to nematodes using mesoporous silicon particles, ACS Nano 2015, 9(6), pp. 6158-6167.

Chapter 2 Fabrication and processing of porous silicon

Author's Declaration Form

This chapter on Fabrication and processing of porous silicon (pSi) with results and discussion is based on and includes text and figures from the following published papers:

1. Communication—Supercritically-Dried Membranes and Powders of >90% Porosity Silicon with Pore Volumes Exceeding 4 cm^3 g^{-1}, ECS Journal of Solid State Science and Technology, *9*(2), p. 024016 (2020)

E. Nekovic, C.J. Storey, A. Kaplan, W. Theis, and L. T. Canham, ECS J. Sol. State Sci. Technol. 9, 024016 (2020).

2. *Preserving surface area and porosity during fabrication of silicon aerocrystal particles from anodized wafers, Journal of Porous Materials*, pp. 1-6 (2020).

Storey, C.J., Nekovic, E., Kaplan, A. *et al.* Preserving surface area and porosity during fabrication of silicon aerocrystal particles from anodized wafers. *J Porous Mater* (2020). https://doi.org/10.1007/s10934-020-00996-9

3. *A gentle sedimentation process for size-selecting porous silicon microparticles to be used for drug delivery via fine gauge needle administration, Journal of Silicon,* pp. 1-8 (2020).

Elida Nekovic*, Catherine J. Storey, Andre Kaplan, Wolfgang Theis and Leigh T. Canham

Fabrication and processing of porous silicon (pSi) with results and discussion

2.1. Porous silicon formation by anodisation

Abstract

This section demonstrates the fabrication of ultrahigh porosity structures, called “silicon aerocrystals”, via electrochemical anodisation. p+ wafers have been used for the optimization of electrochemical etching conditions and subsequent drying is demonstrated. The thickness of produced pSi membranes using supercritical drying is in the range of 41 to 210 micron. Pore volumes are from 3.5 to 5.13 cm^3/g, average pore diameters of 29 nm to 35 nm and surface areas 425 to 549 m^2/g.

Introduction

Mesoporous silicon with highly tunable morphology can be achieved by electrochemical etching of bulk silicon (Martin-Palma 2014, Sailor 2012). Nanostructures fabricated by this wet process depend on the way of drying applied, due to the huge capillary forces arising from liquid evaporation from the pores (Bellet 1998).

Previous studies have shown that ultrahigh porosity thin layers on wafers (Canham 1994), very high surface area powders (Loni 2015) and luminescent structures of high quantum efficiency (Joo 2016) can be fabricated via drying with supercritical fluids (Cooper 2003); a method that avoids the capillary forces of air drying.

In this thesis, typical anodization conditions and the highly beneficial effects of using supercritical drying for creating either thick optical quality membranes or microparticulate powders of record-high pore volumes, attractive for drug loading, are reported. The specific focus is to explore the limits of porosity (pore volume) for nanostructured mesoporous silicon and thereby the potential for very high small molecule drug payloads.

The record high pore volumes (4-5ml/g) reported here should enable high drug payloads and formulations of improved efficacy.

Experimental

Anodization and membrane preparation.

Porous silicon membranes were prepared as follows. Heavily boron-doped p-type 6-inch diameter wafers of resistivity 0.005 to 0.02 Ωcm were anodized in a double-tank anodisation cell in an ("20% ethanoic HF") electrolyte 1 volume of 40wt%HF to 3 volumes of 100% ethanol. The current density range was from 72 to 108 mA/cm^2 and galvanostatic etching was used.

Membranes were "lifted off" the wafer by using elevated current pulses of 165 mA/cm^2 at the end of anodization. The current elevation takes place at a higher current than the anodisation current. It dissolves the interface between the silicon wafer and the pSi layer. Membrane detachment occurs in the electrolyte rinse bath consisting of pure ethanol. To raise the porosity of the membranes further, some detached high porosity membranes were subjected to secondary chemical etching in a 10% "ethanoic HF" (1 volume of 40wt%HF to 3 volumes of 100% ethanol) solution for periods ranging from 1 to 6 hours.

Storage and Drying techniques

After the anodisation procedure, membrane flakes were collected and stored in ethanol. The idea was that each wafer provides two batches – one for subsequent air drying at room temperature; the other for supercritical drying (SCD) in a Quorum Technologies Limited K850 critical point drier. Ethanol storage times before drying were in the range of 24 to 120 hours. The standardised SCD process has been described in detail previously (Loni 2015), but to summarise it involved flushing ethanol out with liquid CO_2, converting the liquid CO_2 to supercritical CO_2, further flushing of the supercritical CO_2, and then venting the supercritical fluid once. This process took 65 to 85 minutes.

Gas adsorption/desorption analysis

To determine pore volume, surface area and average pore diameter for each powder, nitrogen gas adsorption/desorption analysis was carried out using a Micromeritics Tristar 3020. The Barret-Joyner-Halenda model is used for computational analysis of the isotherms;

the surface area is determined via the Brunauer-Emmett-Teller method, and the average pore diameter was estimated from the adsorption branch (4V/A) method by BET. Pore size distributions were performed by computational analysis of the adsorption branch using the BJH method. Furthermore, pore volume values obtained from gas adsorption were converted to porosities and compared to those obtained from the gravimetric data. Gravimetric data for both porosity and thickness were determined from calculations using the wafer diameter and density of silicon with 3 weights w_i=initial weight of the Si wafer before anodization; w_f=final weight of the Si wafer (after pSi has been detached); w_{psi}=weight of porous silicon membrane.

Electron microscopy

High-Resolution Scanning Electron Microscopy (HRSEM) was used to study morphology using a Philips XL30 ESEM-FEG microscope and a voltage of 20keV electron beam with prior nm-scale Au coating of membrane surfaces to minimize beam charging.

Results and Discussion

In this experiment, the colours of pSi membranes were investigated. The colour changes as the function of the porosity and thickness. Figure 14 shows how the colour changes with increasing porosity at a given thickness from (a) the grey of bulk silicon to dark brown to orange-brown to a light tan colour, even for high thicknesses of tens of microns.

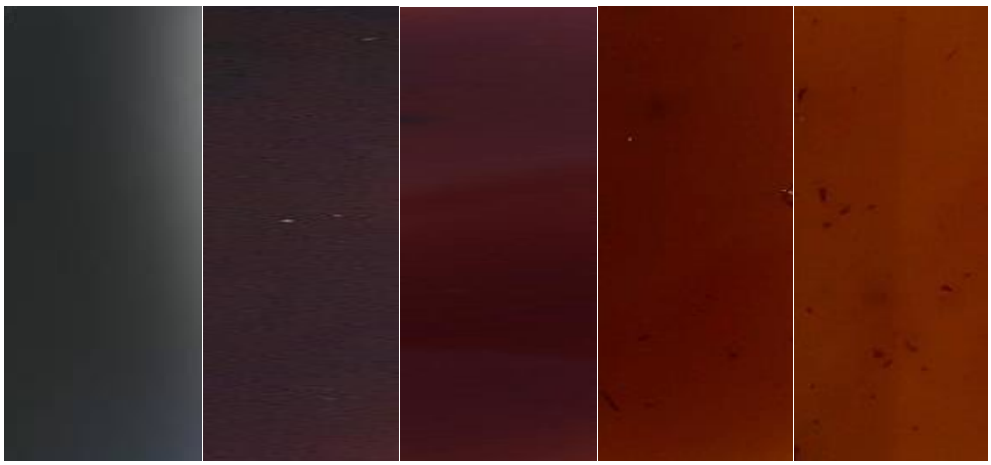

Figure 14 Optical images of Si wafer (thickness of 650 microns) and membranes of varying porosity but the constant thickness of 55 microns. (a) 0% (bulk Si) (b) 84% (c) 87% (d) 90% (e) 93%. The images (b-e) are from an anodized membrane of 81% porosity that was etched in 10% ethanoic HF for increasing periods of 1,2,3 and 5 hours, respectively.

The membranes with porosities greater than 90% were mechanically very fragile but with good optical transparency. Light scattering is low and therefore, the text through them is readable as shown in Figure 15. The structure of the membrane depends on the drying type. The shrinking and cracking appear during air-drying, Figure 16. This resulted in consistently lower pore volumes of air-dried structures, as quantified by gas adsorption data. Table 8 summarizes porosity and thickness values from gravimetric data, with surface area and mean pore sizes from gas adsorption data analysis. General trends apparent are that the SCD membranes have substantially higher pore volumes and mean pore sizes but only slightly higher surface areas than the AD equivalents. This is in contrast to anodized p- wafers where the primary benefit is greatly enhanced surface areas (Loni 2015).

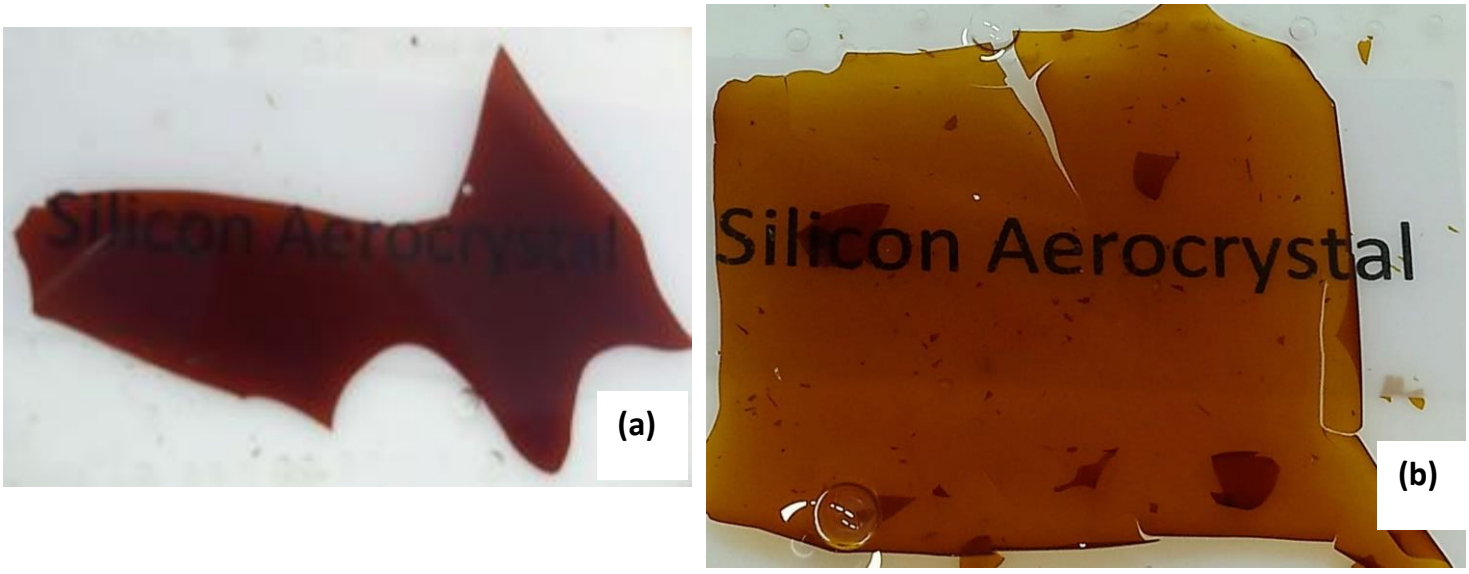

Figure 15 Optical images of an ultrahigh porosity membrane (porosity 93%, thickness 55 microns) during in-situ etching in 10% HF for (a) 2hrs and (b) 5hrs.

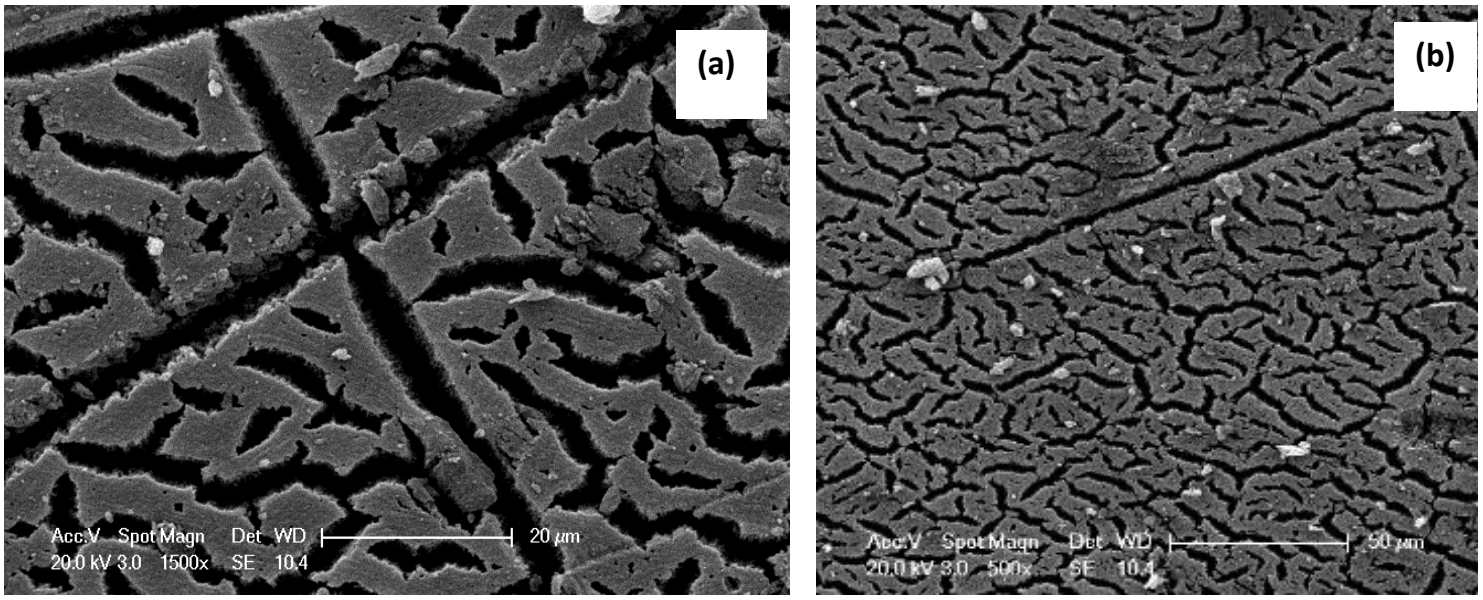

Figure 16 Cracking and shrinking investigated via different magnifications used HRSEM plan view image of the upper face of a 91% porosity membrane (UOB30) subjected to air-drying via ethanol evaporation, (a) 1500 x magnification and (b) 500 x magnification.

Sample Code	Thickness (µm) (gravimetric)	Porosity (%) (gravimetric)	Pore volume (ml/g) : AD/SCD	Porosity from pore volume (%) AD/SCD	Surface area(m^2/g): AD/SCD	Mean Pore size (nm): AD/SCD
UoB 60/61	*41*	*86.7*	*3.05/4.55*	*87.6/91.4*	*517/520*	*20/35*
** UoB 30*	*145*	*NM*	*1.34/4.22*	*75.7/90.8*	*322/425*	*17/34*
UoB 49	*174*	*89.8*	*2.83/3.52*	*86.8/89.1*	*459/462*	*25/31*
UoB 20	*195*	*NM*	*2.65/5.13*	*86.0/92.3*	*520/549*	*16/31*
UoB 40	*210*	*92.8*	*1.88/4.24*	*81.4/90.8*	*478/497*	*12/29*

Table 8 A set of five AD vs. SCD pSi membranes. Gas adsorption and gravimetric data of five supercritically dried membranes and their air-dried equivalents. *UoBXX" values denote the wafer batch codes representing distinct anodization runs at the University of Birmingham (UoB).* "NM": not measured. *UoB 30 is fabricated via anodization and further chemical etching for 5.5 hours and the rest of the membranes are via anodization only. Uncertainties are as follows: ± 1 µm (0.5 %) for thickness, ± 0.08 ml/g (0.08%) for pore volume, ± 6 m^2/g (1%) for surface area and ± 1.5 nm (5%) for mean pore size.

Regards comparison of AD and SCD membranes: the range of pore volumes of air-dried membranes are from 1.34 ml/g to 3.05 ml/g and it corresponds to porosities from 75.7% to 87.6%. In the other hand, for SCD membranes the pore volumes are in the range from 3.52 ml/g to 5.13 ml/g and the porosities are from 89.1% to 92.3%.

Figure 17 shows the isotherms of AD and SCD UoB 20, a structure with a record high pore volume greater than 5 ml/g. The corresponding extracted pore size distributions are shown in Figure 18. In the SCD structure pores up to 100 nm in diameter make a significant contribution whilst in the AD structure, the majority of pores are under 50 nm wide, as the results suggest. This 92.3% porosity structure was investigated by HRSEM and example plan view and cross-sectional images are shown in Figure 19 and 20. Gravimetric data on thickness was found to consistently yield slightly higher values than SEM values, as expected due to accuracy of weighing and some membrane thinning during anodization and chemical etching which becomes more and more significant, the higher the porosity and thickness (etch duration) of the membranes.

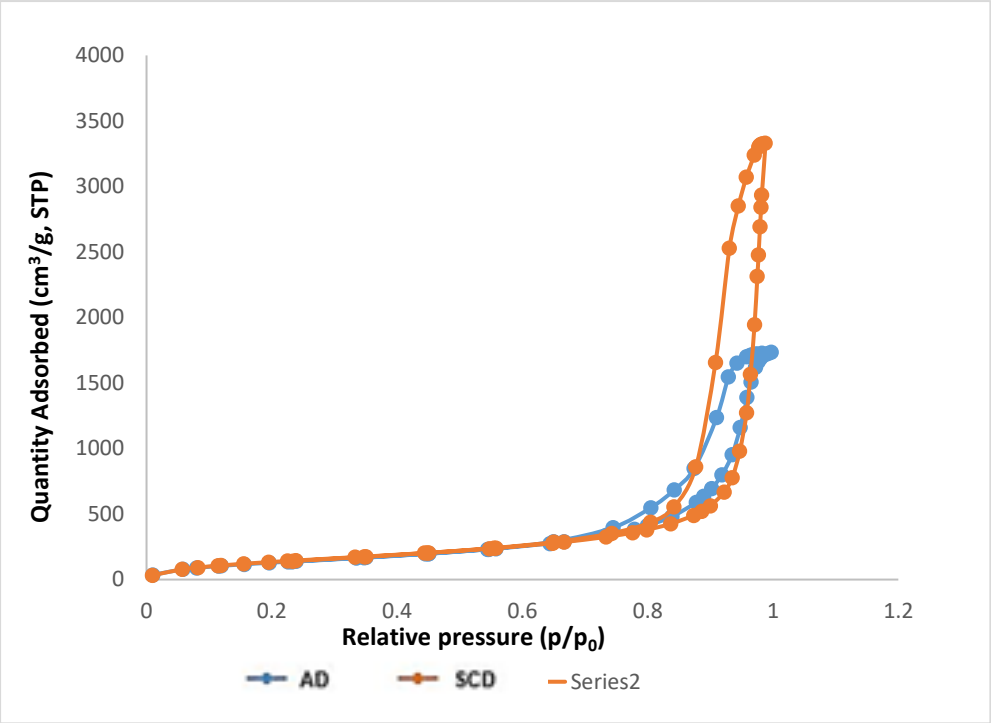

Figure 17 Isotherms for air-dried (AD) structure and its supercritically-dried (SCD) equivalent of UoB 20.

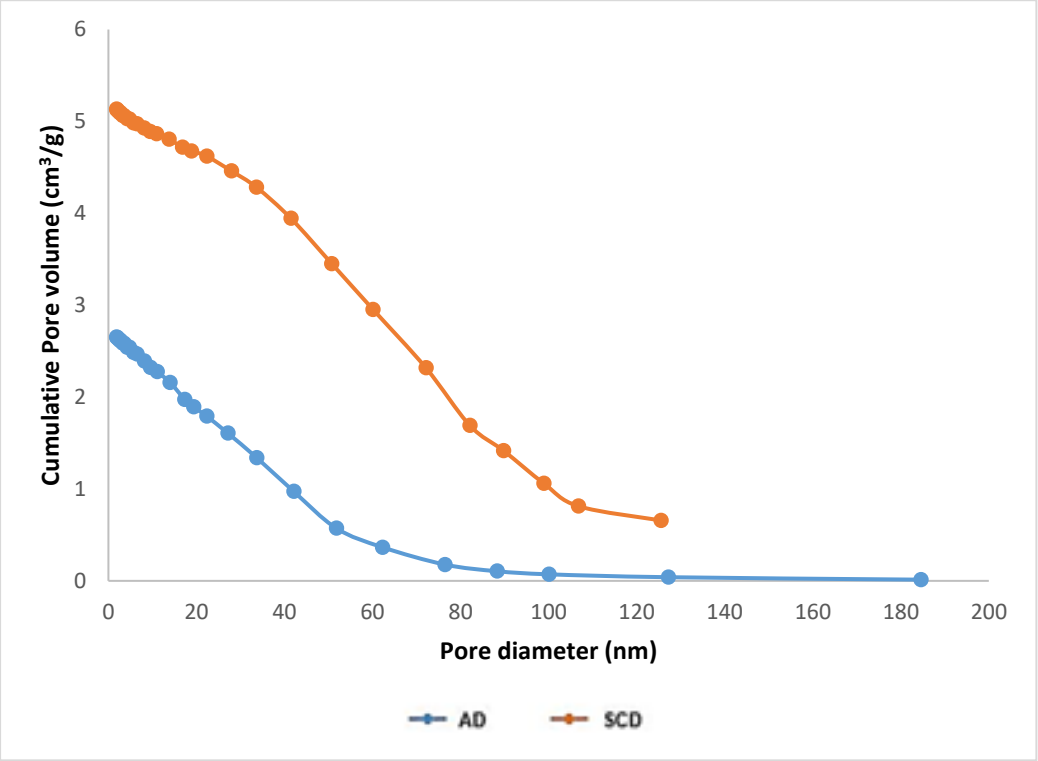

Figure 18 Pore size distributions (incremental pore volume) for air-dried (AD) structure and its supercritically-dried (SCD) equivalent of UoB 20.

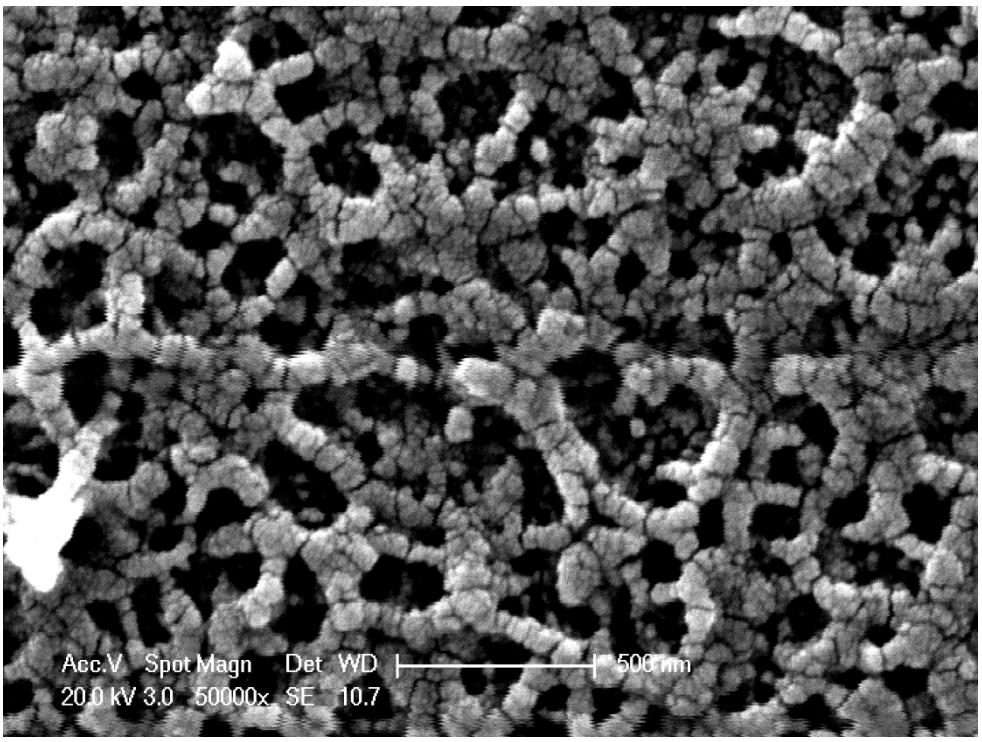

Figure 19 HRSEM plan view image of SCD UoB 20 membrane.

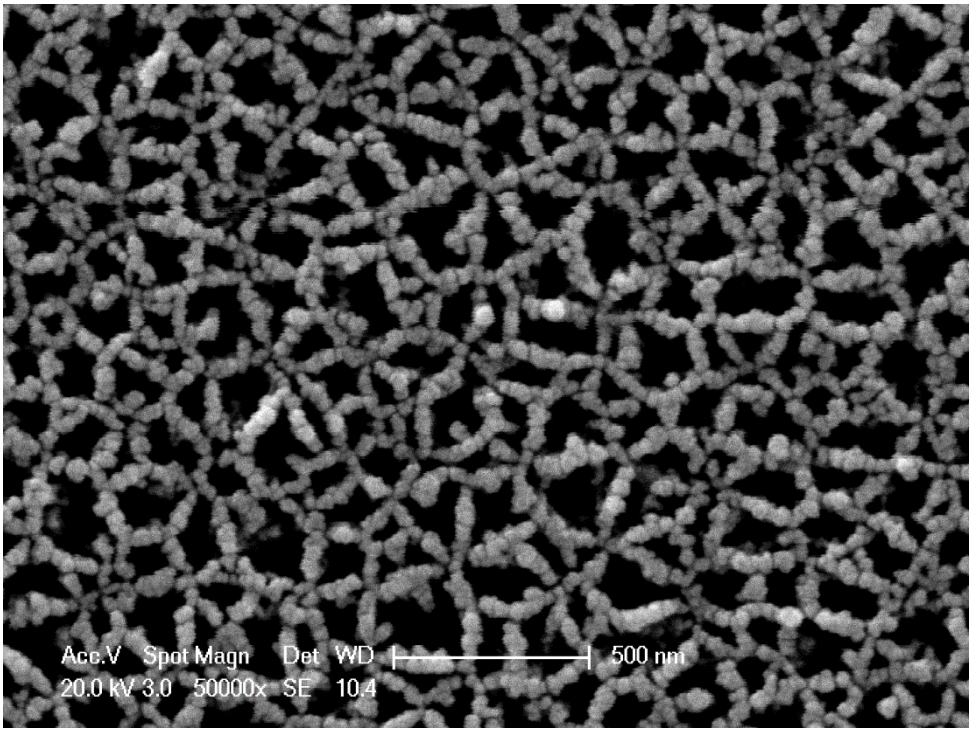

Figure 20 HRSEM plan view image of SCD UoB 30 membrane.

HRSEM image (Figures 19 and 20) of the bottom face network discovered a honeycomb structure of interconnected silicon nanowires of mean width 51 +/- 10 nm. Their morphology appears similar to that of the much smaller "quantum wires" of width <3 nm observed by HRTEM in high porosity luminescent porous silicon (Billat 1997). Nevertheless, the fluctuating nanowire widths evident in Figure 19 may be a consequence of the Au coating used here, and this will need further investigation in the future. Such Au coatings will also lead to an underestimation of porosity and pore sizes and an overestimate of mean silicon nanowire width generated under these etching conditions.

The definition of a "pore" becomes vague in the case of ultrahigh porosity structures, which are created by adjacent cylindrical pores merging into 3D voids. It is observed that the voids between nanowires on the very outer gold-coated surface of the UoB20 membrane have a wide size distribution in the range 30-130 nm with a mean value of 72 nm. Cross-sectional HRSEM images of gold-coated fracture surfaces (Figure 21) gave a lower mean nanowire to nanowire separation of 56 +/- 20 nm. Gas adsorption data, reflecting the entire volume of the same membrane and on as-etched structures gave a mean "pore" size of 31 nm (Table 8). We expect both membranes faces to have significantly larger void dimensions than the membrane bulk because the top face has received the longest chemical etch during anodization and the bottom face received the higher current pulse to achieve "lift-off". The plan for future studies is to utilize image processing techniques (Elia et al. 2016) to better compare estimates of overall porosity, pore/void size and skeleton size distributions from both HRTEM and HRSEM with that of gas adsorption analysis. This will necessitate the avoidance of even ultrathin (<4 nm) Au coatings.

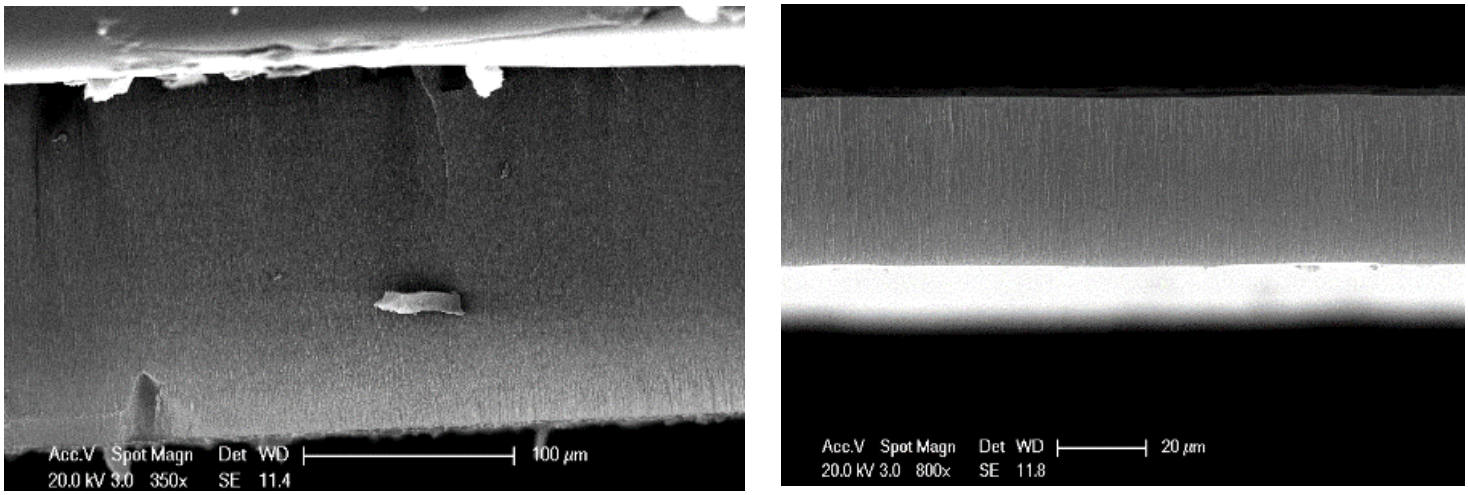

Figure 21 HRSEM cross-sectional images of SCD UoB 20 and UoB 60/61 membranes.

Checking for micro-cracking within the pores can be done using cross-sectional HRSEM. It qualitatively assesses surface roughness and checks the accuracy of gravimetric techniques (Brumhead 1993) in measuring overall porosity and thickness of these aerocrystal structures. Figure 20 shows an image for the highest porosity (UoB20) structure. All SCD membranes had far better structure throughout their thicknesses, although they are mechanically fragile (cf. macro-crack in figure 16).

Multiple measurements yielded mean thicknesses of 189 microns (UoB20) and 39.6 microns (UoB60/61), in comparison with the gravimetric values of 195 microns and 41.5 microns respectively. The gravimetric method assumes no layer thinning during etching and thus overestimates thickness by 3 % (UoB20) and 5% (UoB60/61), as the standard deviation calculations showed.

This study has also shown a general trend with anodized p+ wafers in substantially higher pore volumes of SCD membranes and mean pore sizes but only slightly higher surface areas than the AD equivalents. Furthermore, this is in contrast to anodized p- wafers where the primary benefit is greatly enhanced surface areas (Loni 2015).

Conclusions

In this section, the focus was on achieving ultrahigh porosity and thick membrane structures suitable for silicon aerocrystal particle generation. In order to achieve this goal, the electrochemical etching and drying conditions were optimized. Mesoporous membranes with porosities exceeding 90% and surfaces areas in the range 443-549 m^2/g can be achieved directly under specific anodisation conditions, or via a two-step process of anodization plus subsequent chemical etching.

The highest pore volumes (4-5 ml/g) achieved to date in mesoporous silicon membranes were reported here. Supercritical drying with carbon dioxide has shown to be beneficial over air-drying from ethanol in preserving the highest pore volumes and surface areas generated by particular etching conditions.

There is a consistent trend with anodized p+ wafers having substantially higher pore volumes of SCD membranes and mean pore sizes but only slightly higher surface areas than the AD equivalents. This is in contrast to anodized p- wafers where the primary benefit is greatly enhanced surface areas (Loni 2015).

Fabricated silicon aerocrystal can be of benefit to drug delivery applications. Such studies are planned (see chapter 5).

2.2. Formation of pSi particles (Ball milling and Ultrasonication)

Abstract

As already introduced in Chapter 1, porous silicon particles can be generated from fabricated layers via mechanical milling and ultrasonic fragmentation. The milling technique can be used for the generation of large microparticle quantities. Nanoparticles can be fabricated via ultrasonic fragmentation. However, the disadvantages are very long processing times and low yields. The porosities and surface areas of porous silicon particles are also different from untreated materials. Higher particle yields can be achieved via ball-milling but it is much more damaging than ultrasonic fragmentation, which is predominantly promising for silicon aerocrystals since processing times are reduced whilst yields are simultaneously raised with ultrahigh porosity structures. It has also been found that ultrahigh surface areas (>500 m^2/g) can be entirely conserved using ultrasonic fragmentation.

Introduction

One of the main advantages of mesoporous nanostructured silicon is the tunability of its properties. Electrochemical etching is a technique for nanostructuring semiconducting silicon (Sailor 2012). Crystalline silicon nanostructures with tunable porosity (20-95 %), pore sizes (1.5-50 nm) and surface areas (100-1125 m^2/g), initially in the form of layers (Canham 2018), can be generated. This physical form is utilized by many chip-based applications. *In-vivo* applications such as biomedical therapy require microparticles or nanoparticles for a range of, which exploit the medical biodegradability and very low toxicity of mesoporous silicon (Sailor 2012). Different methods are available for converting porous silicon (pSi) films to

particles such as mechanical milling (Bellet et al. 1998, Canham et al. 1994, Loni et al. 2015) and ultrasonic fragmentation (USF) (Heinrich et al. 2012, Chiste et al. 2019).

One of the interests of this doctoral thesis is to minimise any decrease in porosity and surface area due to such processing. This is very important for possible drug delivery applications. Parameters of interest are the speed of processing and yields. Furthermore, porosity and surface area are crucial for determining the performance. Examples are the porosity determining drug payload and the surface area determining sensor limit of detection. Nonetheless, in most studies concerning USF of pSi (Heinrich et al. 1992, Chiste et al. 2019, Hwang et al. 2020) yields are not provided. Table 9 shows data from two exceptions, together with results from this study. In one prior study (Hon 2012), pSi nanoparticles of 80-120 nm are obtained from 20um thick, electrochemically etched p-type membranes. A 24 hour USF process, followed by filtering and centrifugation steps, generated a nanoparticle yield of only 0.2 %. In the other hand, electrochemical etching, employing a perforation etch procedure to create weaker, easily fractured, high porosity regions within the overall porous layer structure have successfully produced a 24% yield of nanoparticles (150-350 nm in range, z-average 238 nm ± 5) in combination with a 16 hour USF step, sedimentation and centrifugation (Roberts et al. 2017). This latter study suggests that USF processing time and yield can be greatly improved by starting with ultrahigh porosity, which also significantly improves payload in drug delivery applications (Nekovic et al. 2020), as introduced in the previous section.

A specific type of etching, perforation etching used before dry ball milling (BM) (Nissinen et al. 2016) enabled small particle sizes in the sub-micron range, with reported yields ~100%, and material porosities of around 68% appear to have largely withstood the aggressive milling forces. Wet ball milling (in water or isopropanol) of non-porous silicon microparticles had shown a 97% yield of submicron particles after 5 hours of processing. (Canham 2007) However, wet BM has not been utilized extensively with porous silicon feedstocks (Osminkina 2018). Applications which benefit from ultrahigh porosity materials should benefit from more gentle techniques to preserve the delicate internal pore structures.

Study	*Method of Etching and Drying*	*Layer porosity (%)*	*Comminution method*	*Comminution Time (mins)*	*Particle size (nm)*	*The yield of particles (%)*
Nissinen 2016	PE & AD	69	BM	2-15	<1000	~100
Roberts 2017	PE & AD	N/A	USF	960	150-350	24
This study	SE & AD	92	USF	240	<1000	16
This study	SE & SCD	85	BM	1	<1000	5
This study	SE & AD	88	USF	30	<1000	3
Hon 2012	SE & AD	70	USF	1440	80-120	0.2

Table 9 Processing times & yield data for generating nanoparticles from pSi membranes. SE: Standard Etching, PE: Perforation Etching, SCD: Supercritical Drying, AD: Air Drying, BM: Ball Milling, USF: Ultrasonic Fracture.

The comminution process results in a significant decrease in total porosity. Advantages of BM are time (fast), inexpensive and highly repeatable. Disadvantages are mechanical aggression and a significant decrease in the porosities of delicate materials. USF is broadly used in the preparation of pSi micro and nano-particles, but as far as we are aware, there have been no studies documenting its effect on porosity and surface area in comparison with other techniques. In this study, a series of experiments quantifying yields, processing times, and the reduction in both surface areas and porosities for generating sub-micron particles by both ball milling and USF are conducted. As previously mentioned in Chapter 1, Supercritical drying preserves the porosity of highly porous pSi material (Nekovic 2020, Loni 2015). SCD membranes of initial porosity are used. Comparisons can also be made of damage caused by drying with damage caused by comminution.

Experimental Methods

Preparation of porous silicon layers and membranes.

Porous silicon membranes were fabricated via electrochemical anodisation using 20% ethanoic hydrofluoric acid electrolyte. The current densities range was from 108 and 130 $mAcm^{-2}$. Anodisation time was 1 hour. Electropolishing current densities applied were in the range of 165 and 180 $mAcm^{-2}$ for detaching the pSi membrane. Achieved

porosities were in the range of 65.2 % to 92.3 %. The thickness was between 163 µm and 195 µm.

Drying techniques

Air drying (AD): Ethanoic HF electrolyte was rinsed with ethanol after anodisation procedure. The ethanol was then evaporated in a Genlab drying cabinet at the temperature of 50 ^{o}C. Supercritical drying (SCD) was carried-out directly from ethanol storage, using a Quorum Technologies Ltd K850 critical point drier. SCD consists of repeated fill, soak and flush cycles, ethanol was replaced with liquid CO_2. The temperature and pressure are then raised to a critical point. The supercritical fluid was consequently expelled slowly from the system to dry the pSi flakes without capillary forces.

Comminution techniques

- Ultrasonic Fragmentation (USF): An amount of 0.1 g or 0.2 g of pSi membrane flakes were placed in a glass beaker. They were immersed in 10 ml or 20 ml of ethanol and sonicated using a 30W, Fisherbrand FB15051 ultrasonic bath from 30 minutes to 4 hours.
- Ball milling (BM): pSi membrane flakes of amounts between 0.2 g and 5.8 g were dry milled in the air using either a 45 ml or 500 ml zirconium oxide grinding bowl and a Fritsch planetary ball miller at 300 rpm for 1 minute. The material is then filtered out using a sieve and a brush in order to collect all the material.

Characterisation

- Particle sizing was performed using ethanol dispersions and laser diffraction in a Malvern Mastersizer 2000.
- Gas adsorption analysis (Micromeritics Tristar 3020) was used to investigate the pore characteristics of particles. Pore volumes were calculated by computational analysis of adsorption isotherms via the Barret-Joyner-Halender (BJH) adsorption method. Porosity was successively calculated from the pore volume and solid volume of silicon utilising the density of silicon (2.33gcm^{-3}); surface area using the adsorption isotherm branch via the Brunauer-Emmett-Teller (BET) method; and pore diameter using the adsorption average.

- Error limits for the surface area are ±6m^2/g, pore volume +/-0.08ml/g and pore diameter + / - 1.5 nm defined by standard silica-alumina calibration material. Membrane thickness was estimated by gravimetric analysis.

Results & Discussion

Experiment 1: Ball Milling (AD & SCD)

Ball-milling can produce much smaller particle sizes in comparison to other types of milling, such as rotor-milling. The two key components are the grinding bowl and grinding balls, which are made of zirconium oxide grinding bowl and balls in order to prevent metal contamination. The grinding bowl is first charged with the balls and then a known volume of flakes added. The lid is clamped onto the bowl and then held in place on a rotating platform. As the platform rotates, the bowl rotates in the same direction about the central platform axis and contra rotates about the vertical axis through the centre of a bowl (pseudo planetary motion). Centrifugal forces act in a way of grinding the flakes to a fine powder between the internal surfaces and the grinding balls. The main process parameters are platform rotation speed (up to 600 rpm) and time. Others include grinding bowl volume and the number and size of grinding balls used.

The main aim of this experiment was to quantify the effect of BM on different porosities. The materials used were samples UoB 99 & UoB 100, with 5.8 g and 5.1 g of SCD and AD pSi particles respectively. BM time was 1 minute. A very prompt reduction of particle size can be achieved using BM. As we can see from Table 10-from an initial porosity of 85%, around 5% of particles are already at submicron after a single 1 minute of processing).

The damage is evident in Table 11 Comminution results in a 37% reduction in surface area and a 46% reduction in pore volume for SCD material. This reduction in surface area is markedly higher than that of air-drying which was only 5%.

Sample Details	*Volume fraction of particles <0.1 µm*	*Volume fraction of particles <0.5 µm*	*Volume fraction of particles <0.9 µm*	*The yield of <1 µm particles concerning starting volume)*
SCD	2.3%	21.4%	82.3%	4.6%

Table 10 Particle sizing data of SCD sample (UoB 99) after 1 min BM. UoBXX values are wafer batch codes representing distinct anodisation runs at the University of Birmingham (UoB). The d *value represents particle diameter in microns, and the values shown in the table refer to the cumulative volume of particles below this size as a percentile.*

Ball milling		*Surface Area (m^2/g)*	*Pore volume (cm^3/g)*	*Average pore diameter (nm)*	*Porosity (%)*
SCD	Before	400	2.4	23.0	84.9
	After	251	1.3	19.3	74.9
AD	Before	320	0.8	10.1	65.2
	After	304	0.7	9.9	63.4

Table 11 Degradation in surface area and porosity of SCD (UoB 99) & AD (UoB 100) samples before and after BM. Membrane thickness of 163 µm (AD material) 196-206 µm (SCD material).

Experiment 2: Ultrasonic Fragmentation (SCD) vs time

To demonstrate how USF effects high porosity (90%) material, two 100mg sub-samples of SCD pSi flakes (UoB 98) were immersed separately in 10ml of MeOH. They were sonicated for 1.5 or 4 hours before air-drying overnight in a drying cabinet at 50°C. For a control sample, a 100mg sub-sample was taken from the same SCD sample and immersed in 10ml MeOH for 1.5 hours without sonicating and dried as above. All the samples were analysed using gas adsorption analysis to define pore characteristics and were compared to as-received material (Table 12).

There are less destruction and a slower particle size reduction to the material using USF. There is a minimal decrease in the surface area for the air-dried control sample (<0.5%). This data is in comparison to 'as-received' material, whilst surface areas of USF samples have increased slightly (0.9% & 2% respectively for 1.5 hours & 4 hour sonication times).

A noteworthy reduction in pore volume, pore diameter and porosity (21%, 19.4% and 2.6%, respectively) is seen in the air-dried control sample. In contrast, reductions are only marginally elevated after 1.5 hours of USF (26.4%, 27.4% & 3.7%) and practically no additional damage is seen after 4 hours (26.4% & 28.9% & 3.7%). Accordingly, the majority of damage seen here is a result of air drying from the methanol solvent.

Air drying post-USF from a low surface tension solvent such as pentane may further reduce damage caused due to air drying and is under investigation.

Sample Details	***Surface area (m^2/g)***	***Pore volume (cm^3/g)***	***Average Pore Diameter (nm)***	***Porosity (%)***
As-received material	453	3.7	32.5	89.5
Control	451	2.9	26.2	87.2
1.5 hours USF	457	2.7	23.6	86.2
4 hours USF	462	2.7	23.1	86.0

Table 12 Pore characteristics of pSi material UoB 98. Membrane thickness of 182 µm.

Experiment 3: Ultrasonic fragmentation of aerocrystal (AD vs SCD)

An ultrahigh porosity (92%) anodised porous silicon membrane (UoB 20) which had been stored in ethanol without prior drying, was divided into three equal subsamples before either supercritically drying, air drying or USF for 4 hours followed by air drying in a drying cabinet. (Table 13 & 14).

Sample Details	***d(0.1) µm***	***d(0.5) µm***	***d(0.9) µm***	***Yield <1 µm particles (% volume)***
USF+ AD	0.8	2.5	8.9	16.3

Table 13 Particle sizing data of sonicated and air-dried UOB 20.

Sample Details	*Surface Area (m^2/g)*	*Pore Volume (cm^3/g)*	*Average Pore Diameter (nm)*	*Porosity (%)*
SCD	549	5.1	31.3	92.3
AD	520	2.7	16.3	86.3
USF – 4 hours	633	1.5	8.1	77.7

Table 14 UoB20 - Comparison of pore characteristics. Membrane thickness of 195 µm.

A dramatic improvement in the comminution speed by USF was for the highest porosity and mechanically weakest, (92%) material. The yield was 16% yield of submicron particles within 4 hours is observed. This compares adequately with the study of Hon [15] (Table 14). The material of 70% porosity material required 24 hours of processing for 0.2% yield of smaller nanoparticles. USF over longer periods, such as 16 hours used in (Roberts 2017) would generate yields well above 20%. Table 14 proposes that extended USF does seem to the substantially lower pore volume whilst surface areas are increased. This requires further investigation.

Experiment 4: Drying damage vs Comminution Damage

Three pSi membranes of comparable properties (UoB 22/23/25 - 88% average porosity) were combined before subdividing into approximate 0.2g sample sizes. Comparison of damage caused by drying, as well as USF & BM techniques was performed. Sub-samples were subjected to two different drying techniques, such as air-drying and supercritical drying. Furthermore, it is USF for 30 minutes in ethanol and then air-dried, or ball-milled following air-drying. Particle sizing was also performed. The results are presented in Tables 15 and 16.

The conclusion of the results is that the higher the initial porosity, the higher the submicron particle yield. This is particularly noteworthy in the ultrahigh porosity range. For example, the BM of UoB 22/23/25 (initial porosity of 88 %) compared with BM of UoB 99 (85 %) compared favourably with sub-micron yields up to 9% from 5%. There is the harm in porosity such as 23% drop versus a 10% drop, respectively, due in turn to a larger proportion of weaker, narrower, or more fragile pore walls, which are more susceptible to collapse.

BM for only 1 minute contributes a higher submicron particle yield than material sonicated for 30 minutes with 9 % versus 3 %, respectively, as seen in Table 15. However, the use of thinner membranes (eg. 10-50 micron) than carried-out here (150-200 micron) is likely to significantly increase yield via USF.

A short 30 min USF showed no decrease in porosity beyond that caused by air-drying (Table 16). It is proposed that during USF the solvent provides some support to the fragile pore walls, which are thus less prone to damage. Damage occurred at the expected air-drying stage (reductions of 3 % in surface area, 64 % in pore volume, 64 % in pore diameter, and 18 % porosity below our benchmark SCD values) is due to capillary condensation forces acting upon the delicate pore walls. The destructive nature of BM is reflected in an even greater overall reduction (23 % in surface area, 74 % in pore volume, 67 % in pore diameter, and porosity 26 % below benchmark).

Particle sizing data (Table 15 and Figure 22) display a narrower size distribution for USF particles compared with BM particles, with a spread of 31 µm and 51 µm, respectively, between the 10^{th} and 90^{th} percentiles of this high porosity material.

Sample Details	***d(0.1)µm***	***d(0.5)µm***	***d(0.9)µm***	***Yield <1 µm particles (% volume)***
AD + BM	1.2	9.8	51.9	9.3
USF + AD	2.3	11.3	33.4	2.9

Table 15 Particle sizing data of UoB 22/23/25 - 15A, 60 minutes. Membrane thickness: 190 µm, 187 µm &183 µm respectively. Membranes pooled together.

Sample Details	***Surface Area (m^2/g)***	***Pore Volume (cm^3/g)***	***Average Pore Diameter (nm)***	***Porosity (%)***
SCD	560	3.1	22.4	87.8
AD	543	1.1	8.1	71.9
USF – 30min	568	1.2	8.3	73.6
AD + BM	430	0.8	7.4	65.0

Table 16 Pore characteristics of UoB 22/23/25.

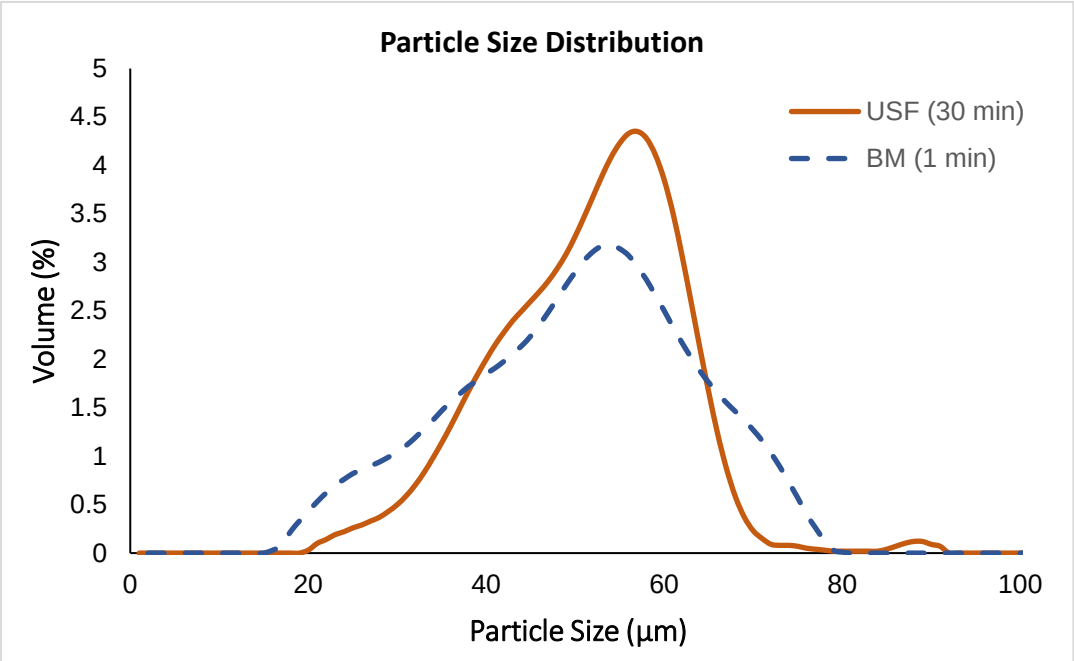

Figure 22 UoB 22/23/25 particle size distribution after 30 minutes USF or 1 minute BM.

Conclusions

Previous studies established that the speed of particle size reduction, as well as the yields of pSi nanoparticles generated by BM or USF, are improved significantly using perforation etching (Qin 2017, Nissinen 2016, Roberts 2017). From data on those parameters alone (table 1), BM would appear vastly superior to USF. However, a radically different picture emerges when the destructiveness with regard surface area, pore volume and pore size, is quantified before and after processing. Here, perforation etching was not used because of the main interest in exploring the limits of ultrahigh mesopore volume in particles for drug delivery and etching conditions have been optimized to achieve this (Nekovic 2020).

In this study, it was confirmed that significant reductions in pore volume can occur in some circumstances with both BM and USF. Surface areas are not adversely affected by USF however and can increase slightly. It was also shown that the yields after defined periods of USF are significantly raised at ultrahigh porosities (>85 %). USF would consequently appear particularly attractive for applications that need silicon nanoparticles of very high surface areas (>500 m^2/g) and moderate to high pore volumes.

2.3. Effects of drying and humidity variations during storage

This section explores how damaging air-drying followed by storage in ambient air, of varying humidity, might be for large, highly porous microparticles. Large decreases in the porosity of dry size classification processes would strengthen the need for wet processing, before drug loading, to enlarge payloads (Nekovic et al. 2020).

Lengthy storage in air of varying humidity causes water adsorption-desorption induced stresses, affecting the pore characteristics and structural integrity of SCD pSi material, as it can be seen in Table 17. Throughout fabrication and processing, it is also frequently necessary to repeatedly soak the pSi (in a solvent such as methanol) and then re-dry, for example after anodisation and then again after wet surface treatment. Recurrent exposure of high porosity silicon microparticles to a methanol solution was hence undertaken to ascertain what degree of damage might be sustained in such circumstances. A methanol-water mixture rather than pure water was used to wet the very high porosity hydrophobic microparticles. To guarantee no damage was caused before these trials, the pSi material had been supercritically dried, a technique is known to preserve high porosities (Nekovic et al. 2020).

Gas adsorption analysis was carried out to calculate the initial pore volume & pore diameter of a 100 mg SCD pSi sample before and after soak & dry cycles.

No. of MeOH:DI (50:50) soak & dry cycles	*BET surface area (m^2/g)*	*% change of BET surface area*	*BJH Pore volume (cm^3/g)*	*Porosity from Pore volume (%)*	*% change of Porosity from Pore volume*	*Average pore diameter (nm)*	*% change of Average pore diameter*
0	506	N/A	3.39	88.70	N/A	27	N/A
1	349	-31.08	1.96	82.00	-41.98	23	-15.74
2	333	-4.61	1.56	78.40	-20.54	19	-17.01
3	331	-0.48	1.51	77.80	-3.07	18	-2.63
4	333	+0.71	1.49	77.60	-1.25	18	-1.56

Table 17 Degradation in surface area and porosity of SCD pSi during repeated capillary condensation.

The sample was then re-wetted in a 20ml solution of 50:50 MeOH: DI water for 5 minutes before air drying on a hotplate at 60°C for 3 hours. The sample was re-processed three more times, using the same soak/dry cycle and gas adsorption analysis was carried out after each cycle (Figure 23).

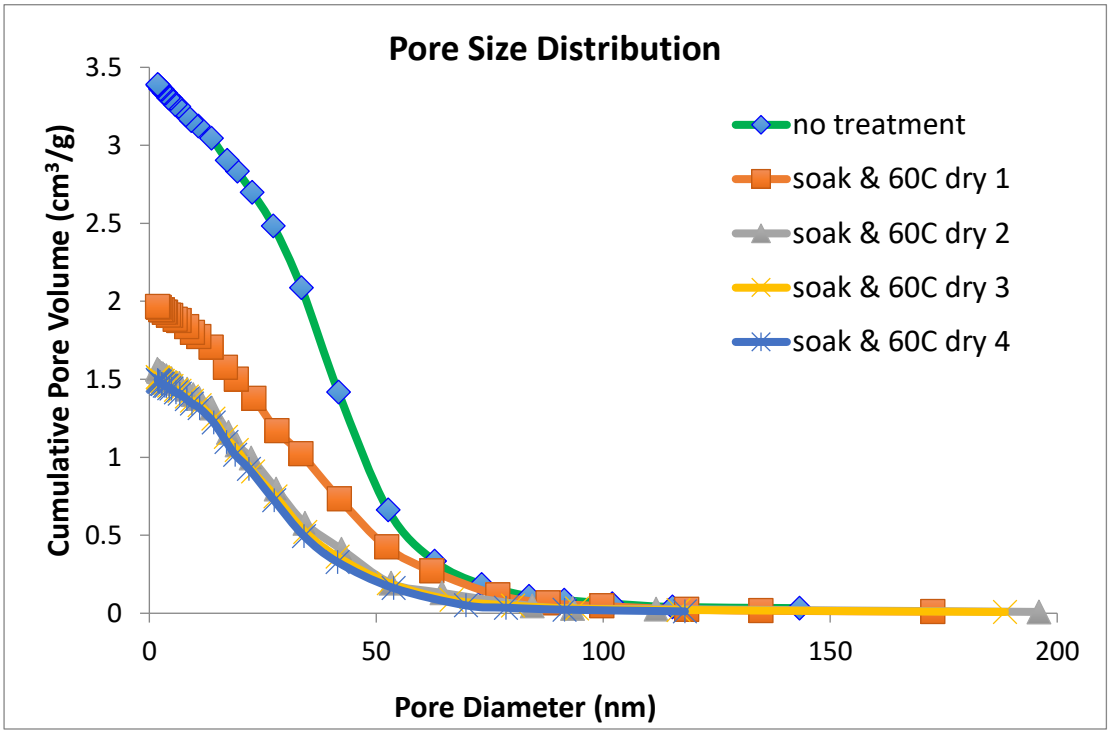

Figure 23 Pore volume/pore size distribution in SCD pSi (Sample UoB 102) during repeated capillary condensation/evaporation (0-4 soak/dry cycles).

The outcomes of this experiment showed that both air drying and storage in ambient air can lower pore volumes, especially if the humidity of the air varies with time, leading to repeated wetting-drying cycles. Substantial porosity degradation can accompany porous silicon fabrication sequences that involve more than one drying step. The majority of damage is caused by the most fragile pore walls collapsing due to the surface tension & capillary forces exerted by the liquid during evaporation in the first two soak/dry cycles (Figure 23). The residual porous infrastructure is more robust, with limited further deterioration taking place in subsequent soak/dry cycles.

Conclusions

This section confirmed that repeated drying steps during manufacturing can significantly lower pore volume and thereby drug payloads.

Lengthy storage in the air can cause significant deterioration of porosity, which is contrary to a gentle sedimentation procedure, which will be covered in the next section.

It was claimed that the following order of fabrication/processing steps: anodisation-sonication-sedimentation-drug loading enables complete avoidance of drying and humid air storage induced structural damage, before drug loading.

2.4. Particle size selection

2.4.1. Size select sedimentation

Abstract

This section demonstrates the ability of sedimentation to size-select ultrasmall (1-10 micron) nanoporous microparticles in common solvents. Experimental values of settling times in ethanol and water are compared to those calculated using Stokes' Law. Differences can arise due to particle agglomeration, internal gas generation and incomplete wetting. Size tunability is quantified for 1 to 120 hours of sedimentation. Air-dried and supercritically-dried pSi powders are shown to have, for example, their median diameter d(0.5) particle sizes reduced from 13 to 1 µm and from 20 to 3 µm, using sedimentation times of 6 and 2 hours respectively. Such filtered microparticles also have much narrower size distributions and are hence suitable for administration in 27 gauge microneedles, which are frequently used in intravitreal drug delivery.

Introduction

Porous silicon particulates for drug delivery can be separated into two size categories: microparticles and nanoparticles. The possible application depends on the particle category choice. There are advantages and disadvantages to both (Kohane 2007). Nanoparticles, with higher comparative surface areas and shorter diffusion distances, yielded to faster dissolution and faster drug release, regularly over a matter of hours (Lee 2015) and as such are well suited to oral delivery applications, where drug delivery is determined on the time frame of its passage through the digestive tract. Such ultrasmall particles also remain mobile, even after parenteral delivery and hence are typically suited to systemic treatments, whilst their ultrasmall size enables them to enter cells by endocytosis and work within (Kohane 2007). Opposite to this, microparticles can offer higher internal drug payloads and slower release rates (Tzur-Balter 2013). Their larger size also renders the particles relatively immobile at the site of delivery. Porous silicon microparticles are thus highly suited to the specific targeting of organs such as the liver or pancreas, where clinical trials for brachytherapy are on-going (Canham 2014, Goh 2007). Alternative opportunity for biodegradable microparticles is retinal conditions (Warther 2018) where slow-release formulations are urgently needed to reduce the frequency of intravitreal injections required, thereby significantly enhancing patient

comfort. In this study, we have focused on achieving very small microparticles, rather than nanoparticles.

Another essential contemplation for particle size tailoring for the loading of specific molecules in a top-down approach, using highly tunable electrochemical anodisation is the fabrication process (Loni 2018). Comminution processes such as ball milling or sonication can then be used to produce particles within a chosen size range (Storey 2020 in press).

For drug delivery via needle administration, size selection of the ensuing microparticles is an important step. A narrow size distribution with minimal outliers will help prevent needles from clogging (Puthli 2009), whilst finer gauge needles improve patient comfort. Needle gauges of 25G or 27G are considered a good compromise of injectability and comfort (Miller 2010, Whitaker 2011). A 27G needle has an internal diameter of only about 200 microns and it is recommended that all particles should be below 20-micron diameter to avoid needle blockage through particle agglomeration (Miller 2010, Whitaker 2011).

Numerous methods can be employed to ensure a tight size distribution. For nanoparticles, sonication followed by centrifugation is a popular method but is often time-consuming and requires additional processing steps (Hon 2012, Roberts 2017). In the other hand, for microparticles, filtering or sieving using metal sieves can enable the selection of particles below 20 μm, however, the process can impart undesirable metal contamination (Loni 2018) since it requires violent agitation of powder, which is also likely to cause damage.

Additionally, using sedimentation, this gentle size selection procedure can be achieved in a suitable time frame with resulting narrow size distributions. If anodisation-sonication-sedimentation-drug loading is sequentially used, then small ultrahigh porosity microparticles ("aerocrystals") can completely avoid drying induced structural damage, before drug loading. Besides, we show here that in contrast repeated drying steps during manufacture can significantly lower pore volume and thereby drug payloads.

Sedimentation was not investigated at all with porous silicon and prior works have not studied it quantitatively yet (Litvinenko 2010). Here, we use Stokes' Law calculations to investigate the likely settling velocities for silicon particles of varying porosity and size in two common solvents: water for hydrophilic particles and ethanol for hydrophobic particles. The porous silicon microparticle range was then experimentally investigated. Prior quantitative

sedimentation studies of some other materials, together with this study, are listed in Table 18. We see that submicron particles, even when non-porous, require very long settling times, whilst quite small microparticles have moderate settling times that are strongly dependent on particle size and density.

Reference	***Type of particle*** ***Density (g/cm^3)***	***Particle size*** ***range (µm)***	***Settling velocity*** ***(cm/h)***	***Settling times utilized***	***Sedimentation solvent***
Vida-Simiti 2012	Solid Nickel 8.90	2-90	5000-72463	5-75 s	Water
Giddings 1991	Porous silica 1.48-1.67 (dry)	2.31-7.48	1270-2571	2.08-4.49 min	Water
This study	*Porous silicon* *1.02-1.67 (immersed)*	1-70	*0.04-5*	*1-24 h*	*Water* *Ethanol*
Philipse 1990	Solid Silica 1.80	0.6-0.72	0.04-0.09 & 6.3	100-200 h	Water Ethanol

Table 18 Particle size range, settling velocity and settling time for different types of particles from prior sedimentation studies and the current study.

Experimental Methods

Porous Silicon Microparticle Preparation

Electrochemical anodization of heavily boron-doped crystalline silicon wafers (0.005-0.02 Ωcm) was used to fabricate porous silicon membranes. Six-inch diameter wafers were anodised in a double cell by applying a current density of 130 mAcm^{-2} for 46 minutes, whilst circulating an electrolyte mix of 1:1 40wt% hydrofluoric acid and ethanol. An increased current density of 165 mAcm^{-2} was applied in the end, for a few seconds, to assist the electropolishing and further detachment of the porous silicon membrane. Lower porosity membranes (UoB 101 49%) were collected and rinsed in ethanol before drying in the air on a hotplate at 60 ^{o}C for 3 hours. Alternatively, for the preservation of high porosity membranes

(UoB99 85%) supercritical drying (SCD) using a Quorum Technologies Limited K850 critical point drier was used (Canham 1994, Loni et al. 2015, Nekovic et al. 2020). Ball milling was then utilized to rapidly create large quantities of microparticles by using a Fritsch planetary ball miller at 300rpm for only 1 minute. Hydrophobic microparticles were created by anodisation, rinsing, drying and milling but could be rendered hydrophilic by subsequent high-temperature oxidation for 16 hours at 700 ^{o}C in diluted oxygen using a ThermoScientific rotary furnace.

Size selection Sedimentation Trials

Six 1 g hydrophilic samples of air-dried, ball-milled and oxidised mesoporous silicon powder of 48.4% porosity were individually mixed with 20 ml of deionized water in separate glass vials and thoroughly vortex mixed. They were subsequently subjected to sedimentation in deionized water at room temperature for different periods from 1 to 24 hours in a 5 cm high liquid column. After the assigned times, the supernatant from each vial was decanted off using the pipette and the solvent removed at 60 ^{o}C in a Genlab drying cabinet until no further weight reduction was observed. The final dry weight was recorded and thereby the overall pSi supernatant yield calculated (dried supernatant weight/ original pSi weight x 100%). A similar 2-hour sedimentation procedure in ethanol was applied to 85% porosity supercritically-dried pSi flakes, that had been ball milled to form a suspension of hydrophobic microparticles. Particle sizing of the supernatants collected after different sedimentation times were performed (see below).

Characterisation

- Gas Adsorption Analysis – Nitrogen gas adsorption analysis using a Micromeritics Tristar 3020, was used to determine the pore properties including; surface area, using the Brunauer-Emmett-Teller method (BET) applied to the adsorption branch of the isotherm; pore volume, using the Barrett-Joyner-Halender (BJH) adsorption method; and pore diameter using the adsorption average.
- Particle Sizing – Samples were systematically vortex mixed before particle sizing. A Malvern Mastersizer 2000, engaging laser diffraction at 466 nm, was then used to perform an analysis of particle size distributions within each sample, whilst distributed in deionised water with the aid of 5wt% Igepal.

Results

Stokes' Law calculations of sedimentation velocities

The settling times for idealized spherical particles in a liquid was calculated using Stokes' Law equation $t = \frac{18\eta s_d}{d^2 g(\rho_p - \rho_f)}$ (Sediq 2017), where: d is the diameter of the particle; ρ_p is the mass density of the particle; ρ_f is the mass density of the fluid; η is the dynamic viscosity of the fluid; g is gravitational acceleration, and s_d is the sedimentation distance. A key assumption made for porous particles was that the solvent supporting the particles completely wetted each particle, removing entrapped air. Particle densities used were thus: 2.33 g/cm^3 for solid silicon; 1.18 g/cm^3 for SCD pSi in water, 1.02 g/cm^3 for SCD pSi in ethanol. 1.67 g/cm^3 for oxidised pSi in water and 1.57 g/cm^3 for oxidised pSi in ethanol. Fluid densities used were: 997 kg/m^3 for water and 789 kg/m^3 for ethanol, respectively. Viscosity parameters (at room temperature) used were: 8.90×10^{-4} Pas for water and 9.83×10^{-4} Pas for ethanol, respectively.

Material	*Particle Diameter (microns)*	*Stokes' Law Settling Time for water & s_d=5 cm*	*Stokes' Law Settling Time for ethanol & s_d=5 cm*
Solid silicon (2.33 g/cm^3)	100	6.1 sec	5.8 sec
	50	24.5 sec	23.4 sec
	10	10.2 mins	9.7 mins
	1	17.1 hrs	16.3 hrs
	0.1	70.8 days	67.8 days
Oxidised porous silicon In water 1.67 g/cm^3 In ethanol 1.57 g/cm^3	100	11.9 sec	11.4 sec
	50	48 sec	42 sec

	10	19.9 mins	19.2 mins
	1	1.4 days	1.3 days
SCD Porous Silicon In water 1.18 g/cm^3 In ethanol 1.02 g/cm^3	100	44.1 sec	39.1 sec
	50	2.9 mins	2.6 mins
	10	1.2 hrs	1.1 hrs
	1	5.1 days	4.5 days

Table 19 Stokes' Law calculations of settling times for solid and porous silicon microparticles in water and ethanol (maximum sedimentation distance s_d=5 cm as shown in Figure 31).

Materials used in drying, storage and sedimentation experiments.

Gas adsorption analysis data of supercritically-dried sample UoB 99 together with air-dried UoB 101 used in drying, storage and sedimentation experiments are shown in Table 20.

Sample code	***Pore volume (ml/g)***	***Porosity from pore volume (%)***	***Surface area (m^2/g)***	***Mean pore size (nm)***
UoB 101 (AD)	0.40	48.40	142	11
UoB 99 (SCD)	2.40	84.90	400	23
UoB 99 (SCD+BM)	1.21	74.90	251	19

Table 20 Pore volume/porosity, surface area and mean pore size values for air-dried (AD) pSi UoB 101 and supercritically-dried pSi UoB 99, before and after ball milling (BM).

Experiment 1. Size distribution versus sedimentation time for oxidised porous silicon microparticles in water.

Figure 24 illustrates the visual appearance of a sample UOB 101 suspensions after sedimentation times varying from 1 to 120 hours. Table 21 and Figure 25 quantify the size distributions and yields of the supernatants collected.

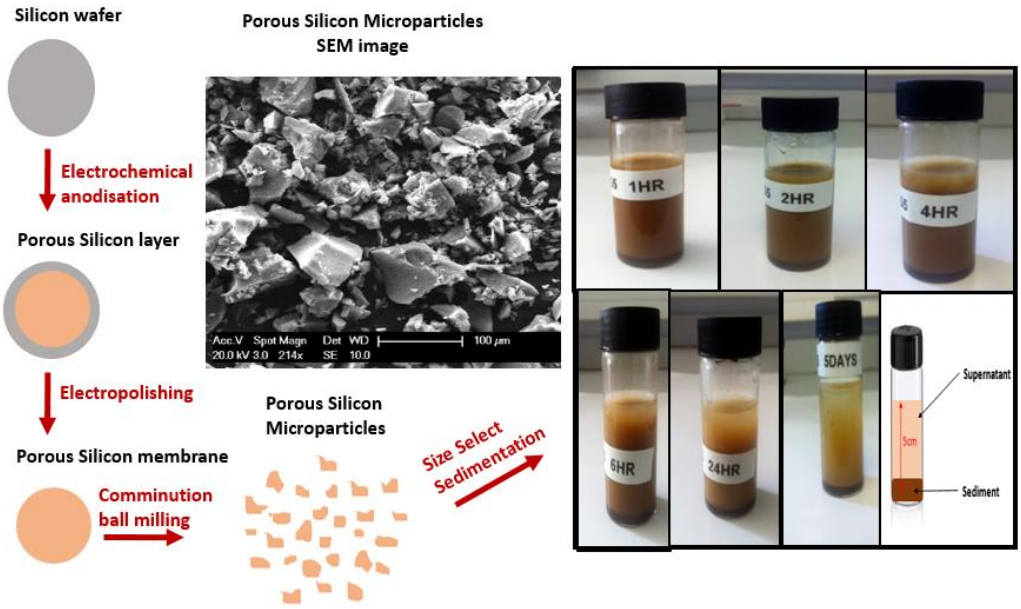

Figure 24 Graphical abstract consisting of the schematic diagram of the experimental procedure and optical image of individual UoB 101 samples during different sedimentation times in water.

Sedimentation time (h)	*Particle size (µm) d (0.1)*	*Particle size (µm) d (0.5)*	*Particle size (µm) d (0.9)*	*The yield of pSi particles (%)*
0 (control sample)	1.616	13.397	34.023	N/A
1	0.668	2.478	9.909	13
2	0.601	1.700	3.459	8
4	0.555	1.298	2.485	5
6	0.545	1.123	2.077	3
24	0.252	0.593	1.326	1
120	0.250	0.440	0.810	1

Table 21 Particle sizing and yield of pSi for air-dried UoB 101 after sedimentation over varying times. *The d value represents particle diameter in microns and the values are shown in the table refer to the cumulative volume of particles below this size as a percentile.*

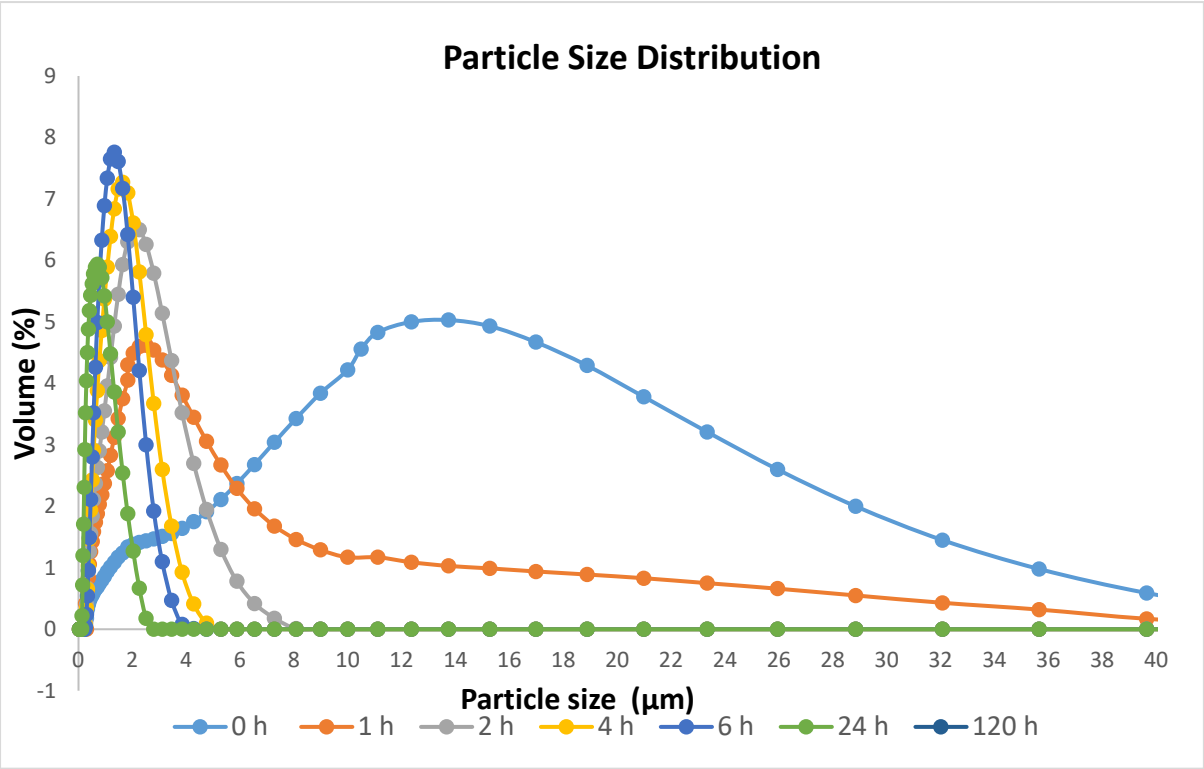

Figure 25 Particle Size Distribution of air-dried UoB 101 for sedimentation times from 0 to 120 h.

Experiment 2. Size distribution change by sedimentation for supercritically-dried porous silicon in ethanol.

Table 22 and Figure 26 present the particle size distributions data after 2-hour sedimentation.

Sample details	*Particle size (µm) d (0.1)*	*Particle size (µm) d (0.5)*	*Particle size (µm) d (0.9)*	*The yield of pSi particles (%)*
SCD + BM	2.00	19.71	68.49	N/A
SCD + BM + 2hour sedimentation	0.79	2.91	8.98	11.38

Table 22 Particle sizing and yield of pSi data for supercritically-dried UoB 99 is presented in the table above.

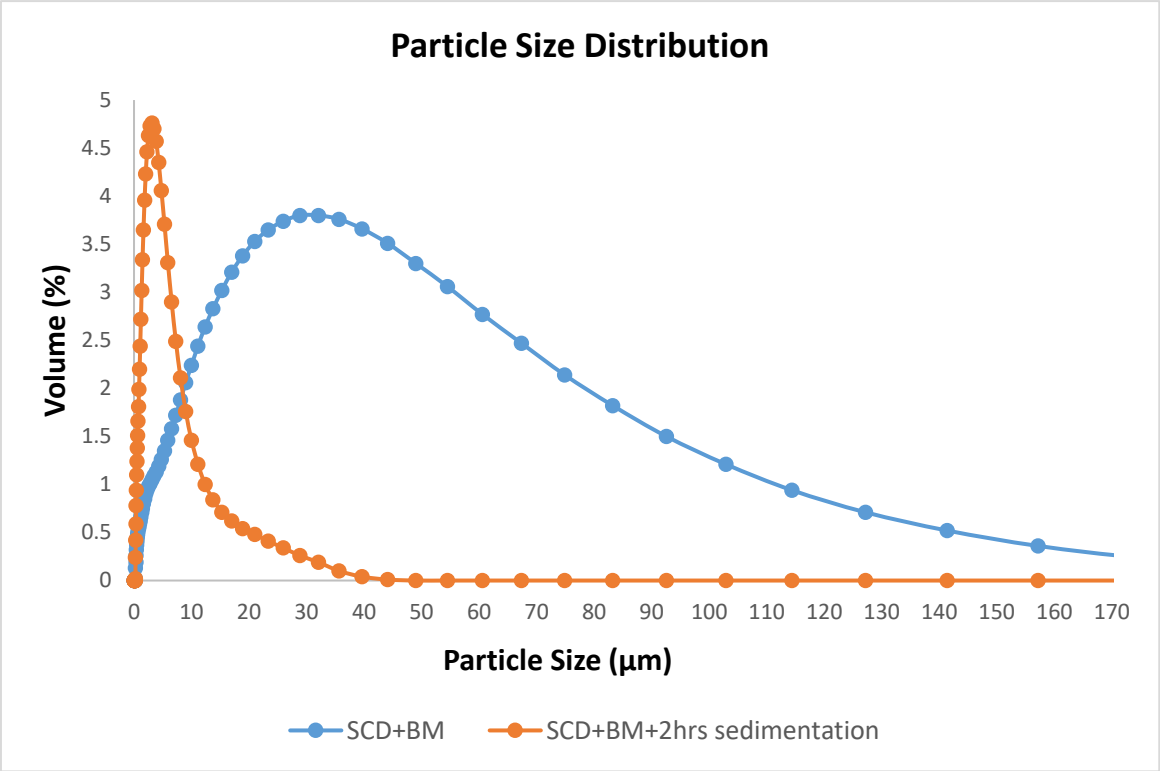

Figure 26 The particle size distribution of SCD material UoB 99 before and after 2 hours sedimentation.

Discussion

Experiment 1 intended to quantify the size tunability of the sedimentation technique for porous silicon particles and common solvents such as water (Figure 25). Particle size distribution data (Figure 26 and Table 21) shows a consistent trend for narrowing spread and smaller particles held in suspension with increasing time. After 1 hour sedimentation, the peak particle size of the oxidised porous silicon (UoB 101) is approximately 2.2 µm, but a significant volume of particles above 10 µm remain in suspension at this stage. By 6 hours a much tighter size distribution is apparent with a peak particle size of 1.5 µm whilst particles above 4 µm have now sedimented out. This is significantly *faster* than Stokes' Law (Table 19) predicts whereby it is calculated that 4 µm particles would take 27 hours to settle. The discrepancy can be attributed to particle agglomeration, as suggested by prior sedimentation studies, summarized in Table 20, attributing it to a tendency of small particles to diminish their higher surface energies. At 24 hours, the trend in experimental data continues with peak particle size and upper particle size in the supernatant being 1 µm & 3 µm respectively. Finally,

after 120 hours sedimentation, the maximum size of particles in suspension is confined to just below 1 µm with a peak size of 0.5 µm. A small fraction of larger particles were still present in the supernatant, denoted by a much smaller second peak, however, this was due to accidental disturbance of the sediment whilst decanting the supernatant.

Experiment 2 explored the use of sedimentation for very low-density silicon aerocrystals. Supercritically-dried high porosity pSi is the most mechanically fragile porous silicon nanostructures and benefits most from gentle processing techniques like sedimentation. Following a 2 hour sedimentation period, the peak size of particles in the supernatant was 3.5 µm, with all particles above 50 µm have settled. Stokes' equation predicts that 50 µm particles in ethanol need only 2.6 mins to settle whilst 10 µm particles need 1.1 hours and 1 µm particles need 4.5 days. It is evident (from Figure 26) that there are still substantial numbers of 10-micron particles that have not sedimented after 2 hours. This is *slower* than predicted by Stokes' Law and might arise from several factors, such as internal hydrogen gas generation due to oxidation, incomplete solvent wetting of the silicon aerocrystal particles or their partial fragmentation due to dissolution in the solvent. Further detailed studies are needed to evaluate which of these is dominant. In summary, settling time depends on the density and viscosity of the solvent, but more significantly on the particle size and particle density, which follows an inverse relationship (Table 22). It is proposed that for sedimentation in the water, the particle agglomeration appears more pronounced than in ethanol. Short sedimentation times of 1-2 hours in both water and ethanol can be used to extract 1-10 micron porous silicon particles with yields above 10%. Settling times and yields in water are affected by particle agglomeration, thus the process might benefit from surface modifications to increase particle surface charge.

It was previously shown that even longer ethanol storage does not cause any further change to the pore volume and surface area of the material (Nekovic et al. 2020). Accordingly, sedimentation is considered as a gentle procedure for narrowing the particle size distribution below a certain value.

2.5. Conclusions

Sedimentation in solvents, unlike metal sieve filtration, is a technique of size selection that can be used without the need to dry porous silicon particles created by wet electrochemical etching.

The ability of sedimentation as a processing tool for size selectivity of microparticles below 10 microns in solvents such as deionized water and ethanol was demonstrated. Prior sedimentation studies on porous silicon have not performed a quantitative analysis. Accordingly, using Stokes' Law we calculated settling times for porous silicon particles of different densities. We found that experimentally particles are settling significantly faster than predicted for higher density (low porosity) oxidised pSi microparticles in water and slightly slower for lower density (high porosity) supercritically-dried pSi microparticles in ethanol.

Using sedimentation, a very tight microparticle size distribution, especially for oxidised pSi material after only 2 hours of processing was ensured. Achieved particle sizes are therefore suitable for fine-gauge needle administration. We have also considered factors that can cause a possible needle blockage via particle agglomeration. For a 27G needle, particle sizes below 20 microns are recommended (Miller 2010, Whitaker 2011) and can be extracted via sedimentation.

It was confirmed here that repeated drying steps during manufacturing can significantly lower pore volume and thereby drug payloads. Contrary to sedimentation, lengthy storage in the air can cause significant degradation of porosity. We claim that the following order of fabrication/processing steps: anodisation-sonication-sedimentation-drug loading enables complete avoidance of drying and humid air storage induced structural damage, before drug loading.

2.6. References

Anderson J, Rosenholm J, Areva S and Lindén M (2004) Influences of material characteristics on ibuprofen drug loading and release profiles from ordered micro- and mesoporous silica matrices, Chemistry of Materials, 16(21), pp. 4160-4167.

Balter AT, Rubinski A, Segal E (2012) Mathematical modelling of drug release from nanostructured porous Si: combining carrier erosion and hindered drug diffusion for predicting release kinetics, Journal of Materials Research, 28(2), pp. 231-239.

Bellet D and Canham LT (1998) Controlled drying: the key to better quality porous semiconductors, Advanced Materials, 10(6), pp. 487-490.

Billat S, Thonissen M, Arens Fischer R, Berger MG, Kruger M, Luth H (1997) Influence of etch stops on the microstructure of porous silicon layers, Thin Solid Films, 297(1–2), pp. 22-25.

Bley RA, Kauzlarich SM, Davis JE, Lee HWH (1996) Characterization of silicon nanoparticles prepared from porous silicon, Chemistry of materials, 8(8), pp. 1881-1888.

Brumhead, L. T. Canham, D. M. Seeking and P. J. Tufton (1993) Gravimetric analysis of pore nucleation and propagation in anodised silicon. Electrochimica acta, 38(2-3), pp. 191-197.

Canham LT, Cullis AG, Pickering C, Dosser OD, Cox TI and Lynch TP (1994) Luminescent anodized silicon aerocrystal networks prepared by supercritical drying, Nature, 368(6467), pp. 133-135.

Canham LT (2007) Nanoscale semiconducting silicon as a nutritional food additive, Nanotechnology, 18(18), p. 185704.

Canham LT (2014) in Porous Silicon for Biomedical Applications, Edited by H.Santos, Woodhead Publishing, pp. 3-20.

Cooper AI (2003) Porous materials and supercritical fluids, Advanced Materials, 15(13), pp. 1049-1059.

Cullis AG and Canham LT (1991) Visible light emission due to quantum size effects in highly porous crystalline silicon, Nature 353(6342), pp. 335-338.

Charnay C, Bégu S, Tourné-Péteilh C, Nicole L, Lerner DA and Devoisselle JM (2004) Inclusion of ibuprofen in mesoporous template silica: drug loading and release property, European Journal of Pharmaceutics and Biopharmaceutics, 57(3), pp. 533-540.

Chiste E, Ischia G, Scarpa M, Daldosso N (2019) Ultrasonication effect on size distribution of functionalized porous silicon microparticles, Materials Research Express, 6(7), p. 075006.

Goh AS, Chung AY, Lo RH, Lau TN, Yu SW, Chng M, Satchithanantham S, Loong SL, Ng DC, Lim BC, Connor S, Chow PK (2007) A novel approach to brachytherapy in hepatocellular carcinoma using a phosphorus 32 brachytherapy delivery device – a first in a man study, International Journal of Radiation Oncology* Biology* Physics, 67 (3), pp. 786-792.

Giddings JC and Moon MH (1991) Measurement of particle density, porosity, and size distributions by sedimentation/steric field-flow fractionation: application to chromatographic supports, Analytical Chemistry, 63(24), pp. 2869-2877.

Hon NK, Shaposhnik Z, Diebold ED, Tamanoi F, Jalali B (2012) Tailoring the biodegradability of porous silicon nanoparticles, Journal of Biomedical Materials Research Part A, 100(12), pp. 3416-3421.

Heinrich JL, Curtis CL, Credo GM, Sailor MJ, Kavanagh KL (1992) Luminescent colloidal silicon suspensions from porous silicon. Science, 255(5040), pp. 66-68.

Hwang J, Woo H, Lee T, Hong J, Kim N, Choi Y, Kwon Y, Jang J, Yoon S, Paik T, Choi J (2020) Engineering of alkyl-terminated silicon nanoparticles for the selective filtration of copper ions, Journal of Industrial Engineering Chemistry, 82, pp. 197–204.

Joo J, Defforge T, Loni A, Kim D, Li ZY, Sailor MJ, Gautier G and Canham LT (2015) Enhanced quantum yield of photoluminescent porous silicon prepared by supercritical drying, Applied Physics Letters, 108(15), p. 153111.

Kennedy E, Canham LT, Santos HA (2016) Mesoporous biomaterials: a lexicon and structured Bibliography of Reviews, Mesoporous Biomaterials, (3), pp. 1-14.

Kohane DS (2007) Microparticles and nanoparticles for drug delivery, Biotechnology and bioengineering, 96(2), pp. 203-209.

Lee JH and Yeo Y (2015) Controlled drug release from pharmaceutical nanocarriers, Chemical engineering science, 125, pp. 75-84.

Litvinenko S, Alekseev S, Lysenko V, Venturello A, Geobaldo F, Gulina L, Kuznetsov G, Tolstoy V, Skryshevsky V, Garrone E, Barbier D (2010) Hydrogen production from nano-porous Si powder formed by stain etching, International Journal of Hydrogen Energy, 35(13), pp. 6773-6778.

Li W, Liu Z, Fontana F, Ding Y, Liu D, Hirvonen JT, Santos HA (2018) Hierarchical structured and programmed vehicles deliver drugs locally to inflamed sites of intestine, Advanced Materials, (30), p. 24.

Loni A, Canham LT, Defforge T and Gautier G (2015) Supercritically-Dried Porous Silicon Powders with Surface Areas Exceeding 1000 m^2/g, ECS Journal of Solid State Science and Technology, 4(8), pp. 289-292.

Loni A (2014) in Handbook of Porous Silicon, ed. by L. Canham, Springer Nature Switzerland AG, pp. 1-9.

Loni A (2018) in Handbook of Porous Silicon, 2nd ed. by L. Canham, Springer Reference Switzerland, pp. 945-950.

Makila E, Ferreira MP, Kivelä H, Niemi SM, Correia A, Shahbazi MA, Kauppila J, Hirvonen J, Santos HA and Salonen J (2014) Confinement effects on drugs in thermally hydrocarbonized porous silicon, Langmuir, (30), pp. 2196-2205.

Maniya NH, Patel SR, Murthy ZVP (2014) Study on surface chemistry and particle size of porous silicon prepared by electrochemical etching, Materials Research Bulletin, (57), pp. 6-12.

Martin-Palma RJ , J. Hernández-Montelongo, V. Torres-Costa, M. Manso-Silván and A. Muñoz-Noval Á (2014) Nanostructured porous silicon-mediated drug delivery, Expert Opinion Drug Delivery, 11(8), pp. 1273-1283.

Miller MA, Engstrom JD, Ludher BS, and Johnston KP (2010) Low viscosity highly concentrated injectable nonaqueous suspensions of lysozyme microparticles. Langmuir, 26(2), pp. 1067-1074.

Nekovic E, Storey CJ, Kaplan A, Theis W and Canham LT (2020) Communication-Supercritically Dried Membranes and Powders of >90% Porosity Silicon with Pore Volumes Exceeding $4cm^3g^{-1}$, ECS Journal of Solid State Science and Technology, (9), p. 024016.

Nissinen T, Lama M, Riikonen J, Lehto VP (2016) Improved production efficiency of mesoporous silicon nanoparticles by pulsed electrochemical etching, Powder Technology, (288), pp. 360-365.

Osminkina LA, Gongalsky MB (2018) in Handbook of Porous Silicon, 2nd edn, ed. By L.T. Canham.

Puthli S and Vavia PR (2009) Stability studies of microparticulate system with piroxicam as model drug, An Official Journal of the American Association of Pharmaceutical Scientists, 10(3), pp. 872-880.

Qin Z, Joo L, Gu L, Sailor MJ (2014) Size control of porous silicon nanoparticles by electrochemical perforation etching, Particle & Particle Systems Characterization, (31), pp. 252-256.

Riikonen J, Mäkilä E, Salonen J and Lehto VP (2009) Determination of the physical state of drug molecules in mesoporous silicon with different surface chemistries, Langmuir 25(11), pp. 6137-6142.

Russo L, Colangelo F, Cioffi R, Rea I, De Stefano L (2011) A mechanochemical approach to porous silicon nanoparticles fabrication, Materials, 4(6), pp. 1023-1033.

Roberts DS, Estrada D, Yagi N, Anglin EJ, Chan NA, Sailor MJ (2017) Preparation of Photoluminescent Porous Silicon Nanoparticles by High-Pressure Microfluidization, Particle & Particle Systems Characterization, (34), p. 1600326.

Salonen J, Laitinen L, Kaukonen AM, Tuura J, Björkqvist M, Vähä-Heikkilä TK, Hirvonen H and Lehto VP (2005) Mesoporous silicon microparticles for oral drug delivery: loading and release of five model drugs, Journal of Controlled Release, (108), pp. 362-374.

Santos HA (2014) Porous Silicon for Biomedical Applications, ed. By H.A. Santos, Woodhead Publishing Series in Biomaterials, 68(68).

Santos SA, Salonen J, Bimbo LM, Lehto VP, L. Peltonen, L., & Hirvonen (2011) Mesoporous materials as controlled drug delivery formulations, Journal of Drug Delivery Science and Technology, 21(2), pp. 139-155.

Sailor MJ (2012) Porous Silicon In Practice: preparation, characterisation and applications, Wiley VCH.

Salonen J, Kaukonen AM, Hirvonen J, Lehto VP (2008) Mesoporous silicon in drug delivery applications, Journal of pharmaceutical sciences, 97(2), pp. 632–653.

Sediq S, Waasdorp KD, Nejadnik MR, Van Beers MMC, Meulenaar J, R. Verrijk and Jiskoot W (2017) Determination of the porosity of PLGA microparticles by tracking their sedimentation velocity using a flow microscope (FlowCAM), Pharmaceutical Research, (34), pp. 1104–1114.

Secret E, Leonard C, Kelly SJ, Uhl A, Cozzan CZ, Andrew JS (2016) Size control of porous silicon-based nanoparticles via pore-wall thinning, Langmuir, (32), pp. 1166-1170.

Simiti IV, Jumate N, Thalmaier G, Sechel N, and Moldovan V (2012) The fabrication and surface functionalization of porous metal frameworks-A review, Journal of Porous Materials, (19), pp. 21-27.

Troia A, Giovannozzi A, Amato G (2009) Preparation of tunable silicon q-dots through ultrasound, Ultrasonics Sonochemistry, (16), pp. 448-451.

Tzur-Balter A, Rubinski A and Segal E (2013) Designing porous silicon-based microparticles as carriers for controlled delivery of mitoxantrone dihydrochloride, Journal of Materials Research, 28(2), pp. 231-239.

Warther D, Xiao Y, Li F, Wang Y, Huffman K, Freeman WR, Sailor, and Cheng L (2018) Porous silicon based intravitreal platform for dual-drug loading and controlled towards synergistic therapy, Drug Delivery, 25(1), pp. 1537-1545.

Whitaker MA, Langston P, Naylon A, Azzopardi BJ and Howdle SM (2011) Particle size and shape effects in medical syringe needles: experiments and simulations for polymer microparticle injection, Journal of Materials Science: Materials in Medicine, (22), pp. 1975-1983.

Yang P, Gai S and Lin S (2012) Functionalized mesoporous silica materials for controlled drug delivery, Chemical Society Reviews, (41), pp. 3679-3698.

Chapter 3. Supercritical fluids and supercritical drying

3.1. Introduction

The main aims of this chapter are to introduce supercritical fluids, their applications (Clifford et al. 2005), the physical processes behind drying induced shrinkage, the nature of porous silicon cracking and to describe the supercritical drying process – which is the most effective drying technique for highly porous nanostructured materials, the focus of this thesis. The theoretical background and underlying physics are explained.

The motivation for supercritical drying

In this subsection, the main advantages and motivations for using supercritical drying are discussed.

Structural collapse during conventional air-drying is a phenomenon related to the surface tension of the rinse solution. As it evaporates, the pressure is exerted on the pore walls which becomes a serious problem the smaller they become. A further consequence is that as-anodized pSi membranes also tend to deform during air drying.

Supercritical drying is a technique that prevents pore collapse and membrane deformation due to solvent evaporation.

The SCD technique was first demonstrated by Kistler in the 1930s and has been of much use for the processing of highly porous nanostructures (Kistler 1930). The experimental procedure Kistler used is as follows: an aerogel stored in alcohol was first transferred to the ether – having both lower critical temperature and chemical reactivity. It was then placed in a small autoclave which was heated inside an electric furnace until a pressure of 300 atmospheres had been reached and the critical temperature achieved. Since then, SCD has been used as a successful technique for fabricating pSi films and free-standing pSi membranes of very high thickness and porosity (< 95 %) (see chapter 2) without causing collapse and hence also results in improved homogeneity.

3.2. Supercritical fluids and their properties

In 1822 Cagniard de la Tour showed that there is a critical temperature, above which a substance exists neither as a gas or a liquid but has properties of both. In their study, liquid carbon dioxide (CO_2) was heated in a sealed chamber and rocked backwards and forwards. The liquid movements were monitored until at some point, the splashing stopped. This has been explained using a phase diagram in Figure 27 (Arai et al. 2002).

The specific feature of a supercritical fluid (SCF) is in the slope of pressure as a function of volume (Arai 2002).

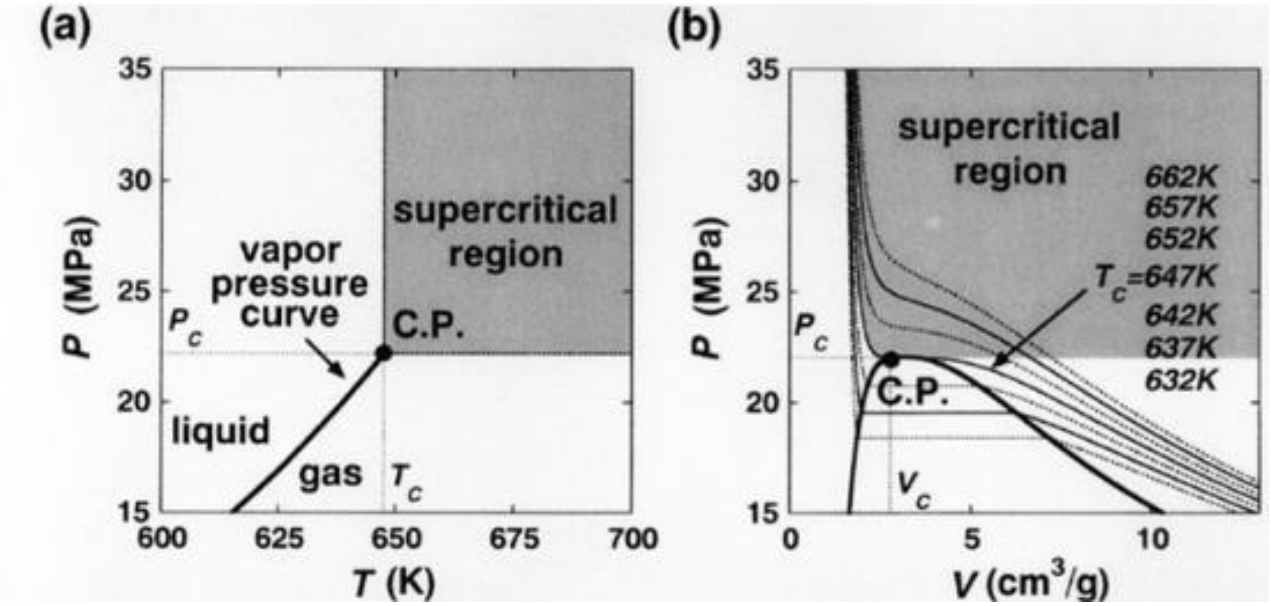

Figure 27 Phase diagram of water in (a) P-T plane and (b) P-V plane. (C.P. is an abbreviation for critical point) (Arai 2002).

Figure 27 (a) shows the phase boundaries and established the supercritical state of the substance. Three states of the matter: solid, liquid and gas are divided by distinct phase boundaries shown by solid lines. A pressure-volume (PV) diagram is shown in Figure 27 (b). The vapour-liquid boundary in the P-T diagram is an area where the vapour and liquid phases coexist in the PV diagram. The cupola-shaped area in Figure 27 (b) presents the liquid saturation at the point of boiling. The right area is the vapours saturated at the condensation temperatures. The graph consists of isotherms and they show how the volume changes with the pressure. At the temperatures below the critical temperature T_c, each of the isotherms consists of three segments. The horizontal section of each isotherm denotes the mixtures of

vapour and liquid. In the areas of the temperatures and pressures above the critical point, the isotherms are smooth and there is no intersection of any phase boundaries. Steep isotherms are observable because of the small changes in the volumes with large pressure changes. A success of SCFs lies in the two responsible factors, which are pressure and temperature (Erkey 2011).

Supercritical fluids show important characteristics: homogeneity, compressibility and a change from liquid to both liquid and gas properties having the properties of both. Carbon dioxide is the most commonly used SCF because it has a low critical temperature value of 30 ˚C, is inexpensive, non-flammable, stable in radioactive applications and is non-toxic. It is also described as a "green" solvent because it avoids the need for more hazardous organic solvents and the search for useful non-toxic solvents is a prime goal of green chemistry. Besides, it is ecologically safe, abundant, renewable, easy to prepare and easy to remove from a product. SCFs are discussed more fully in subsection 3.3 Applications of supercritical drying.

In Table 23, a comparison of gases, supercritical fluids and liquids are given.

	Density (kg/m^3)	***Viscosity (µPas)***	***Diffusivity (mm^2/s)***
Gases	1	10	1-10
Supercritical fluids	100-1000	50-100	0.01-0.1
Liquids	1000	500-1000	0.001

Table 23 Comparison of gases, supercritical fluids and liquids. Adapted from (Zhang 2014).

In Table 23, density, viscosity and diffusivity values are given for gases and supercritical fluids and liquids, respectively. As we can see from the table, in terms of density the gases have the lowest values, where the liquids have the biggest. Viscosity is the highest for the liquids, where supercritical fluids have 10 x smaller values. Diffusivity is tunable for both gases and supercritical fluids, where it is constant for liquids.

3.3. Applications of supercritical fluids

The most popular applications of supercritical fluids involve *supercritical fluid extraction (SFE)* and *supercritical fluid chromatography (SFC)*. The most relevant application for this thesis is the drying of highly porous material.

Supercritical fluid extraction (SFE)

SFE uses a supercritical fluid to remove the soluble substances from insoluble matrices. These fluids penetrate the sample faster than other solvents and they also transport the extracted material away from the sample faster. There is also less residue of solvents left in the product in comparison to other extraction techniques. In Figure 28, a schematic diagram of the SFC setup is provided. The design of an SFE consists of CO2 cylinder, surge tank, extractor, nad, separators, collector and gas-measuring device, thermostatic baths and isocratic pump.

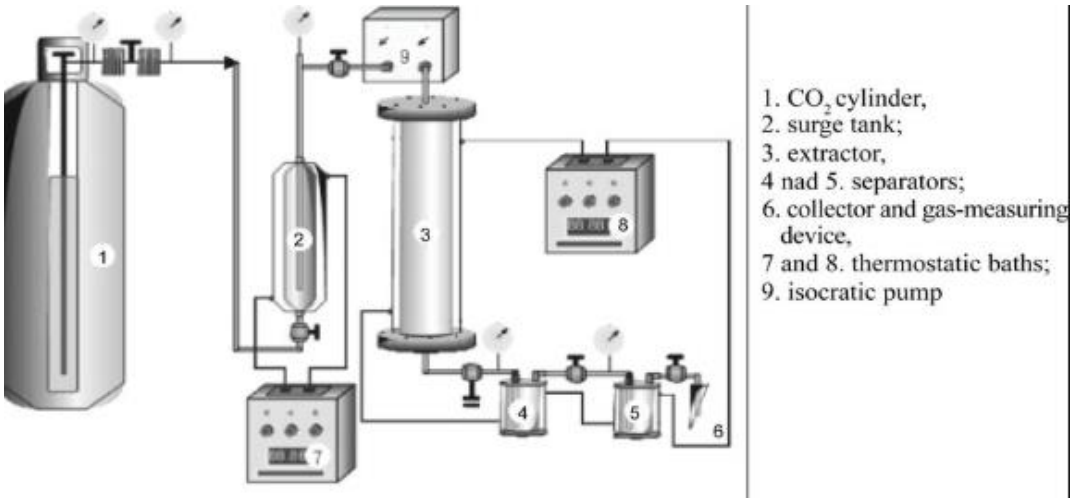

Figure 28 Schematic diagram of SFC setup (Arai 2002).

Liquid CO_2 is delivered in order to keep the cell contents above the critical temperature of the extraction fluid. It keeps the cell above the critical point. Furthermore, an equilibrium coil is used for mixing the carbon dioxide and a modifier (liquid) is used to modify solvent characteristics. The effect of the modifier to the liquid is the on phase diagrams for pressure-temperature relations and the triple and boiling points, and lines of solid, liquid, and vapour separation (Brondz et al. 2017).

The BPR makes sure that the pressure in the cell is above the critical pressure of the extraction fluid. During the extraction, carbon dioxide and a modifier are pumped at set flow rates

through the cell together with the sample. Soluble components of the samples are re-dissolved and then removed from the cell. SFE has been applied to natural products, foods, drugs, metals, polymers, fossil fuels (Abraham et al. 1996).

Supercritical fluid chromatography (SFC)

SFC is defined as the separation of organic compounds using a supercritical fluid as the mobile phase. This technique is an eco-friendly alternative to HPLC (High-performance liquid chromatography). Due to the rapid diffusivity and low viscosity of supercritical fluids, it allows for faster separations and better component resolution in a solution than HPLC.

The equipment used for SFC is similar to SFE equipment; however, a column that contains a stationary phase replaces the sample-holding cell. This system also includes an injection just before the column and a detector between the column and the BPR. The sample in the liquid solvent is dissolved in the mobile phase and passes into the column where its constituents are separated. The isolated components pass into the detector before entering the BPR and on to waste or collection. Here, the depressurized fluid becomes a gas and in the case of using a modifier, it is a liquid. The following compounds have been analysed using SFC: cholesterol, acidic and basic drugs, oligomers (Abraham et al. 1996).

In addition to the techniques mentioned above, supercritical fluids can also be used in metal processing, environmental clean-up methods, impregnation and the dyeing of polymers and synthetic fibres.

An additional very useful application of supercritical fluids is the drying of very highly porous materials. During a standard air-drying process, capillary forces are generated due to meniscus formation in the liquid, which can result in pore walls collapse. The smaller the pore size, the bigger the capillary forces and pressure that are exerted on the delicate pore walls. The Laplace equation (Belmont 1996) is used to estimate capillary forces. Capillary forces act at fluid-air-solid interfaces to minimize the surface energy of the interface. Surface tension is an effect of the misbalance in the forces between molecules and is related to the decrease in surface energy that comes from decreased energy. The surface tension values of water, ethanol and pentane are 72 mJ/m^2, 22 mJ/m^2 and 14 mJ/m^2, respectively. Using the surface tension value of water, for example, it would take a force of 72 dynes to break a surface film

of water 1 cm in length depending on the different surface tension impact of the droplet shape, or bubble formation (Bellet et al. 1998).

There is a variety of possible applications for supercritical drying. Here we will investigate some of the most interesting.

Supercritical CO_2 has been widely used in the food and pharmaceutical industries for extraction processes. The most widely known is the decaffeination of coffee.

Supercritical carbon dioxide decaffeination uses high-pressure vessels (~250-350 atmospheric pressure) to circulate the carbon dioxide through green beans. At these pressures, carbon dioxide has supercritical properties. It can extract up to 98% of the caffeine from beans.

The decaffeination procedure is as follows: first, the green beans are soaked in hot water and are then placed into a sealed extraction vessel. Pores of the coffee beans open up as the beans swell and that allows the caffeine to diffuse out of the beans. At 300 atmospheric pressure, supercritical CO_2 is pumped into the vessel and the caffeine subsequently dissolves into the CO_2 as it is drawn out from the coffee beans. This process takes approximately 8-12 hours, whereby the CO_2 moves through an extractor and scrubber.

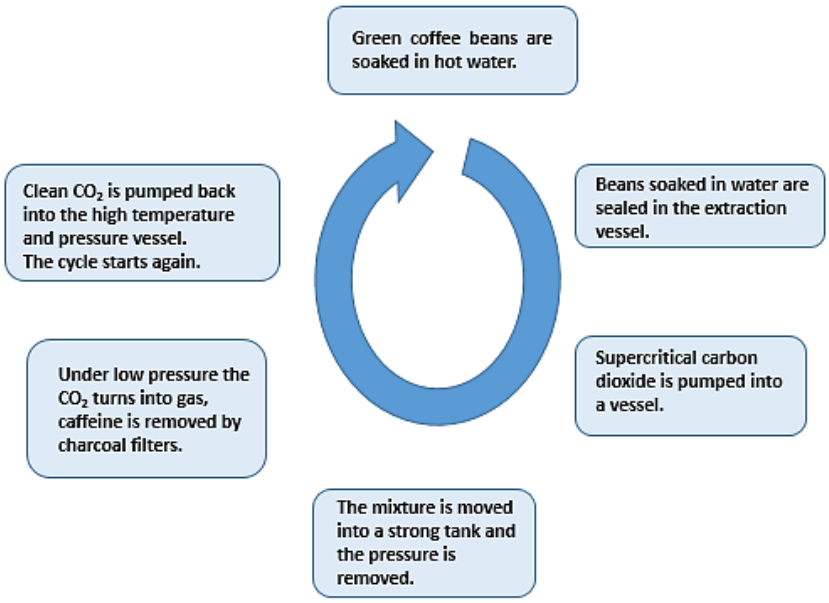

Figure 29 Extraction procedure using supercritical carbon dioxide.

The carbon dioxide and caffeine mixture are placed into a tank. As the pressure is decreased, CO_2 evaporates as it reverts to its gaseous form and leaves the caffeine behind in the container.

Extracted caffeine is used in the pharmaceutical industry and also in energy drinks. The decaffeination procedure is summarized in Figure 29.

Other applications of SCD include the drying and cleaning of organic residues within micro-electro-mechanical systems (MEMS). Here, organic solvents that become trapped in the gaps between devices in an array, are removed (Scherer 1992). Moreover, powder processing is also possible using SCD which prevents particle agglomeration, leading to smaller particle sizes and increased specific surface areas as well as higher homogeneity of a powder.

Another important application is advanced green processing using supercritical CO_2. Supercritical CO_2 is a non-toxic and environmental green solvent that can replace harsher solvents used in traditional processing (Scherer 1992). Supercritical drying has found further application in impregnating porous nanoparticles to provide support. For example, specific metal nanoparticles are impregnated into highly porous materials to provide support (White 2009).

Some further commercial (industrial) uses of SCD include the cosmetics industry, polymer and plastic industry, waste treatment, textile and wood industries.

3.4. Air Drying of porous silicon

Highly porous silicon film becomes strained during evaporation of the rinse solvent, which causes mechanical instability. This results in cracking and peeling of the film. Different studies, such as those using the Laplace equation have been used for studying mechanical stresses in thin films. The pressure difference ΔP between the vapour and liquid is given by:

$$|\Delta P| = \frac{2\gamma_{LV}}{r}; \qquad (4)$$

where γ_{LV} is the surface tension of the fluid and r is the radius of the spherical meniscus (~pore radius when the capillary stresses are maximum) (Bellet et al. 1998).

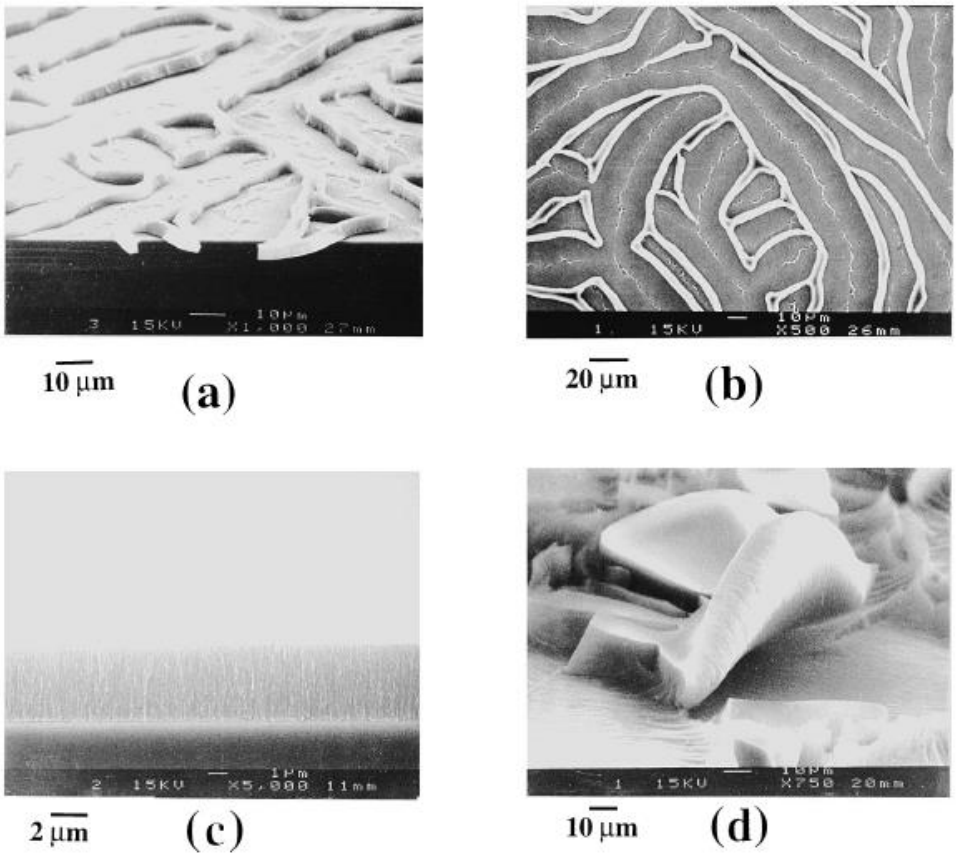

Figure 30 Scanning electron microscopy observation of 5-µm-thick p^+ type porous silicon layers of ~90% porosity after evaporation of different liquids: (a) water, (b) water plus surfactant (TACI), and (c) pentane; (d) exhibits a 20-µm-thick p^+ type PS layer ~porosity of 90% dried with pentane (Belmont 1996).

Cracking of the samples due to the evaporation of water inside the pore network can be investigated and revealed using a scanning electron microscope (SEM) (see chapter 4). The stresses involved cause cracking of the pore network during drying, which results from the capillary tensions in the liquid (Belmont et al. 1996).

Mesoporous silicon is commonly dried in the air but this leads to limitations in achievable surface areas and pore volumes. As-anodized porous silicon films when faced with air-drying exhibit crazing and shrinking. The sponge-like structure of the porous layer undergoes capillary forces that degrade the structure.

Figure 30 shows SEM images of a 90% porosity p+ pSi layer after the evaporation of different liquids. To avoid cracking, the capillary stresses that act during the drying, need to be removed.

Three physical processes are known for removing a liquid from a porous solid. They are evaporation, filtration and distillation. Drying stresses are caused by the presence of a liquid/vapour interface within the structure (Canham 2014).

Later, in the results section, the cracking of the pSi layers and free-standing membranes will be investigated further. One important factor, related to layer deformations is called *critical thickness*. It is defined as a maximum thickness that can be made before the film start cracking. The relevant parameters on which critical thickness h_c depends are the surface tension of the liquid used in drying, the porosity *P*, the pore size *r,* E_{Si} Young's modulus of Silicon and γ_{Si} average of the values for several crystallographic orientations.
The equations used for the calculation of the critical thickness are:

$$E_P = E_{Si}\,(1-P)^2\,; \qquad (5)$$

$$h_c = \left(\frac{r}{\gamma_{LV}}\right)^2 E_{Si}\;\;(1-P)^3\gamma_{Si}\;. \quad (6)$$

E_p and E_{Si} from equation (5) are Young's modulus of the porous and bulk silicon, respectively. Equation (6) provides the value of critical thickness h_c and has a dependence on γ_{LV} and *P*. Results of critical thickness calculations will be presented and explained later in the chapter.

According to equation (6), if deionized water (DI) (used for rinsing the pSi layer) is replaced with a liquid of lower surface tension, the critical thickness will be higher. For example, water can be easily replaced with ethanol or pentane, with pentane having a particularly low surface tension value, as already mentioned. For p^+-type samples with a porosity of 90 %, h_c values are about 1 and 20 µm when water and pentane, respectively, are used as the drying liquid.

Several other techniques can also be used for drying rather than by atmospheric evaporation. These include vacuum drying, slow controlled drying, spray drying and microwave drying. Capillary forces are not avoided in these drying techniques, however freeze-drying and supercritical drying are two methods which can avoid the liquid/vapour interface during drying procedure (Baudron et al. 2019) and supercritical drying is considered the best, particularly for the preparation of very highly porous materials (Canham 1994, Behren 1997).

3.5. Supercritical drying: process

To achieve highly porous nanostructures, supercritical drying has been acclaimed as the most used drying technique.

Carbon dioxide is the most commonly used liquid. Parameters of interest are the critical temperature and critical pressure, which are 31 ˚C (304.1 K) and 7.39 MPa (1,071 psi) respectively (Bellet et al. 1998).

The procedure for supercritical drying is as follows:

- As-anodized pSi samples are rinsed in ethanol after anodization to remove HF-based electrolyte from the pores.
- The pSi sample is then stored in a vial filled with ethanol before supercritical drying.
- The pSi membranes/layers are transferred to the SCD chamber.
- Ethanol is flushed from the system and replaced with liquid CO_2. This process is repeated until all ethanol has been expelled and only liquid CO_2 remains.
- Once all the residual ethanol has been removed the temperature and pressure of CO_2 is increased passed the critical point to create the SCF. This SCF can then be slowly aspirated through an exhaust valve to safely dry the material.

The phase diagram is shown in Figure 31.

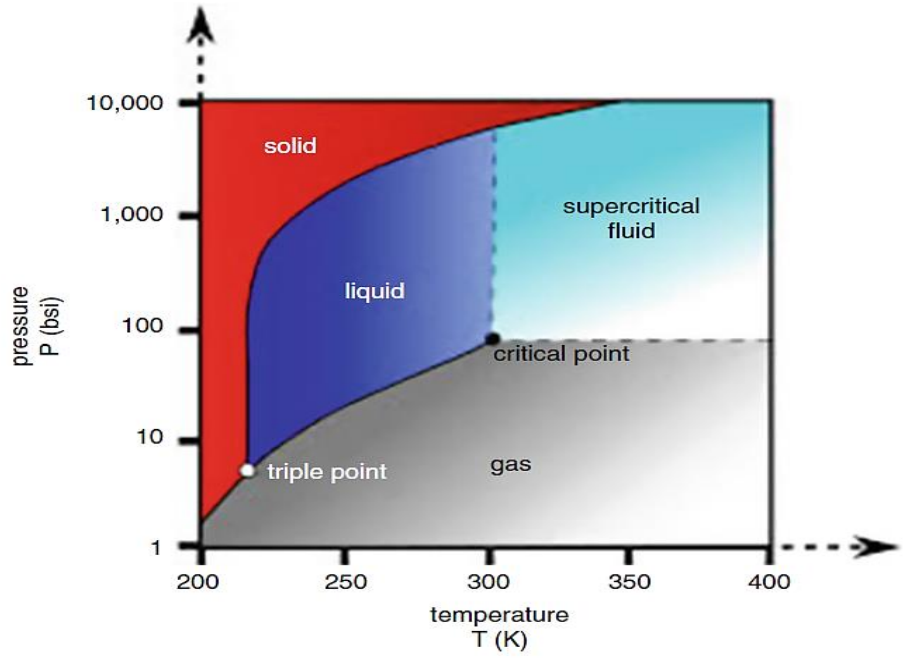

Figure 31 The phase diagram of carbon dioxide; a supercritical solvent (Canham 2014).

In this process, temperature and pressure are increased which raises the liquid above its critical temperature and pressure. At the critical point, the fluid can be removed using decompression with no liquid/vapour phase boundary. No drying stresses are encountered as no boundaries are crossed (Bellet et al. 1998).

The main problem with supercritical drying is having some residual ethanol left in the pores. To test for ethanol, a dedicated sensor can be used. Alternatively, a filter paper placed over the exhaust valve will indicate ethanol if it becomes damp.

To conclude this subsection, one major challenge in the preparation of highly porous structures is to eliminate the liquid solvent from the material without collapsing the structure. Also, supercritical drying is a common procedure of preparation of aerogels (highly porous structures > 90% porosity).

Supercritical drying: equipment

Critical point drying is a method used to avoid the damaging effects of capillary forces upon the pore network during drying. The technique was first introduced for the preparation of SEM specimen by Polaron in 1971. There are different models of critical point driers available commercially.

Critical point driers are available for both powder and wafer processing. In figure 32, some drier types are presented. In this thesis, a Quorum K850 Critical Point Drier is used (Figure 32 a). The popular K850 critical point drier combines versatility and ease of operation. It has a built-in thermo-electric heater and adiabatic cooling that allows precise temperature control. The vertical pressure chamber (32 mm diameter x 47 mm high) has a side viewing port, which allows a clear view of the liquid meniscus during processing.

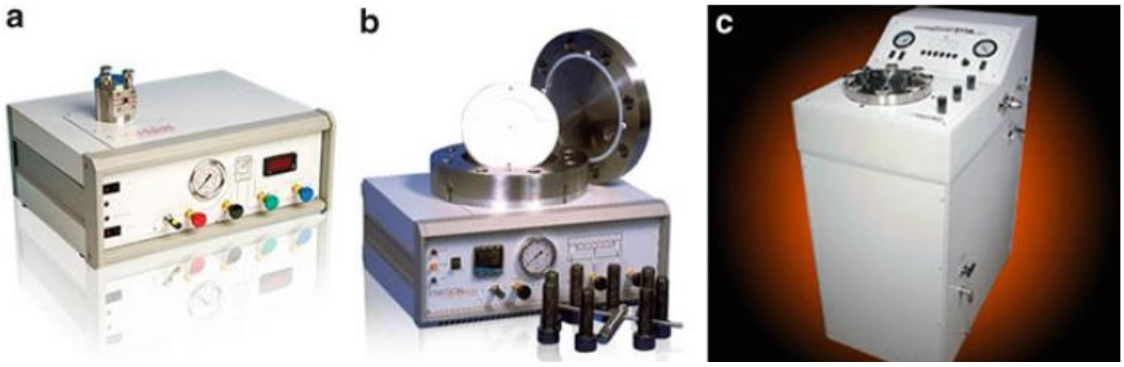

Figure 32 Supercritical dryers, (a) benchtop system (Quorum Technologies Ltd, UK) for processing stain-etched porous Si powders, (b) benchtop system (Quorum Technologies Ltd, UK) for processing an anodized 150 mm diameter silicon wafer, (c) cleanroom-compatible automated multiwafer system (Tousimis Corp., USA) (Canham 2014).

The specimens for Critical Point Drying are placed inside a sample holder and loaded into the pressure chamber of the K850, which has been precooled. The chamber is then filled with liquid CO_2 from a cylinder.

The chamber is then heated to just above the critical temperature and pressure of CO_2. The SCF can then be slowly vented through a needle valve, to avoid specimen distortion.

Another type of critical drier, EMS850, Figure 32 (c) is fitted with thermoelectric heating and adiabatic cooling, and temperature control of +35°C on heating with associated pressure on heating of the order of 1250 psi. This ensures no excess pressures or temperatures.

The chamber is vertical, with top-loading, to ensure specimens do not become uncovered during the drying process and has a side viewing port to locate the meniscus for the correct level when initially filling the chamber. This version of drier is the same as K850 but for a larger industrial scale.

The chamber - with liquid level indicated is shown in Figure 33.

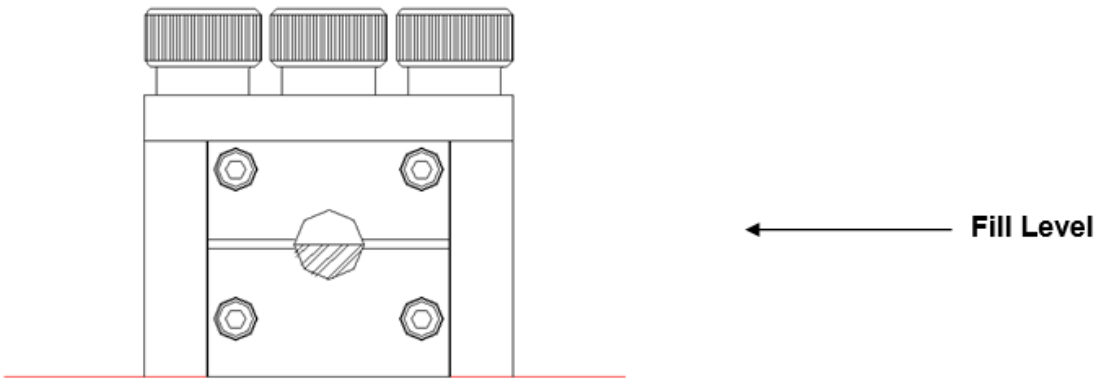

Figure 33 Fill level of a chamber. (From K850 Quorum Technologies Standard Operating Procedure).

The model used in this doctoral thesis is fitted with three valves: fluid inlet, flushing and a gas vent together with fine bleed valve for decreasing the pressure.

3.6. Impregnation using supercritical fluids

Some studies (Abraham et al. 1996, Arai et al. 2002) have shown that drugs can be impregnated (loaded) into mesoporous silicon via supercritical fluids.

A potential application of pSi is drug release, which is possible due to high internal pore volumes. The idea is to achieve a high degree of loading of a model drug, ibuprofen, used in many trials of controlled-release formulations. Ibuprofen is of particular interest due to its low melting point, low cost and good solubility in water. Previous studies have used different solvents for ibuprofen loading, however, liquid CO_2 has several advantages over other solvents, such as it creates no solvent residues, it can be used in high purity applications and requires no additional drying steps.

The proposed procedure for impregnation of ibuprofen into the mesoporous silicon is as follows:

- pSi particles are thoroughly ground using a pestle and mortar.
- pSi particles are then placed in a bag, made of polypropene (PP);
- The particles are weighed and the weight is recorded priory to the placement into a bag;
- The mixture of pSi particles is then placed into a bag;
- The beaker is placed in a stainless steel reactor;
- The reactor is pressurized with carbon dioxide and then the liquid CO_2 is introduced into the glass beaker;
- During this procedure, the solution is stirred at a constant speed using a magnetic bar;
- The loading period can take from 15 mins to 18 hours;
- After the loading has been finalized, the reactor is depressurized;
- The bag, with the mesoporous particles and Ibuprofen, is retrieved (White 2009).

After loading, characterization methods such as Thermogravimetric Analysis (TGA), confocal Raman spectroscopy, Scanning electron microscopy (SEM) and X-Ray Powder Diffraction (XRPD) can be employed. Such studies are planned (see chapter 5).

3.7. Critical thickness study

The main aim of this section is to quantitatively investigate when cracking is likely to occur and hence when SCD is necessary. Large capillary stresses are present during controlled drying and for samples thicker than a critical thickness h_c, cracking occurs.

One of the main problems with the interaction between pSi and liquids is the drying method applied to the material after the fabrication procedure. Capillary condensation is also possible when the pressure is lower than the saturation vapour pressure (Kelvin equations), which is covered earlier in this chapter. Capillary stresses can be very large, creating visible shrinkage of the pSi membranes or layers (Belmont et al. 1996).

In the field of geology, studies have been carried out to induce capillarity during the drying of a clay (Amarasinghe et al. 2014). The effects of particle thickness, particle spacing and the strength of the clay–water van der Waals attraction on capillary phenomena have also been investigated (Belmont et al. 1996).

In a study (Amarasinghe et al. 2014), classical Young-Laplace equations were used. The parameter of interest was the air-water surface tension and by using molecular dynamics the capillary forces that develop in a clay-water-air system were examined. The aim was to understand capillary forces, contact angles and curvatures. The findings were that the calculated results were not consistent with the molecular dynamics (MD) studies, because of the variations in the simulation times. More importantly, this reference gained some fundamental understanding of the clay-water-air capillary phenomena (Amarasinghe et al. 2014).

For this thesis, the procedure for sample preparation in this doctoral thesis is as follows: first, pSi samples are made by anodization of the Si wafers. They are then rinsed in ethanol and left to air dry on a hotplate for a few hours.

SEM imaging can be performed on air-dried samples to study the effect of drying from different solvents, on the pore walls. Depending on the surface tension value of each solvent, drying has different effects on the pSi membranes/layers.

$$h_c = \left(\frac{r}{\gamma_{LV}}\right)^2 E_{Si}\ (1-P)^3 \gamma_{Si}\ . \quad (6)$$

As can be seen from the formula above, the higher the value of surface tension, the lower the critical thickness and vice versa. Calculations of critical thickness for mesoporous silicon as a function of porosity for different solvents; such as water, ethanol and pentane have been calculated.

This model of critical thickness was performed in MATLAB and the results are shown below (Figure 34 and Table 24):

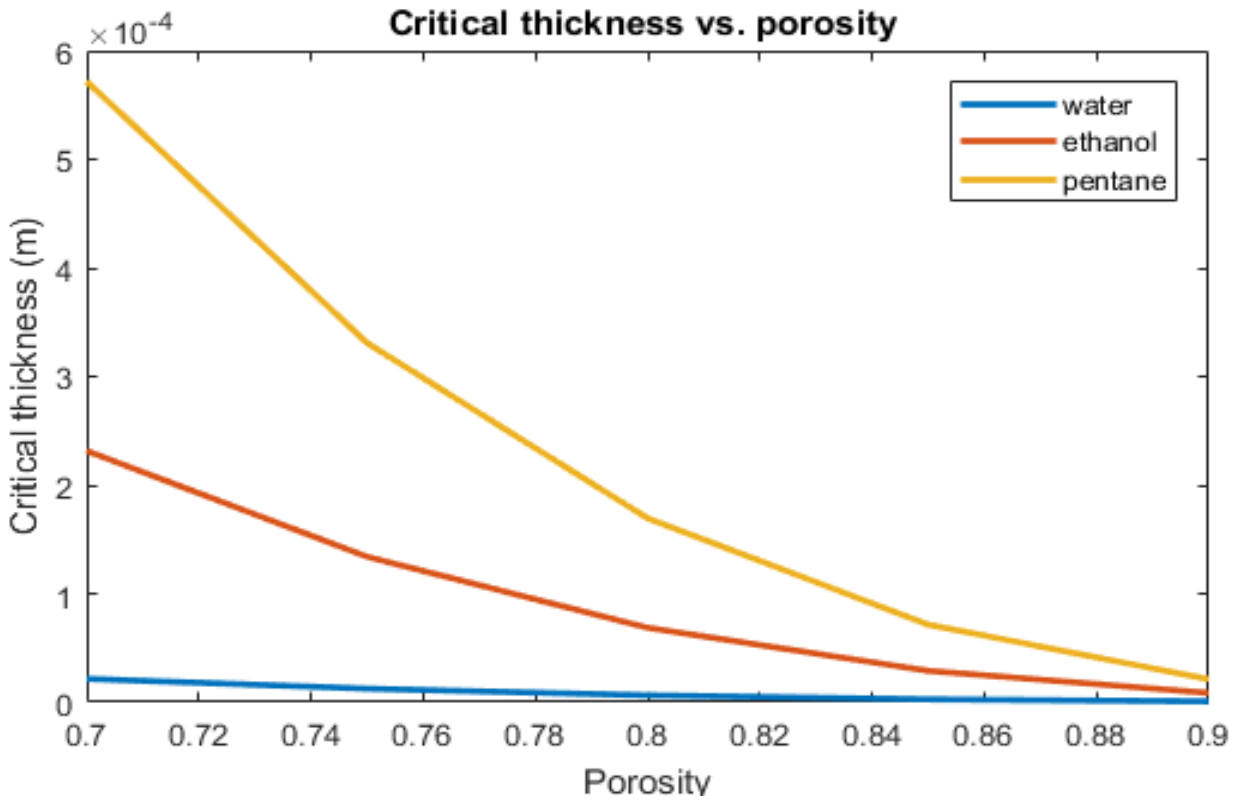

Figure 34 Critical thickness as a function of porosity for water, ethanol and pentane.

γ_{LV} (mJ/m^2)	h_c (µm)	69%	73 %	75 %	79 %	84 %	86 %	90 %
72	water	24	15	12	74	3.2	2.1	0.8
22	**ethanol**	255	168	**133**	79	35	2.35	8.5
14	pentane	630	410	330	196	86	58	21

Table 24 Calculated data of critical thickness for water, ethanol and pentane.

For an ultrahigh high porosity of 90%, for example, layers of air-dried from water need to be thinner than 0.8 microns to avoid cracking. With ethanol evaporation, this limit is increased to 8.5 microns and with pentane drying, a 20-micron thick layer is predicted to be crack-free. However, the thicker layers needed for robust membranes (eg 100-250 microns) will clearly need supercritical drying.

The critical thickness model can tell us when we can expect cracking but now how layers crack. Cracking occurs where large stresses exist within the layers. This model yields different results when different solvents are used. SEM images of cracks are included earlier in this chapter.

3.8. Conclusions

In conclusion, shrinking often happens when drying with water and how this can be reduced by using pentane for relatively thin layers of moderate porosity. However, for thick ultrahigh porosity layers (see chapter 2) SCD is essential to preserve porosity (See figure 34 and Table 24).

The critical thickness of porous silicon can be calculated and depends on the following parameters: mechanical properties, the surface tension of the liquid, porosity and pore size. Layer thickness and also the drying liquid used has been examined, and have been demonstrated to be directly related to surface tension. Overall, SCD is a technique, which avoids the problems associated with the liquid to gas phase changes that are present in other methods.

3.9. References

Abraham MA and Sunol AK (1996) Supercritical fluids, Extraction and Pollution Prevention, In ACS Symposium Series 670, American Chemical Society.

Arai Y, Sako T, Takebayashi Y (2002) Supercritical fluids: molecular interactions, physical properties, and new applications, Springer science & business media.

Baudron V, Gurikov P, Smirnova I and Whitehouse S (2019) Porous Starch Materials via Supercritical and Freeze-Drying, Gels, 5(1), p. 12.

Bellet D and Canham LT (1998) Controlled Drying: The Key to Better Quality Porous Semiconductors, Advanced Materials, 10(6), pp. 487-490.

Von Behren J, Fauchet PM (1997) The strong visible luminescence in porous silicon: Quantum confinement, not oxide-related defects, Physica status solidi (B): Basic research, 204(1), pp. R7-R8.

Belmont O, Bellet D, and Bréchet Y (1996) Study of the cracking of highly porous p+ type silicon during drying, Journal of Applied Physics, 79(10), pp. 7586-7591.

Brondz I, Sedunov B and Sivaraman N (2017) Influence of modifiers on supercritical fluid chromatography (SFC) and supercritical fluid extraction (SFE), International Journal of Analytical Mass Spectrometry and Chromatography, 5(2), pp. 17-39.

Canham LT, Cullis AG, Pickering C, Dosser OD, Cox TI, Lynch TP (1994) Luminescent anodized silicon aerocrystal networks prepared by supercritical drying, Nature, 368(6467), pp. 133-135.

Canham LT (2014) Handbook of Porous Silicon. Zug, Springer International Publishing.

Clifford AA and Williams JH (2005) Introduction to Supercritical Fluids and Their Applications, In Supercritical fluid methods and Protocols, Humana Press, pp. 1-16.

Erkey C (2011) Supercritical fluids and organometallic compounds: from recovery of trace metals to synthesis of nanostructured materials, Elsevier, pp. 11-19.

Kistler SS (1931) Coherent expanded aerogels and jellies, Nature, 127(3211), p. 741.

Amarasinghe A, Priyanthi M, Anandarajah P (2014) Dynamic study of capillary forces on clay particles, Applied Clay Science, (88), pp. 170–177.

Scherer WR (1992) Recent progress in drying of gels Journal of Non Crystalline Solids, (147), pp. 363-374.

White RJ, Luque R, Budarin VL, Clark JH and Macquarrie DJ (2009) Supported metal nanoparticles on porous materials, Methods and applications, Chemical Society Reviews, 38(2), pp. 481-494.

Zhang X, Heinonen S and Levanen E (2014) Applications of supercritical carbon dioxide in materials processing and synthesis, Royal Society of Chemistry, 4(105), pp. 61137-61152.

Chapter 4. Characterization of porous silicon (pSi) with results and discussion

4.1. Gas adsorption analysis

Introduction

Gas adsorption analysis has been previously introduced in Chapter 1 including the theoretical background and relevant data in Chapter 2. Surface area, pore-volume, and pore diameter measurements of pSi nanostructures are based on an adsorption isotherm constructed using data from nitrogen or carbon dioxide gas interactions with the porous material at extremely low temperatures (Sailor 2011). A commercial instrument employed for these measurements and used in this doctoral thesis is the Micromeritics Tristar Analyser 3020. In this section, more details about this precise characterization tool, relating to its principle of work, analysis principles, and also sample preparation are provided.

Furthermore, data analysis was performed on the pSi membranes which have been fabricated by the electrochemical etching of p+ wafers and then subjected to either air-drying or supercritical-drying.

Experimental methods

The Tristar Analyser is an instrument capable of providing high-quality porosimetry measurements on porous materials by employing a gas adsorption method (Sailor 2011).

The Micromeritics 3020 Tristar Analyser consists of the following main components: sample chamber, elevator and dewar with liquid nitrogen. The main interest is the sample chamber and we will mainly focus on this part.

The sample chamber layout is presented in Figure 35 denoting the most relevant parts.

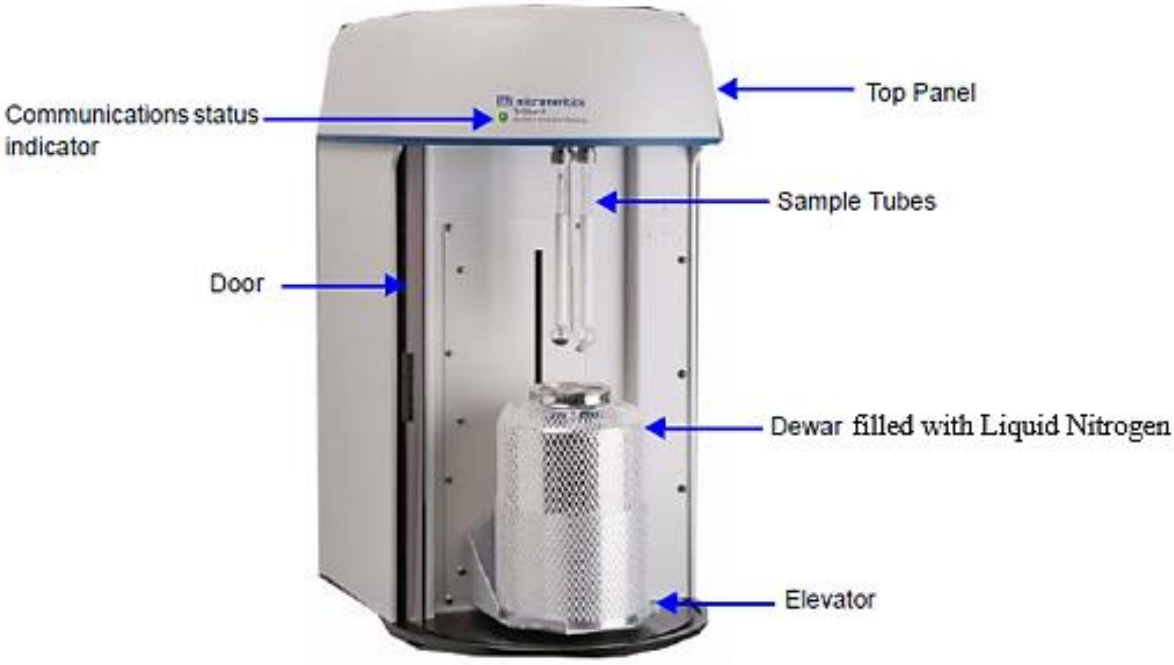

Figure 35 Sample chamber of Micromeritics 3020 Tristar analyser.

Sample preparation and analysis

Described below are the sample preparation steps including the principal steps for loading and operation of the Micromeritics 3020.

- The porous material is placed in a glass sample tube (100 mg or more);
- Degassing (degasification) at 90 °C for 60 minutes is done before gas adsorption analysis to remove existing adsorbed gases and moisture from the tube; Nitrogen is fed into the tube during degassing to avoid the reintroduction of humidity which would otherwise occur in ambient air.
- The weight of the sample before and after degassing is recorded;
- The sample tube is then placed again into the instrument;
- The sample tube is evacuated;
- The free space is measured by helium dosage; Helium is used because it is not readily adsorbed.

- The helium is then evacuated and the tube is immersed in a cryogenic fluid because the gases can easily condense and adsorb onto the surface of our samples at cryogenic temperatures and the steady temperature is also kept trough the analysis.
- The adsorbate gas is dosed in incremental volumes with the pressure being measured in situ after each dose;
- Dosing continues until a plateau is reached by the isotherm and pressure, which implies that pores are filled;
- The pressure is then incrementally reduced and the liquid starts to desorb;
- The porous structure is empty again.

Principles of Analytical Technique

Physical adsorption and capillary condensation principles are used to obtain information about the surface area and porosity of a solid material. A sample placed in an evacuated sample tube is primarily cooled, then exposed to the analysis gas at a series of precisely controlled pressures. With each incremental increase in pressure, the amount of adsorbed gas molecules on the surface increases (Sailor 2011).

An equilibrated pressure P is compared to the saturation pressure P_0 and their relative pressure ratio P/P_0 is recorded along with the quantity of gas adsorbed by the sample at each equilibrated pressure.

Firstly, micropore walls get filled with a monolayer. Nitrogen gas is adsorbed on every surface. Monolayer coverage occurs on all surfaces. Then macropores get filled with nitrogen. The larger pores are filled by capillary condensation. This process may continue to the point of bulk condensation of the analysis gas as well as the relative pressure saturation.

Once the adsorption phase of the analysis is completed, the desorption process may begin in which pressure is systematically reduced resulting in the liberation of the adsorbed molecules. As with the adsorption process, the changing quantity of gas on a solid surface at each decreasing equilibrium pressure is quantified. These two sets of data describe the adsorption and desorption isotherms. Analysis of the shape of the isotherms yields information about the surface area and internal pore characteristics of the material.

Results and Discussion

The calibration gas adsorption measurements are performed on the silica-alumina standards of known morphologies. The accuracy limits for surface area, pore-volume, and pore diameter are in the following ranges: ±6 m^2/g, ±0.08 cm^3/g, and ±1.5 nm, respectively. The principles of analysis are further explained below utilizing an air-dried and supercritically-dried porous silicon membrane (Figure 36).

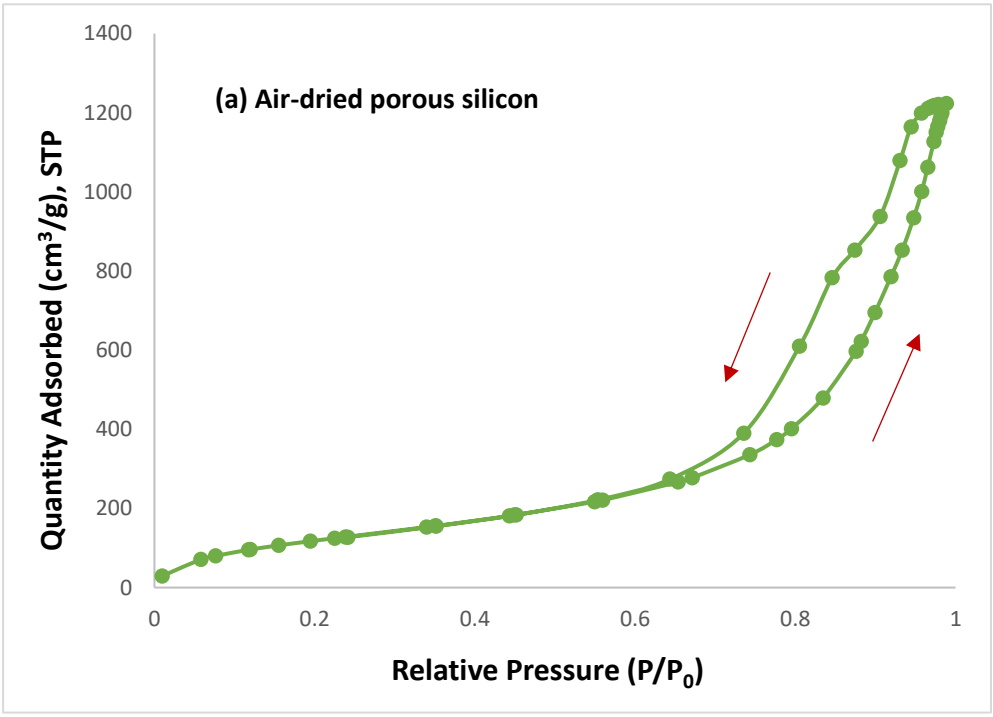

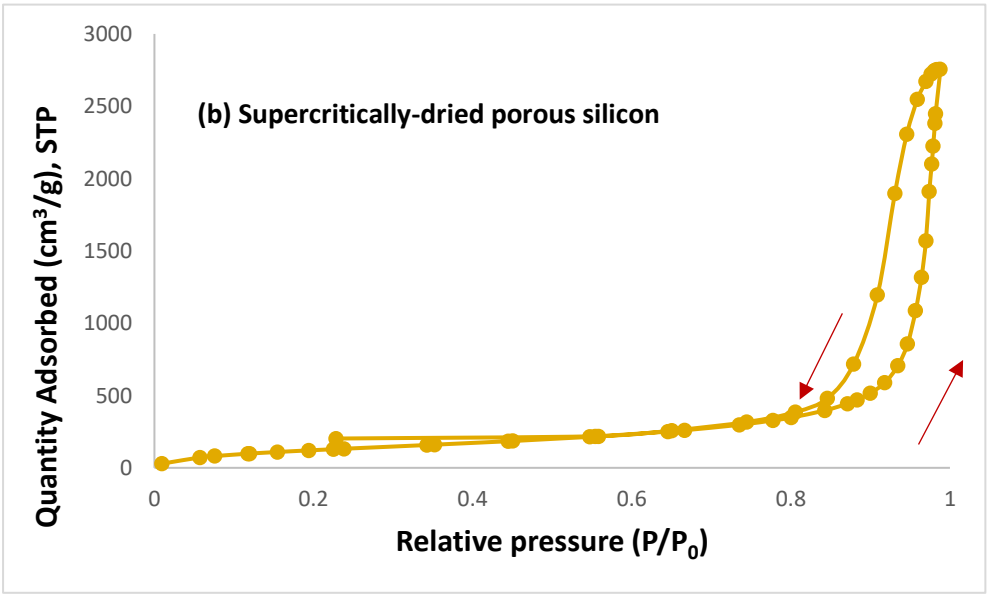

Figure 36 Nitrogen adsorption isotherms for p+ porous silicon membranes. (a) Air-dried pSi and (b) supercritically-dried pSi.

Figure 36 illustrates two typical adsorption/desorption isotherms for highly doped p+ porous silicon samples. The X-axis shows the pressure *P* of the adsorbate gas with units relative to the saturation vapour pressure of the gas, P_0. The volume of gas adsorbed by the sample is shown along the y-axis. By increasing the relative pressure (P/P_0) to the saturation point, the adsorption branch of the curve is obtained. On the other side, by reducing P/P_0 back to zero, the desorption curve is obtained. This path is indicated by the arrows in Figure 36.

The morphology of the samples used in this example analysis belongs to the mesoporous range. To aid the understanding of an isotherm, the adsorption/desorption branches can be further divided into segments. The primary segment of the curve alongside P/P_0 between values 0 and 0.1 corresponds to the adsorption of a monolayer on the porous surface. This is an origin of the surface area value of the pSi structure. A lower total volume of gas adsorbed by the sample (a) indicates a lower total pore volume, relative to the supercritically-dried sample.

The strong increase in adsorbed volume in the latter segment of the curve, which is at $P/P_0>0.7$ for these samples is an indication of capillary condensation in the pores. Eventually, a plateau is observed at P/P_0>0.9 and it relates to complete filling of the mesopores. The amount of the adsorbed volume is proportional to the mesopores capacity. Please, note that the final volume of the gas adsorbed in the region of the plateau is lower for the air-dried porous silicon membrane than the supercritically-dried equivalent (Figure 36). This indicates that the pore volume of the pores is smaller for the air-dried sample (Sailor 2011).

The hysteresis loop originates from microcapillary condensation. It occurs in the smallest pores of the sample. First, molecules adsorb on a surface. Adsorption happens layer by later where the higher energy sites are filled first and then the lower states. Capillary condensation is a process where the molecules accumulated on two opposing walls get close enough to each other they collapse into a thermodynamically lower energy state. By reducing the pressure during desorption the molecules at low energy do not tend to leave their place. For this, the higher gradient of chemical potential (or equivalently pressure drop) is needed to pull the adsorbed molecules out of their sites. It is then visible that the same molecules desorb at lower pressure. This gap is known as a between equilibrium adsorption and desorption pressures are the hysteresis (Dian et al. 2004).

The relationship between the pore radius and relative vapour pressure is provided by the Kelvin equation (7): (Sailor 2011)

$$r = -\frac{\gamma V}{RTln(P/P_0)} \qquad (7)$$

where *r* is the meniscus radius of the liquid, *γ* is the surface tension of the gas/liquid interface, *V* is the volume of the liquid, *T* is the temperature, *R* is the gas constant, *P* is the observed pressure and P_0 is the saturated pressure. This model takes into consideration complete pore wetting by the liquid (Sailor 2011).

Tabulated gas adsorption data for the samples AD and SCD UoB 40 are presented in Table 25.

Sample details	***Pore volume (ml/g)***	***Porosity from pore volume (%)***	***Surface area (m^2/g)***	***Mean Pore size (nm)***
AD	1.88	81.4	478	12
SCD	4.24	90.8	497	29

Table 25 Gas adsorption and gravimetric data of sample code UoB 40 supercritically dried (SCD) membranes and their air-dried (AD) equivalents. The thickness of the sample is 200 µm. Uncertainty on Mean pore size is ±1.5 nm (5%).

The pore volume value of the air-dried sample is lower than for the supercritically-dried one due to the pore collapse during the air drying. Supercritical drying removes the capillary forces and preserves the pore volume. Furthermore, the corresponding porosity values are calculated from pore volume values using the Barrett-Joyner-Halenda (BJH) adsorption method (Barret et al. 1951). Pore volume values obtained from gas adsorption were converted to porosities (Canham 2014).

Mean pore sizes are also presented and we can see they are in the range between 12 nm and 29 nm for AD and SCD samples respectively. They are different as the pore walls collapse during the air-drying which is causing pore size shrinkage. These values fit into the mesoporous silicon range (2-50 nm). Pore volume values are further presented in the plots in Figure 37.

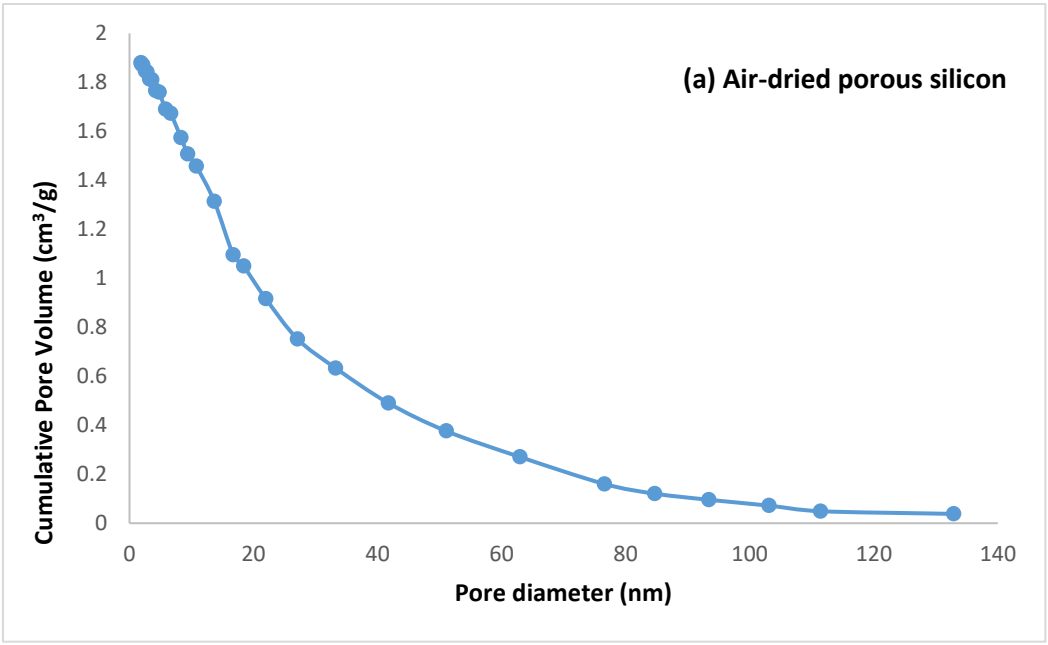

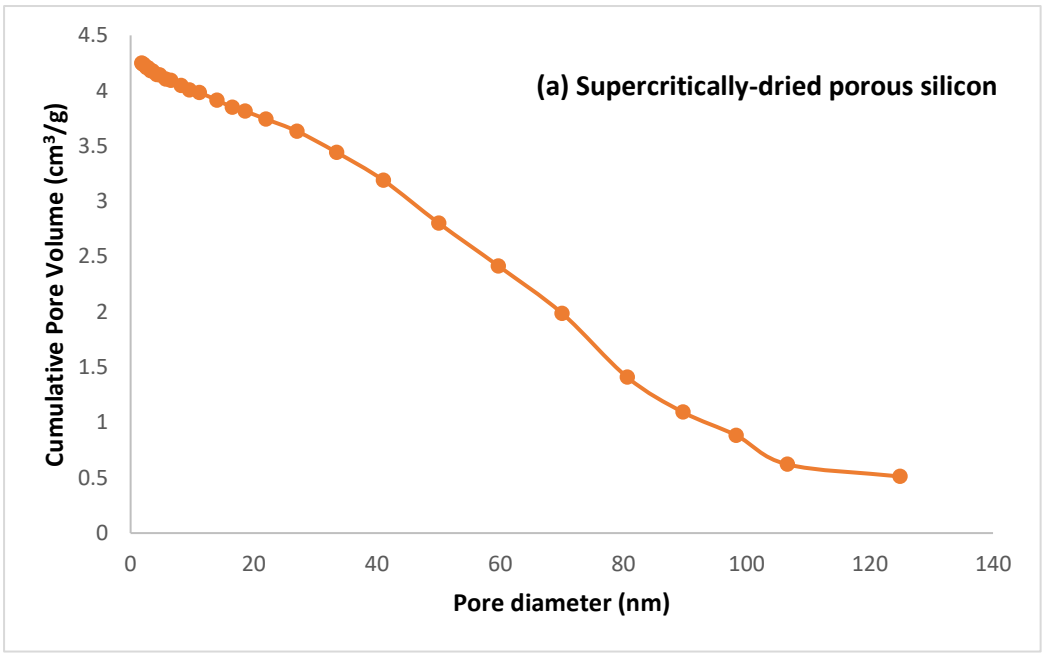

Figure 37 Pore volume vs. pore diameter for p+ porous silicon membranes. (a) Air-dried pSi and (b) supercritically-dried pSi.

Plots in Figure 37 presents pore volume as a function of pore diameter. As we can see, figure (a) denotes the air-dried pSi membrane, where the pore volume is from 0.2 ml/g to 1.8 ml/g which corresponds to the pore diameter range of 1 nm to 130 nm.

For supercritically-dried pSi membrane, the pore volume range is between 0.5 ml/g to 4.3 ml/g. This is related to the pore diameters from 1 nm to 125 nm.

Conclusions

Limitations of Gas Adsorption analysis

Gas adsorption-desorption analysis is a non-destructive technique particularly suited to gather data from small pore structures: above 1 nm and below 100 nm (Canham 2014). This characterization technique is also problematic for low surface area materials.

In the BET measurements, micropores are successfully analysed whereas it is not sensitive to macropores. In the case of larger mesopore structures, electron microscopy is more appropriate to be used for the reliable determination of average pore size. The BET method is capable of providing the best values of surface areas for porous samples.

4.2. Electron microscopy

Introduction

Two types of microscopy are available for this study were: optical microscopy (OM) and electron microscopy (EM). The former one was used in the last two centuries but it has limited capabilities with regards to image resolution. OM and EM are different in terms of (a) principle of work, (b) lenses, (c) magnification, (d) type of images produced, (e) type of imaging performed.

The first electron microscope was constructed by Ruska and Knoll in 1933. This type of microscope was based on the electron pass through thin specimens (McMullan 1995). Then, in 1938, Von Ardenne added the scanning coil to a transmission electron microscope (TEM) and constructed a scanning transmission electron microscope (STEM). Scanning electron microscope (SEM) analysis is used in a variety of disciplines, such as for organic and inorganic materials on the nanometer and micrometre scale. SEM can be accompanied by an energy-dispersive spectrometer (EDS) and it has been very successful (Wang et al. 2005). The majority of SEM machines are equipped with an EDS system and a data analyser system. The advantage of using EDS besides is the evaluation of the various elements compositions.

This section focuses on Scanning Electron Microscopy (SEM), which uses a focused high-energy electron beam to generate signals at the surface of the sample. The signals extracted from the sample-electron interactions can reveal information about the sample, such as morphology, chemical composition, orientation, and a crystalline structure (Nixon 1998). Using SEM the following matters can be studied: topography and morphology (texture), chemistry (chemical composition), crystallography, the orientation of materials (Newbury 1995).

Experimental methods

Before explaining SEM more into detail, a comparison of light vs. electron microscope will be given to familiarise the reader with the topic. The details considered are the illumination source, type of lens, magnification method, type of sample viewing, and use of vacuum. They are shown in Table 26.

Details	***Light /Optical microscope***	***Electron microscope***
The source of illumination	Ambient light.	Electrons.
Type of lens	Glass lenses.	Electromagnetic lenses.
Method of Magnification	Moving the lenses.	Changing the current through lenses.
Type of sample viewing	Ocular (eyepiece).	Fluorescent screen / digital camera.
Use of vacuum	No vacuum.	Vacuum usage.

Table 26 Details about Optical microscope vs. electron microscope. Adapted from the (Website 6).

Light vs. electron microscope elements is shown in Figure 38.

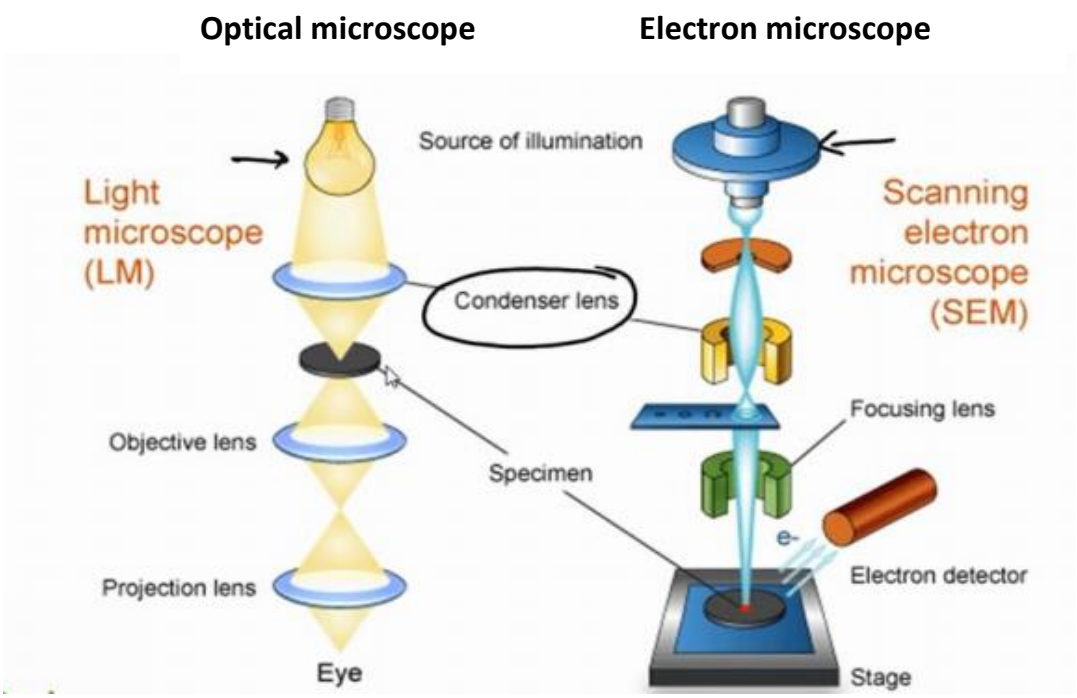

Figure 38 Optical microscope vs. electron microscope (Goldstein et al. 2003).

Furthermore, details of the differences between a Scanning electron microscope (SEM) and Transmission electron microscope are shown in Table 27.

Details	***TEM***	***SEM***
Electron beam	Static beams.	The sample is scanned line by line.
Voltage	High accelerating voltage.	Lower accelerating voltage.
Interaction of the beam electrons	A thin specimen is required.	Wide range of allowed specimens.
Imaging	Electrons pass through and are transmitted by the specimen.	Information is collected near the specimen surface.
Image rendering	Transmitted electrons are focused by the objective lens and magnified to create a real image.	The beam is scanned along the sample surface and it builds up the image.

Table 27 Transmission electron microscope vs. Scanning electron microscope.

Components of SEM

SEM is now considered in more detail and is a primary tool used in this PhD program. Components of the SEM are:

(1) Electron gun

- Produces electron beams.
- Electrons are emitted when the solid is heated.
- A strong electric field is used to direct the electrons.

(2) Lenses

- Condenser lenses determine the number of electrons in the beam and the electron beam diameter.
- Objective lenses change the position of electrons focused on the sample.

(3) Scanning coil

- For scanning electron beams across the sample surface.

(4) Sample chamber

SEM Analysis process

- The analysis is performed using high-energy electron beams. A thermal source is used for the emission of electrons.
- The size of the spot which is produced from the gun is large to generate a sharp image and the lenses then compress the spot and focus the electrons onto the specimen.
- The image of the specimen is formed point by point and depends on the movement of the scan coils which causes the electron beam to move to a specific location in the form of a straight line.
- The emitted electrons are detected by an electron detector from the scanned sample. The collected signals are then displayed on the viewing screen and the brightness and intensity are controlled. Results are affected by the voltage mode. For example: if a voltage of 5 kV is used, the image will have rich surface information; whereas the voltage range, 15-30 kV allows for the penetration under the surface. A 3D SEM image depends on the topography visualization of the sample (such as shape, size, and surface texture).
- Data is collected over a selected area of the sample surface and a 2-dimensional image is produced to display spatial variations in the material properties. Areas in the range of 1 cm down to 5 microns can be imaged (McMullan D 1995).

The resolution of scanning electron microscope is about 2 nm. The resolution is limited by the width of the excited electron beam and the interaction volume of electrons in a solid. The resolution of a TEM is 0.2 nm, which is 1,000 times greater than a compound microscope and about 500,000 times greater than the human eye (McMullan D 1995).

Results and discussion

This section will provide a few results of prepared porous silicon membranes, attained by SEM imaging: plan view and cross-section.

High-Resolution Scanning Electron Microscopy (HRSEM) was used to study morphology using a Philips XL30 ESEM-FEG microscope and a 20 keV electron beam with prior nm-scale Au coating of membrane surfaces to minimize beam charging. In Figure 39, the SEM used in this thesis is shown.

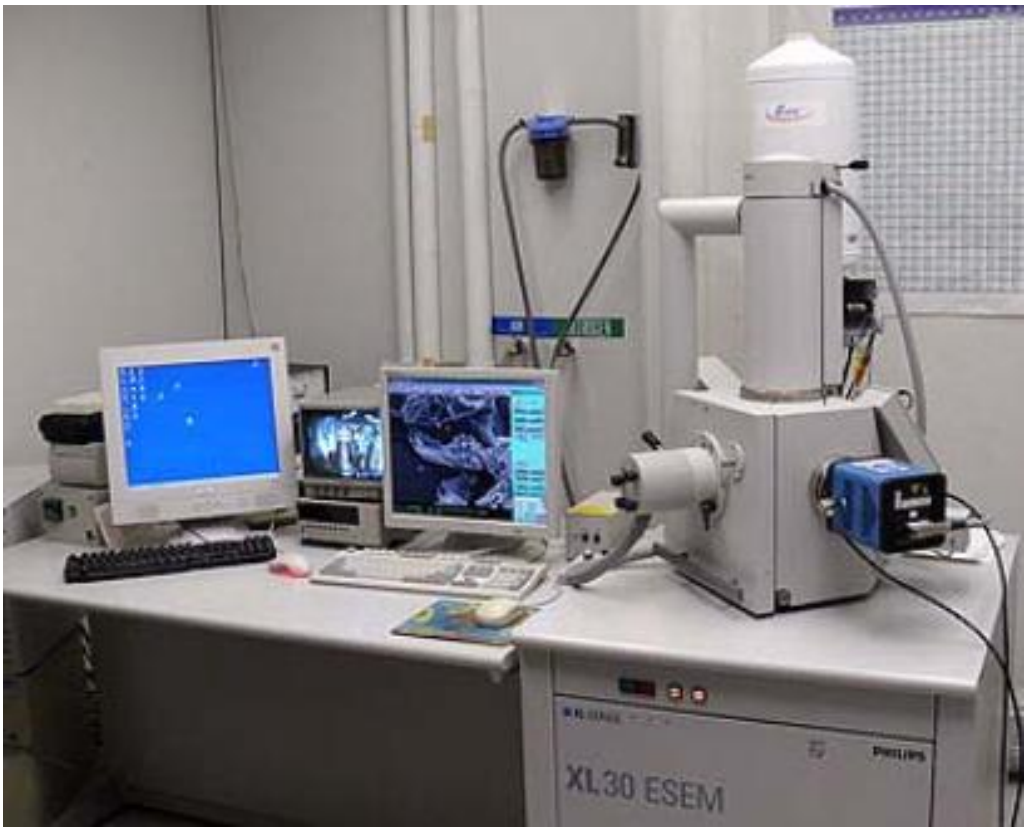

Figure 39 High-Resolution SEM microscope. Philips XL30 ESEM-FEG microscope.

Sample analysis process

The steps of a sample loading procedure are presented below, as well as some further imaging details.

- Before SEM imaging, the samples are pre-coated with gold to minimize the effect of the charge and to improve the material conductivity.
- Mount the sample on the SEM sample holder/stub.
- Check if the nitrogen gas for venting is on. SEM Imaging Software: press VENT and then OK.
- Load the sample into the main chamber. Important here is to check that the sample will not hit the detector while closing the door. Adjust the sample height. Press PUMP.
- Wait for pre-vacuum to reach the pressure of $1.3 \cdot 10^4$ before proceeding it should then say vacuum OK.
- The important step during SEM imaging is to ensure that the imaged spot is in the focus;
- When focusing, astigmatism also needs to be checked.

  An optical system with astigmatism is one where rays that propagate in two perpendicular planes have different foci. If an optical system with astigmatism is used to form an image of a cross, the vertical and horizontal lines will be in sharp focus at two different distances (Goldstein et al. 2003).

EDX-measurement details

Energy Dispersive X-Ray Analysis (EDX), also referred to as EDS or EDAX, is an x-ray technique used to identify the elemental composition of materials.

EXAMPLE 1

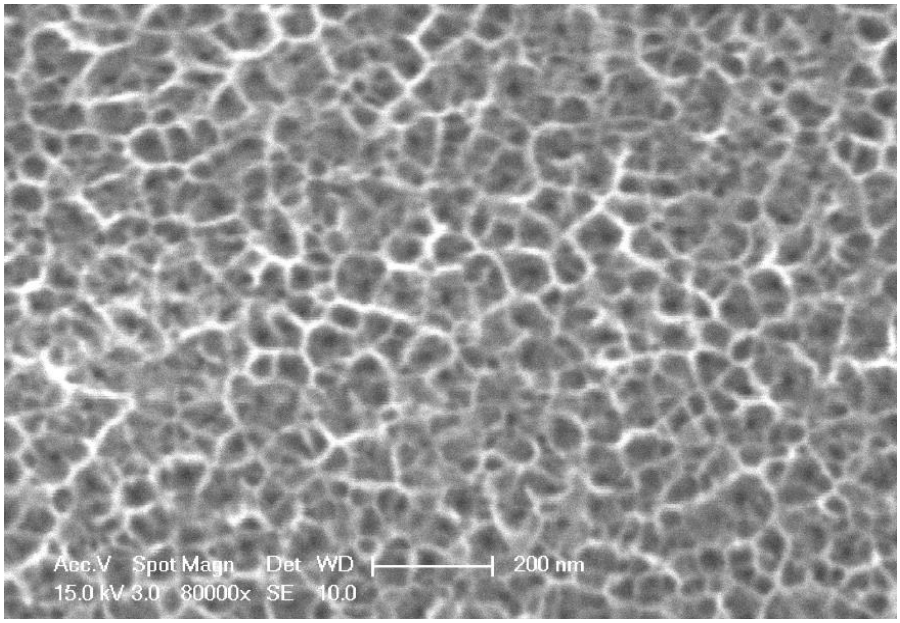

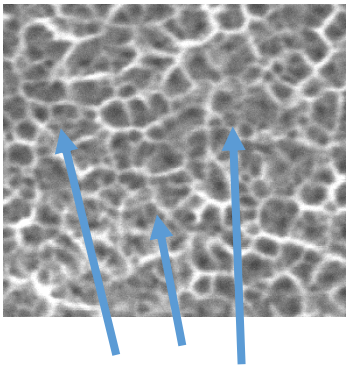

Presence of the smaller pores inside the bigger

Figure 40 A plan view image of a pSi membrane BN21-R1270 R1283 etched for 80 mins.

The thickness of the membrane is 165 microns. The voltage used here was 15.0 kV and the magnification of 8000X.

The BET data of the SEM imaged sample is shown in Table 28.

Sample code BN21 R1270-R1283	***Surface area (m^2/g)***	***Pore volume (cm^3/g)***	***Porosity (%)***	***Mean pore size (nm)***
As-anodized	118	0.32	44.9	7.5
4 hrs etched	256	2.00	82.3	20.2

Table 28 BET analysis of the sample with identification code BN21 R1270-R1283 which was SEM imaged above.

EXAMPLE 2

The following image (Figure 41) shows a directionality of the pores of the porous silicon membrane, with a respect to the top surface. This imaged sample (code UoB 20) was prepared via electrochemical anodisation and then supercritically dried. This same sample was subjected to two types of drying: air-drying and supercritical drying and the pore volume, surface area and mean pore size values are different when compared. SEM imaging was used to investigate further morphology of these nanostructures as well as to compare the pore sizes to the ones obtained by the Gas adsorption analysis.

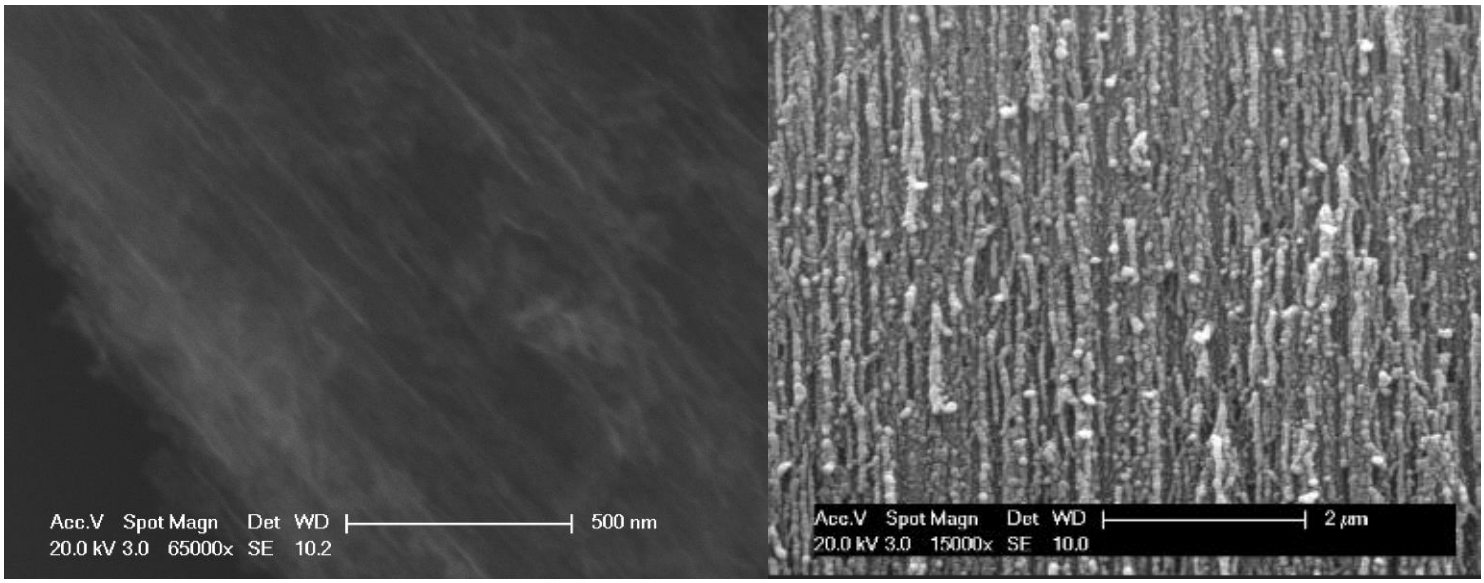

Figure 41 SEM image of sample UoB 20, showing a pore directionality.

BET data analysis of this imaged sample is shown in Table 29.

Sample Code	*Thickness (µm) (gravimetric)*	*Pore volume (ml/g) : AD/SCD*	*Porosity from pore volume (%) AD/SCD*	*Surface area(m^2/g): AD/SCD*	*Mean Pore size (nm): AD/SCD*
UoB 20	*195*	*2.65/5.13*	*86.0/92.3*	*520/549*	*16.3/31.3*

Table 29 BET analysis of sample code UoB 20, SEM imaged.

EXAMPLE 3

This example shows a plan view SEM image of a porous silicon membrane along with pore size analysis (Figure 42).

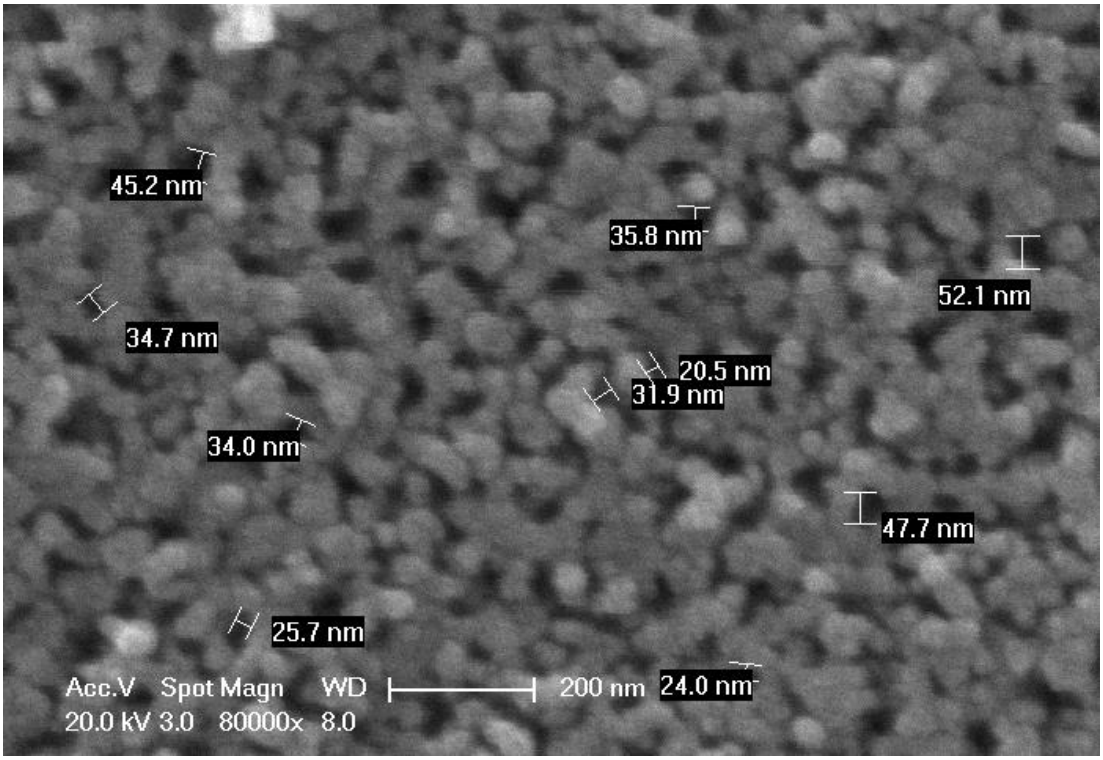

Figure 42 Plan view image of porous silicon membrane and pore size analysis measurements.

The voltage used was 20.0 kV and the magnification was 80000 X.

Measured pore size values are in the range of 24.0 nm to 52.1 nm. The feature used is the ruler from the SEM Software. The difference in the pore sizes arises from the characteristic of electrochemical etching. It is due to the difference between the top and the bottom part of the membrane. Furthermore, the top part is longer under the etching conditions as the pores form and grow at the tip deeper into the substrate over time, which lead to the larger pore sizes. The previous fact happens under the electropolishing conditions where the current density is elevated in comparison to the anodisation current density value. Therefore, the interface between the membrane and the wafer is completely dissolved and the membrane detached. The bottom face of the membrane opens up during the electropolishing and accordingly detachment of the membrane

EXAMPLE 4

Another type of SEM image is a cross-sectional image that is used in this doctoral thesis for comparison to calculated thickness values using the gravimetric method (Figure 43).

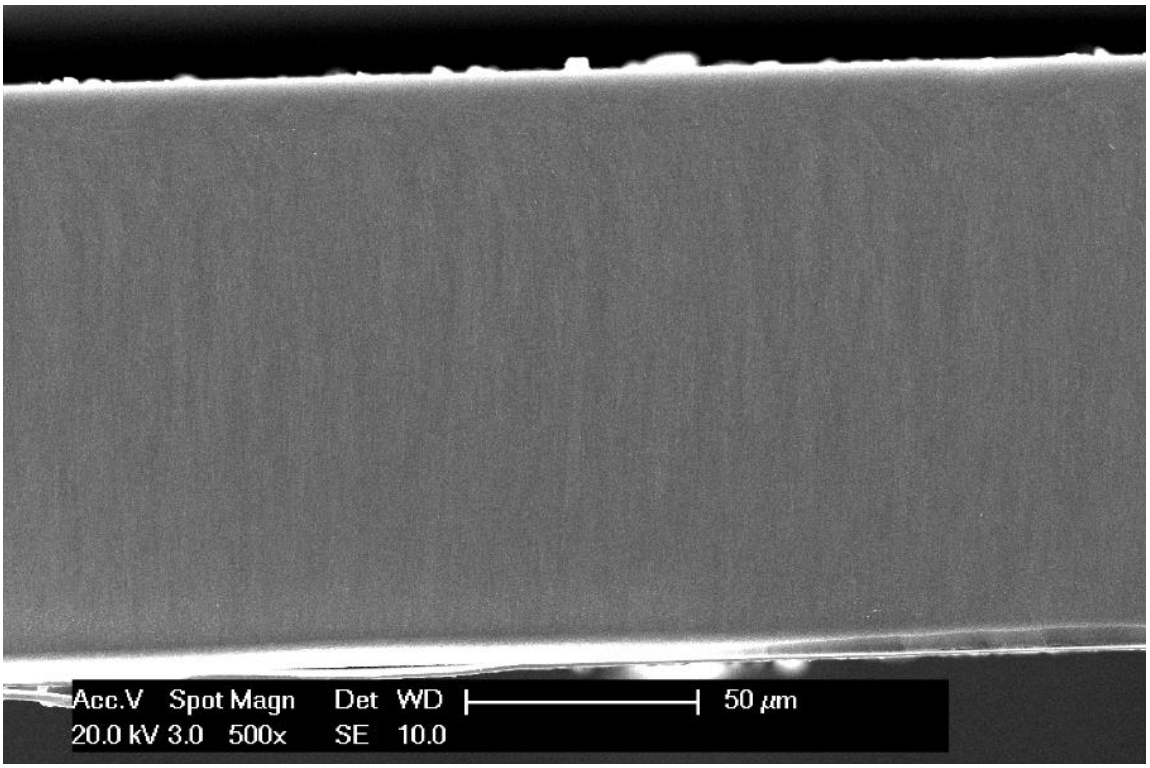

Figure 43 A cross-section SEM image of porous silicon membrane UoB 20.

The thickness value of this pSi sample obtained by the gravimetric method was 195 microns. By contrast, an average thickness value of 189 microns was obtained from a total of 12 cross-sectional thickness measurements.

In Table 30, values of thickness measurements obtained by software ImageJ are shown. ImageJ is an image processing software. It can display, edit, analyse and process SEM images.

Measurement	***Thickness (µm)***
1	188
2	192
3	182
4	181
5	181
6	193
7	189
8	193
9	189
10	195
11	194
12	190
Average value (µm)	189
Standard deviation (µm)	5
Error on the mean (µm)	1

Table 30 Thickness measurements of sample code UoB 20 obtained by ImageJ software.

Inaccuracies in the thickness measurements using the gravimetric technique can arise due to inaccurate weight measurements because of some membrane fragment losses. It is often extremely difficult to retrieve every last fragment of the membrane and this can lead to weight inaccuracies which can ultimately affect the thickness measurements. The final result is 189 µm ± 1 µm.

EXAMPLE 5

This example of a cross-sectional SEM image of the porous silicon membrane is shown in Figure 44.

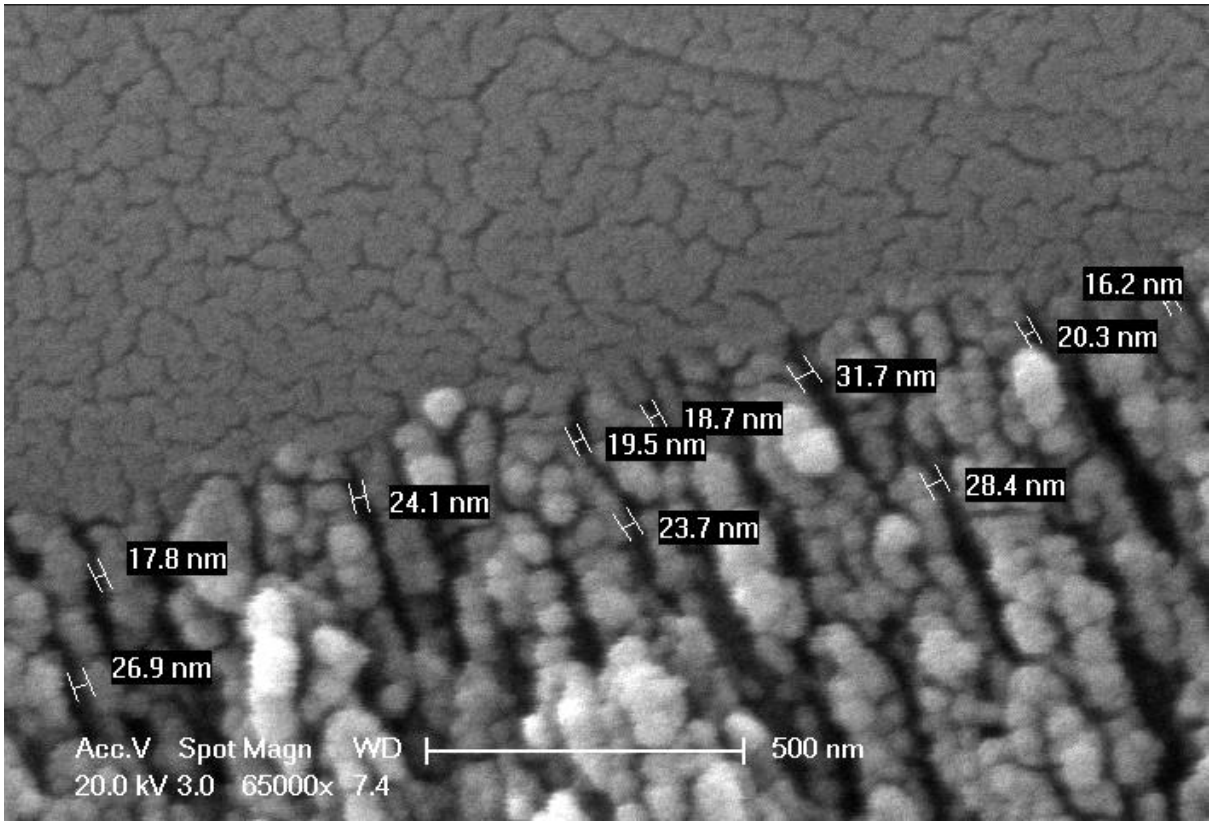

Figure 44 A cross-sectional SEM image of the sample UoB 20.

The voltage used was 20.0 kV and the magnification value was 65 000x. The measured pore size is in the range of 16.2 nm to 31.7 nm. Furthermore, the value of the mean pore size obtained by gas adsorption analysis, BET was 30.5 nm. The standard deviation value, in this case, is 5.06 nm. The much lower values of pore diameter extracted from electron microscopy are due to the ultrathin gold coating necessary to acquire good images.

Conclusions

This section provided some basic contents about the scanning electron microscopy (SEM) technique as well as some examples of SEM images of porous silicon membranes. The main aim of SEM images is studying the nanostructures, pore size, pore impregnation, measuring thickness, etc.

Some examples of the SEM images, both plan-views and cross-sectional views have been provided together with relevant details and explanations. Plan-view images were mainly used towards pore size determination and the cross-sectional images are employed for the thickness measurements and comparison to gravimetric data. Furthermore, the standard deviation values are calculated. In this doctoral thesis, these images were of benefit for morphology studies.

Moreover, Using CSEM and LVSEM can lead to the prevention of excess scattering of the electrons, eliminate the defocusing of the electron beam, and also produce a high-resolution image.

A combination of EDS with SEM is very important for quantitative and qualitative analysis of the specimen. Without EDS, only surface topography information can be produced via SEM.

4.3. Porosity determination by JMicrovision software

Introduction

JMicrovision is an image analysis toolbox written for measuring and quantifying the components of high-definition images. The program contains most of the common image processing operations, has an efficient visualization system (Smith et al. 1992). The main reason for choosing this analyser software is to measure the average pore size and determine the porosity of a porous silicon membrane by image processing of top-view scanning electron microscope (SEM) micrographs (McMullan D 1995). Results using this method will be compared with gas adsorption analysis data as well as gravimetric method data. Standard deviations of the various methods have been calculated.

Experimental methods

Electron microscopy/SEM imaging—High-Resolution Scanning Electron Microscopy (HRSEM) was used to study porous silicon morphology using a Philips XL30 ESEM-FEG microscope and 20 keV electron beam with prior nm-scale Au coating of membrane surfaces to minimize surface charging.

Image processing-Pore dimensions are determined using the JMicrovision 1.2.7. software. There are three steps in the processing of each image. The first step is the application of a mathematical-morphological filter ("closing") to filter out the morphological noise that comes from small closed shapes within the pores. The second step involves segmentation of the shapes of the pores and was done by a simple binarization operation where each shape is identified using an iterative bisection histogram. This process is repeated until there is no more change in the threshold value.

Results and discussion

Pore diameter and porosity were calculated using both the gravimetric method and gas adsorption analysis and the results are presented in Table 31. The porosity was also measured using software and the value is presented in the table below.

Sample code	Thickness (µm)	Porosity (%) (Gravimetric)	Surface area (m^2/g)		Pore volume (cm^3/g)		Porosity from pore volume (%)		Pore diameter (nm)	
			AD	SCD	AD	SCD	AD	SCD	AD	SCD
UoB 41	118	87.13	421	443	2.45	2.62	85.00	85.80	18.97	19.78

Table 31 Gravimetric and Gas adsorption (BET) data of the sample UoB 41 which was subsequently used in JMicrovision 1.2.7. analysis of average pore diameter and porosity.

Software package JMicrovision 1.2.7. is then subsequently used to estimate these values after which all four methods were compared.

Gas adsorption analysis data is shown below in Figure 50. The adsorption cumulative pore volume as a function of pore diameter is calculated using the Barrett-Joyner-Halenda (BJH) adsorption method; surface area via the Brunauer-Emmet-Teller (BET) method and average pore diameter was estimated from the adsorption branch (4V A^{-1}) method by BET. BET analysis provides precise specific surface area evaluation of materials by nitrogen multilayer adsorption measured as a function of relative pressure using a fully automated analyser. BJH analysis can also be employed to determine the pore area and specific pore volume using adsorption and desorption techniques. This technique characterizes pore size distribution independent of the external area due to the particle size of the sample (Sailor 2011).

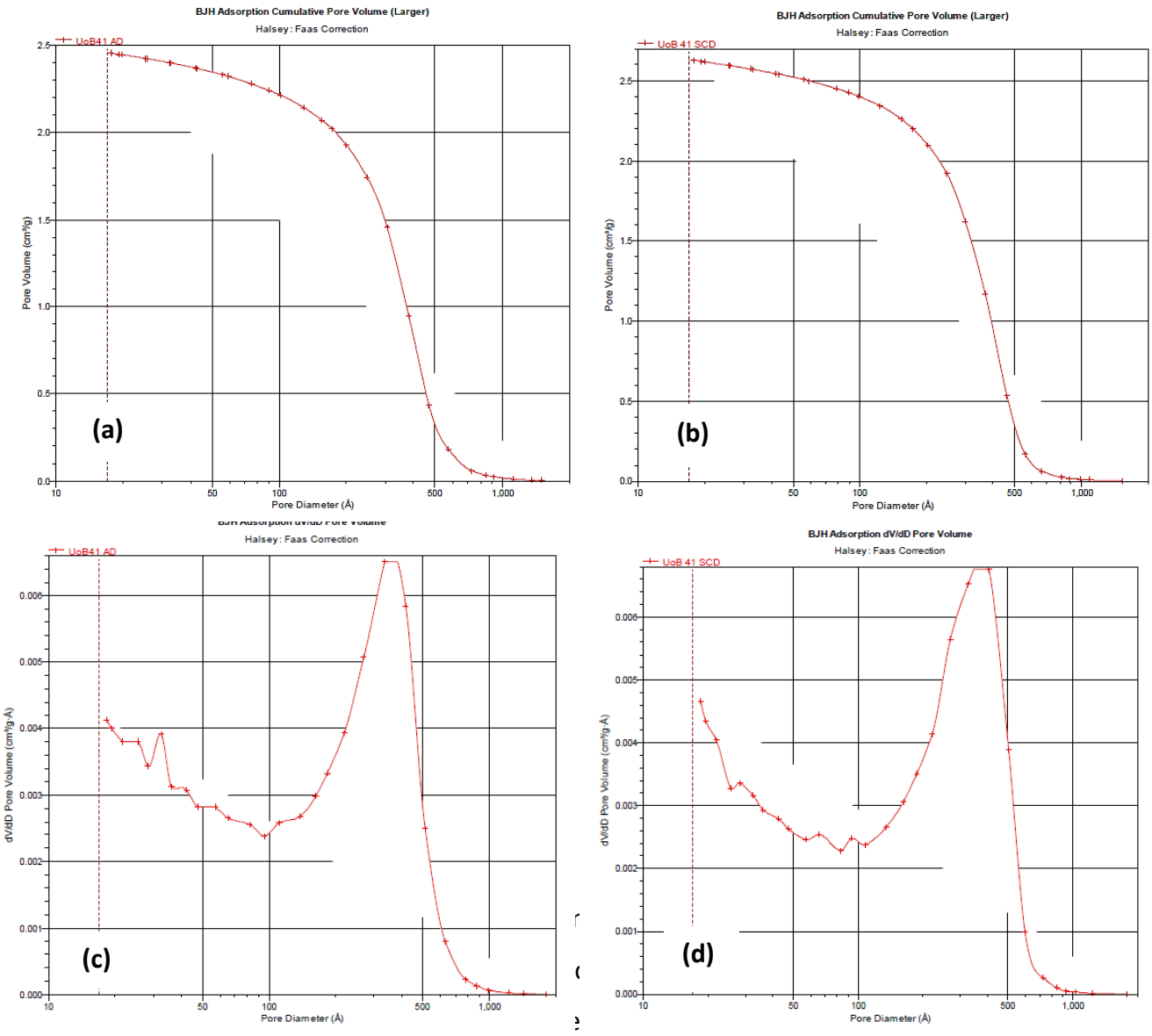

Figure 45 Pore volume vs. pore diameter for p+ UoB 41 porous silicon membranes. (a & c) Air-dried pSi and (b & d) supercritically-dried pSi.

This can be investigated by plan view SEM imaging where such cracks and shrinking can be observed in the case of air drying and no cracking and shrinkage for supercritical-drying.

Figure 46 shows such cracking of pSi membrane during air-drying.

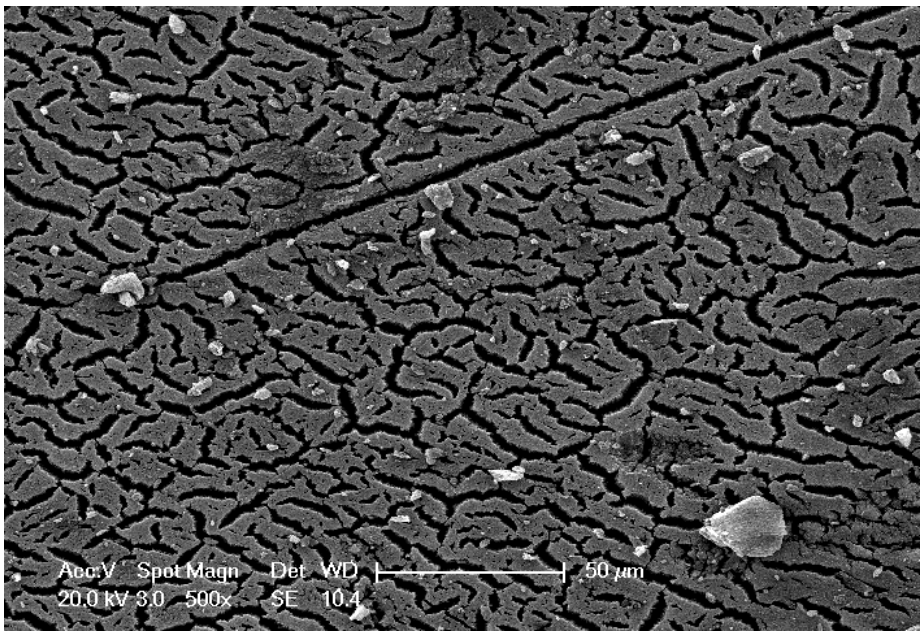

Figure 46 SEM image of the pSi membrane cracks during air-drying.

Furthermore, the sample was prepared for SEM imaging. Before imaging, the sample was coated with a layer of gold to avoid beam charging and improve the conductivity of the material. The sample was then imaged before software analysis. Therefore, coating with gold substantially lower the porosity and pore sizes and therefore the software analysis will give lower values than expected. The plan view image of sample SCD UoB 41 is shown in Figure 47.

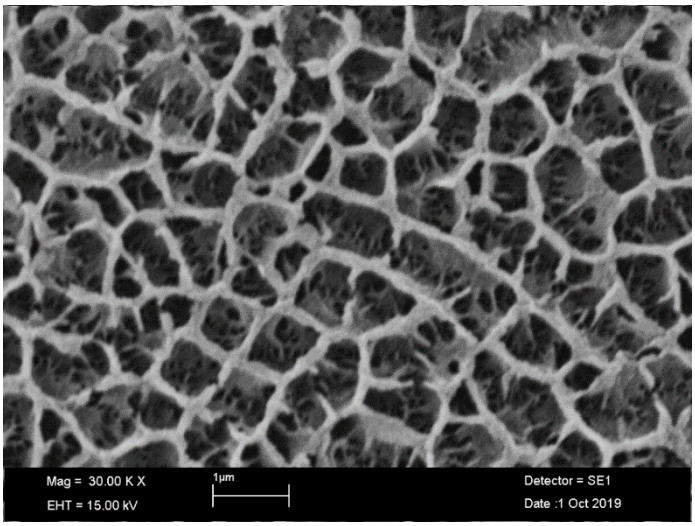

Figure 47 Plan view SEM image of the sample named UoB 41.

The aforementioned processing steps are presented in the figure below showing 3D projection to 2D (Figure 48).

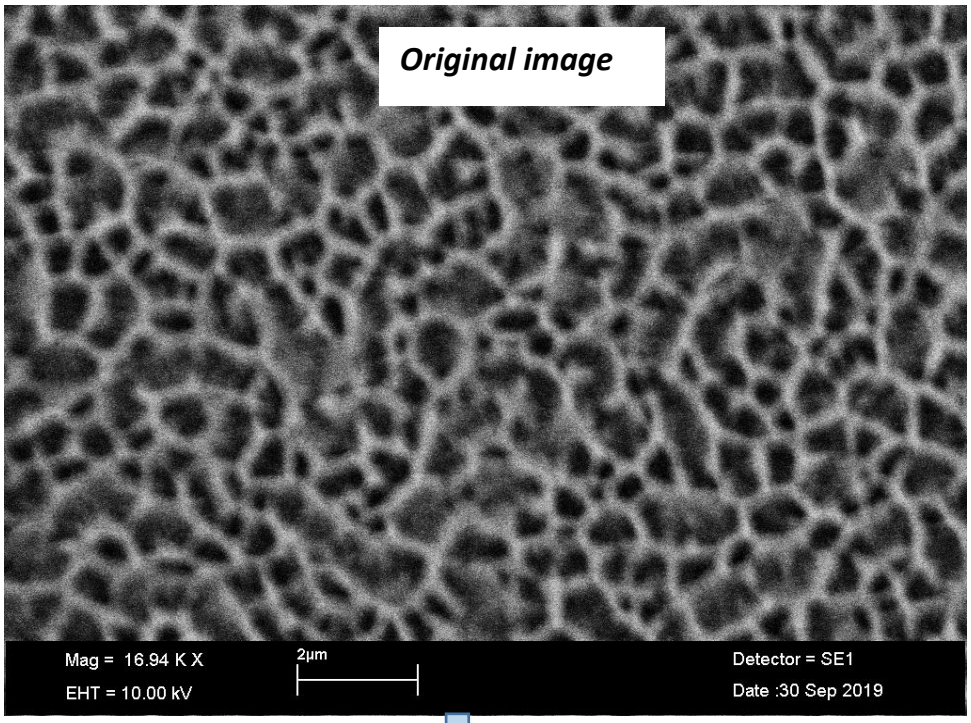
Original image
Mag = 16.94 K X
EHT = 10.00 kV
2µm
Detector = SE1
Date :30 Sep 2019

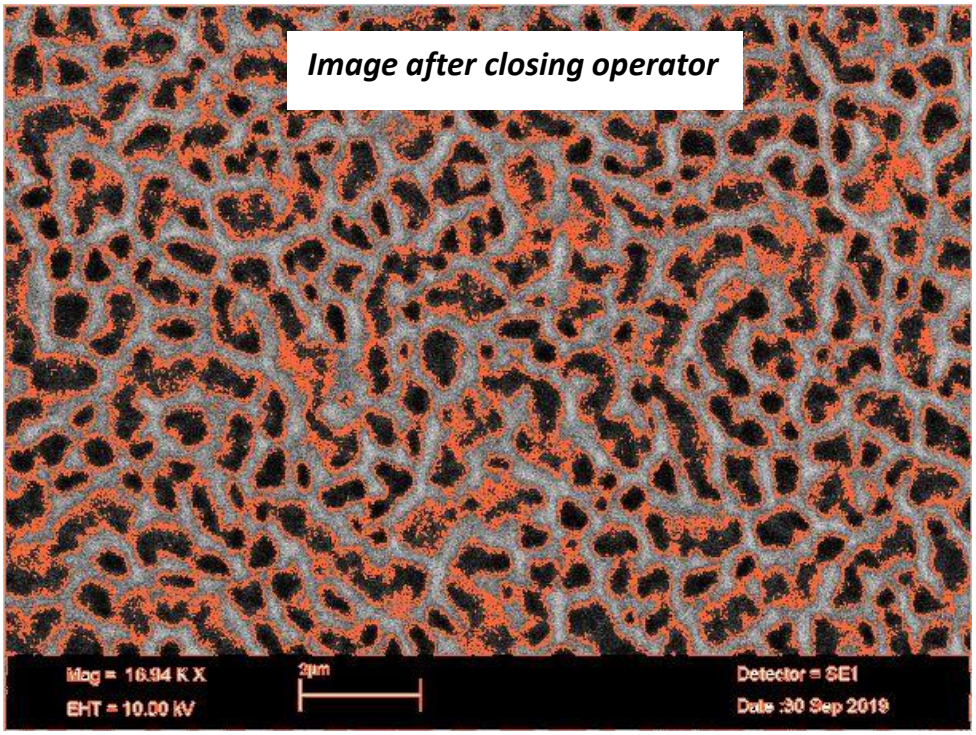
Image after closing operator
Mag = 16.94 K X
EHT = 10.00 kV
2µm
Detector = SE1
Date :30 Sep 2019

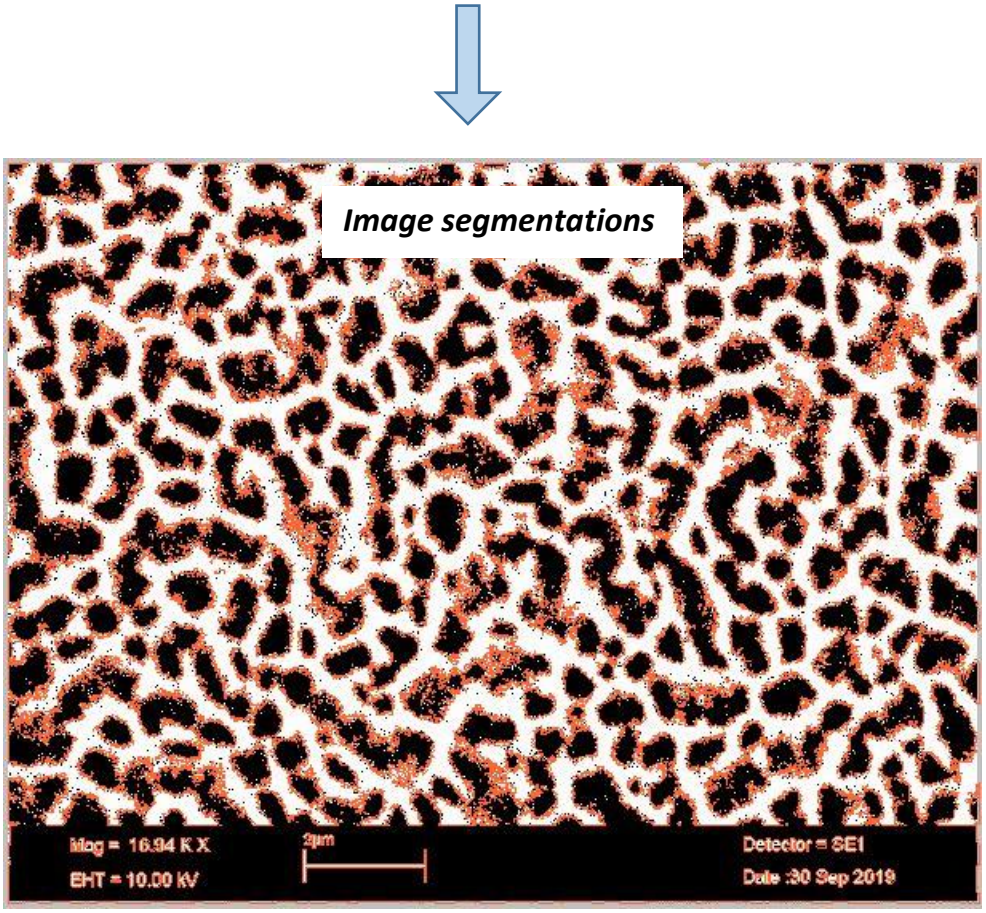

Figure 48 Images from each processing step.

Psi membranes were produced using a double-tank cell. The anodisation time and current were 30 minutes and 15 A, respectively. In this study, HF concentration was kept constant while the current densities have been varied. An electropolishing current higher than the anodisation current has been applied to lift-off the membrane. Details of this sample are shown in Table 35. The average diameters of pores, as a function of the current density and HF concentration, were determined by direct measurements on the SEM images, which were based on average area, and perimeter measurements.

Analysis data of the sample UoB 41 is shown in Table 32.

The total number of measurement records performed is 29 and the different properties have been analysed, such as area, perimeter, barycenters, orientation, length, width, eccentricity, compactness, elongation etc. Moreover, porosity was calculated as the ratio between pore volume and the volume of the entire membrane. It is important to image the uniform pores by SEM imaging. Porosity measurement values are also presented in Table 32.

To investigate the validity of the results, included in Table 32, a comparison between the different methods of obtaining the values for pore size and pore volume/porosity was performed. Standard deviation values were 7 nm and 12 %, respectively.

Area of the image analysed	***Porosity value measured by the software (%)***
1	59.30
2	60.5
3	63.9
Standard deviation (%) in comparison to BET analysis	12.04

Table 32 Analysis data of the sample UoB 41 achieved by Software JMicrovision 1.2.7.

During the image processing, it is important to first split the channels of the image, use RGB colours, choose the threshold and to analyse the particles (with showing results and with summarising them).

Inaccuracies can arise from errors made during weights measurements (gravimetric method) where some of the material might not be successfully reclaimed or when the wafer has not been completely dried so the weight can keep increasing. Alternatively, sometimes small pores are omitted during image analysis. This is because the avoidance of the small pores has a negligible effect on the results, which have an impact on the calculation of the porosity. Even if there is a large number of these small pores, their contribution to the total porosity is still negligible.

Conclusions

Image processing of SEM plan-view images can be used for pore size and porosity determination, irrespective of layer thickness, and can be applied to uniform thickness membranes of various pore morphologies (Elia et al. 2016). Furthermore, it is used for assessing the average pore size in a variety of samples.

In this doctoral thesis, the results obtained by this software have a standard deviation of 12.04 % for porosity and 7 nm for the mean pore size, in a comparison to already mention methods. In general, porosity increases with an increase in the current density. This indicated the immediate pore formation over the area of the silicon sample when the current is applied. Outlook regards this section is a possibility of a programming model, which is applied to the SEM image and can automatically provide pore size and porosity data. The advantages would be the attaining the data automatically and then compare it to the other methods used, such as gravimetric method and BET analysis.

4.4. Particle size measurements

Introduction

This section will focus on particle size characterization using a Malvern Instruments Mastersizer 2000. The following topics will be covered:

- Light scattering by particles.
- What does Mastersizer do?
- How does Mastersizer work?
- Measurements procedure.
- Results overview.
- Saving the results.
- Data analysis.

One of the simplest theories for explaining the way particles scatters and absorb light is using the Fraunhofer model. This model provides a scattering pattern when a solid of known size is passed through a laser beam. Theory-based on this assumption is called Mie theory. Mie theory predicts the way light is scattered by small spherical particles and by the interactions between the light and the particle. The key factor in this theory is the particle size. Each particle will have a specific scattering pattern, which differs from other ones.

Experimental methods

The sample placed in the vial has been vortex mixed before the measurements. The sample is then delivered to the optical bench. Scattering patterns (intensity) from the sample are captured by the detector and analysed by the Malvern software whereby particles from each scattering angle are correlated with particular particle size. Therefore, larger particles scatter less and smaller particles scatter more.

To prepare samples ready for particle sizing, first, a pSi powder may be mixed with a surfactant. As-anodized porous silicon is hydrophobic so this is important when using DI as a dispersant. However, if using a dispersant such as ethanol, no surfactant is needed as ethanol wets to the pores very well.

Creating a standard operating procedure before carrying out measurements is a necessary step. The matters involved are optical properties of the sample and dispersant, suspension, duration of stirring, amount of ultrasonic dispersion and additives required.

The Malvern Mastersizer 2000 equipment is shown in Figure 49.

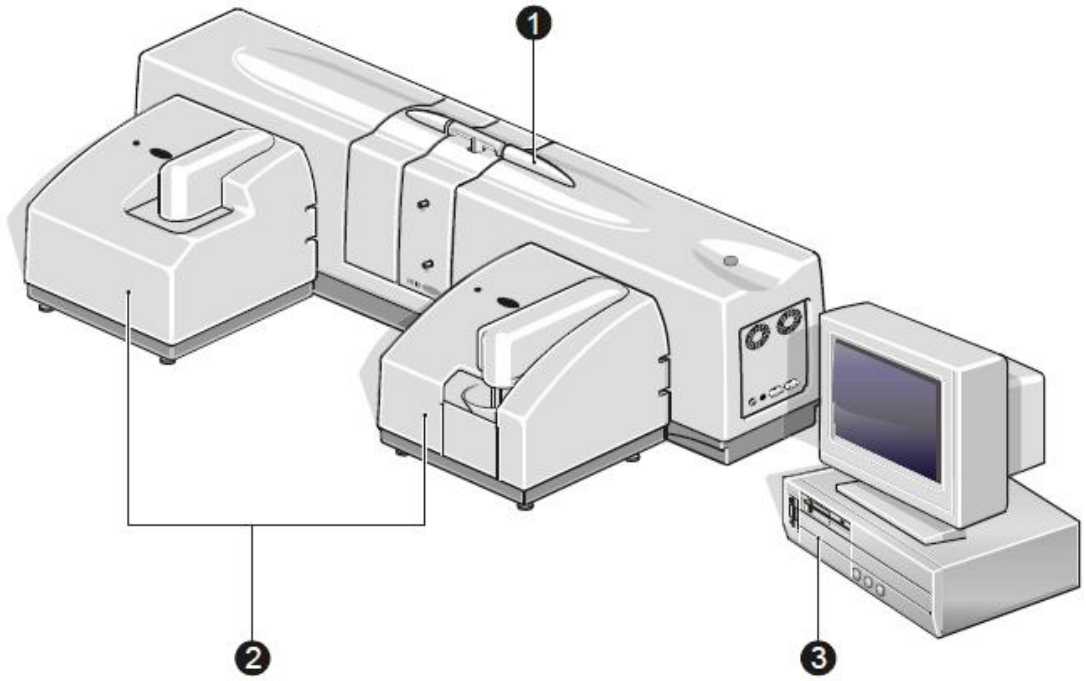

Figure 49 A graphical representation of the Malvern Mastersizer 2000. Identified features include (1) an Optical bench, (2) one or more sample dispersion units, and (3) a Computer system.

- *(1) The optical bench* is used for raw data collection used to calculate the particle size in the sample using the aforementioned Mie theory.
- *(2) One or more sample dispersion units*: the purpose of this part of the equipment is to prepare the sample and deliver it to the optical bench for measurements. Many sample forms can be handled, such as dry powders and samples dispersed in a liquid.
- *(3) Computer system*: a stand-alone unit that runs the Malvern software. It controls the optical bench and dispersion units and analyses the raw data collected.

Optical bench apparatus

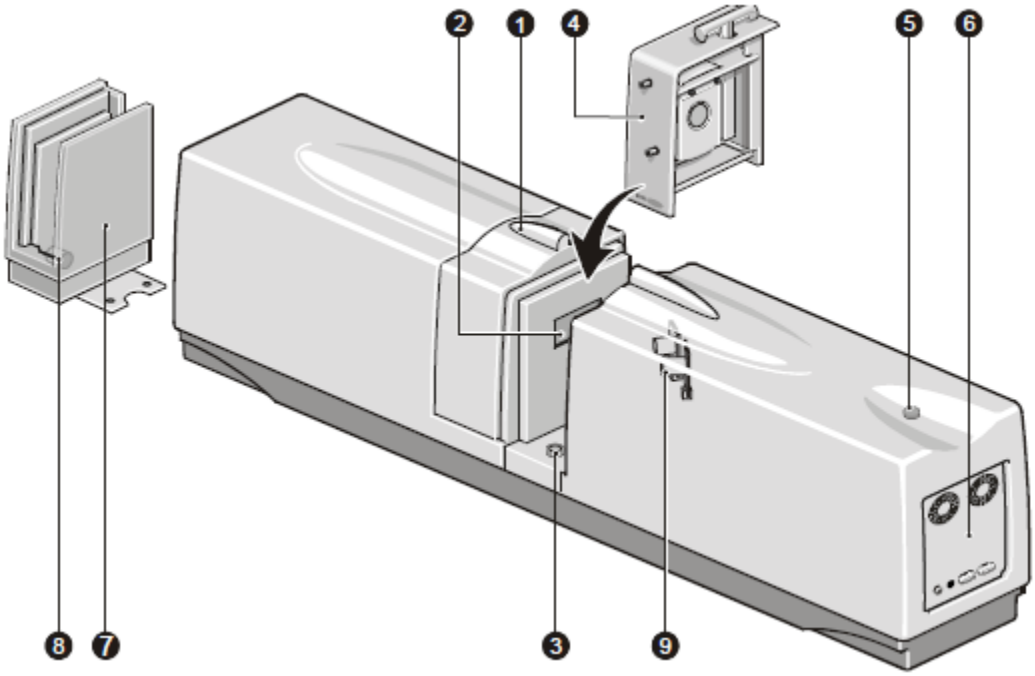

Figure 50 Optical bench components.

Components of the optical bench from the figure above:

(1) Cell area protection cover: this area prevents dust and dirt contamination.

(2) Protection window: stops dirt and dust from entering detectors.

(3) Drain: allows possible spillages to exit onto the workbench.

(4) Cell: interface between the sample dispersion unit and the optical bench. The sample is passed between two cell windows through which the laser passes, allowing it to be analysed by the laser beam.

(5) Power indicator: illuminates when the optical bench is turned on.

(6) End panel: contains all connectors for the optical bench.

(7) Cell holder: area for holding the unused cells.

(8) Window tool: for removing the windows from the cell if they need cleaning or replacing.

(9) Backscatter detectors: collecting the light scattering data from the sample.

Malvern software

The software controls the measurements and processes them to produce a size distribution. The software analyses the raw data and includes a user interface which consists of:

- The interface for defining a standard operating procedure (SOP), running a measurement, displaying the results, and printing the reports.
- The report designer, which allows creating custom reports for results displaying.
- Measurements window, which displays the data of selected records. In this part, the size distributions and graphs together with tables are displayed.

Sample preparation

Both dry and wet samples can be used for particle sizing. During sample preparation thorough mixing of samples is vital, for example, dry samples can separate during storage, with large particles escalating to the top whilst the smaller ones collect at the bottom. To counteract this, prior sample mixing is suggested. Wet samples require correct dispersion in the liquid dispersant; if the wrong dispersant is used, such as water in the case of a hydrophobic pSi, the sample can form clumps, float on the surface, or even dissolve.

Adding the sample

The amount of sample required for a measurement is closely monitored by the software. Here the laser beam measures the obscuration level of the sample. The sample should be added to fall within optimum obscuration limits (Table 33).

Obscuration range (%)	Obscuration graph colour	Notes
<5	red	Add more sample.
5-10	orange	Low but usable with a good signal to back-ground ratio.
10-20	green	Ideal.
20-50	orange	Usable but try to add more dispersant - there's a danger of multiple scattering.

Table 33 Obscuration range notes and a relevant graph colour explained.

The software requires control of the obscuration of the laser beam, which is caused by the sample. The obscuration is explained as the fraction of “loss” light from the main beam once the sample undergoes the measurement. For example, 40% obscuration means that 40% of the incident laser beam is lost due to absorption or scattering. Table 35 gives an overview of the obscuration range (%) with relevant graph colour and additional notes.

Software measurements steps:

- A status area on the screen-indicates changes as the measurement progress;
- Measure background-data from the particle field is contaminated by electrical noise. This electrical noise can arise from the background as well as the scattering data from dust which is located on the optics and float in the dispersant. Background measurements are used to define a measurand known as input quantities in a measurement model.
- Add sample-indicates for the sample to be added to the measurement tank, the system then measures how much of the sample is added and monitors the obscuration limit.
- Measure sample-a command to start the measurement.
- Result-shows calculated size distribution.

Understanding of displayed data

The analysis results are presented in the form of relative volume distribution of the particles in the size classes range (Figure 51).

The common form of the displayed graph is shown below: Figure Malvern Mastersizer 2000 particle size data.

(1) Histogram-displays the results as the “in-band” percentages. A size band of particles is presented as each bar.
(2) Result-under plot (cumulative undersize/results less than)-displays the result in the percentage form below a certain particle size. The exact value is readable from the table which accompanies the graph. The result is calculated from initial size bands

which are done by the curve fitting to the analysis data so the values within the size band can be read.

(3) Result-over plot-similar to the previous point. For example, reading from the graph it is visible that 90% of the sample is under 23 microns.

(4) The frequency curve-the frequency can be used towards showing the peaks in the graph. The peak provides the particle diameter.

Experimental methods

Before taking a sample for the measurement, it is very important to make sure that the sample is representative of the whole sample.

In addition to the processes described above, an ultrasonic bath can be applied to help with dispersion, with or without a surfactant. Applying two minutes of ultrasonic can help in the situation where large agglomerates of particles tend to sink to the bottom of the beaker. This will automatically break up the large particles and formed agglomerates.

Moreover, in terms of the choice of the dispersant-majority of samples allow the water to be the dispersant. If the sample is hydrophobic, a surfactant needs to be added to the dispersant. Adding a surfactant helps by removing the surface charge effect on the sample that can cause clumps or the sample to float on the surface. Recommended surfactants are as follows: Igepal, Teepol, Synperonic, Aerosol, and Hyamine. In this doctoral thesis, Igepal was used. If the dispersant is stored at low temperature or under pressure, degassing before use is necessary. It leads to the reduction of the gases solubility. Bubbles can cause problems in measurements as they can be counted as particles. The solution for this is to store the sample at room temperature and the lower pressure for degassing, as already mentioned above. Ultrasonication prevents re-agglomeration.

In conclusion, after the measurement information has been collected and analysed, it has been displayed in forms. The records tab is opened automatically. Selecting this tab all the records will be shown. On top of the window, the series of tabs will be available. To change between the reports, it is simple to select another tab. This was all discussed previously.

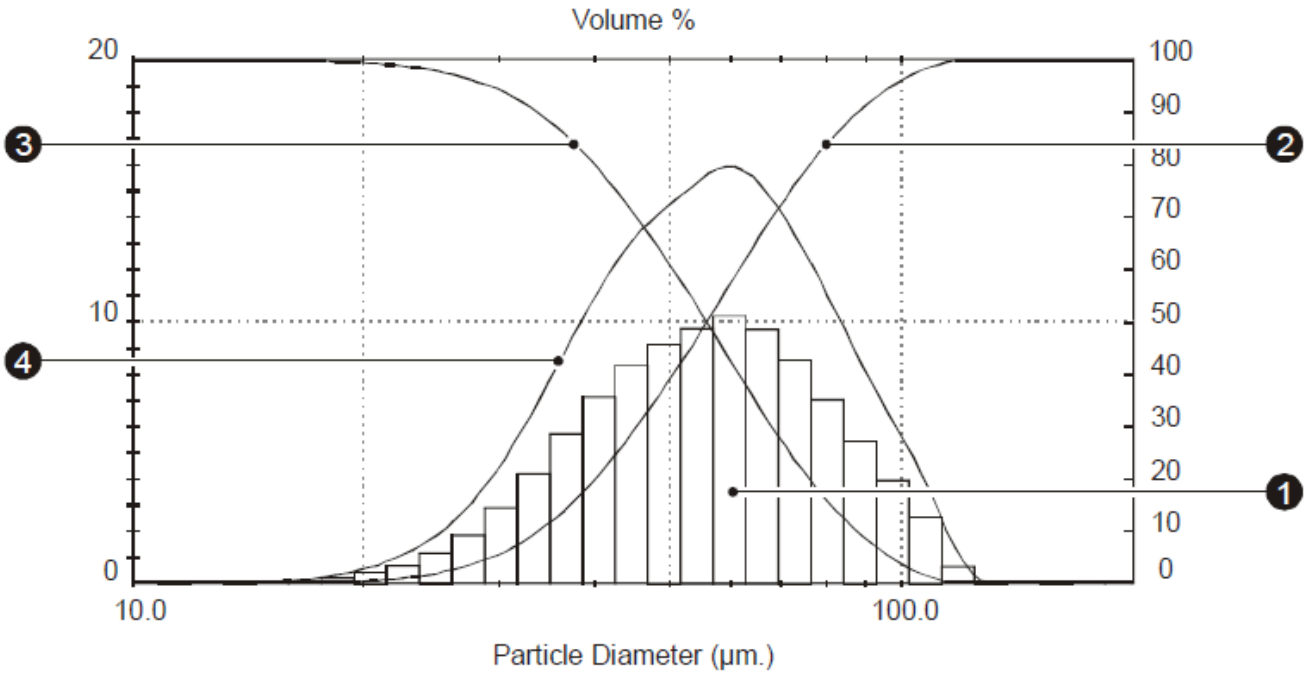

Figure 51 An example of plot Volume (%) vs. particle diameter (µm) from Mastersizer 2000.

Mie Theory

The Mastersizer 2000 uses the Mie theory for solving the interaction of light with matter.

Mie solution of the Maxwell equations defines the scattering of an electromagnetic plane wave by a homogeneous sphere. Hence, the solutions consist of a spherical multipole partial waves named after Gustav Mie. Mie theory is usually employed in electromagnetic simulations of the spherical nanostructures (Stratton 2007). The term Mie usually refers to a collection of Maxwell's equations for particle scattering. In this theory, the approximation made is that the size of the scattering particles is equivalent to the wavelength of light.

There are no limitations for the upper particle size values. The explanations of the Mie theory can be found in the book *Electromagnetic theory* by J. A. Stratton (Stratton 2007).

The Mie theory formalism is based on the calculations of the electric and magnetic fields from the inside and the outside a spherical objects. It is used to calculate the amount of the scattered light. The intensity of the scattered radiation is given by the equation:

$$I = I_0 \left(\frac{1 + \cos^2 \theta}{2R^2} \right) \left(\frac{2\pi}{\lambda} \right)^4 \left(\frac{n^2 - 1}{n^2 + 2} \right)^2 \left(\frac{d}{2} \right)^6, \quad (8)$$

where I_0 is the light intensity before the interaction with the particle, R is the distance between the particle and the observer, ϑ is the scattering angle, n is the refractive index of the particle, and d is the diameter of the particle.

It is obvious from the equation that Rayleigh scattering depends on the particle size and the wavelength of the light. The intensity of the radiation increases with increasing the ratio between the particle size and the wavelength of the light. Hence, the bigger the particle size, more light is scattered.

The values commonly calculated using the Mie theory are the efficiency coefficients.

An optical model for scattering will use data obtained in the measurements. In this objective, we need to build a model that will calculate scattering for different samples depending on different concentrations, particle sizes. This objective will achieve a comparison between the theory and experiment.

Absorption and scattering efficiencies of light scattering by small particles, can be calculated based on the following equations and we are going to use them in our model:

$$\boldsymbol{Q_{abs} \approx 4x\,(\varepsilon - 1/\varepsilon + 2)} \quad (9)$$

$$\boldsymbol{Q_{sca} \approx 8/3(|\varepsilon - 1/\varepsilon + 2|2)} \quad (10)$$

where the x is the particle's size parameter divided by the wavelength $2\pi a/\lambda$ and ε is the dielectric constant of the particles.

Dielectric constant can be controlled by changing the optical constant of the sample, which means measuring different reflectance and transmittance for different angles.

The results of the modelling are shown in the Figures 52 and 53.

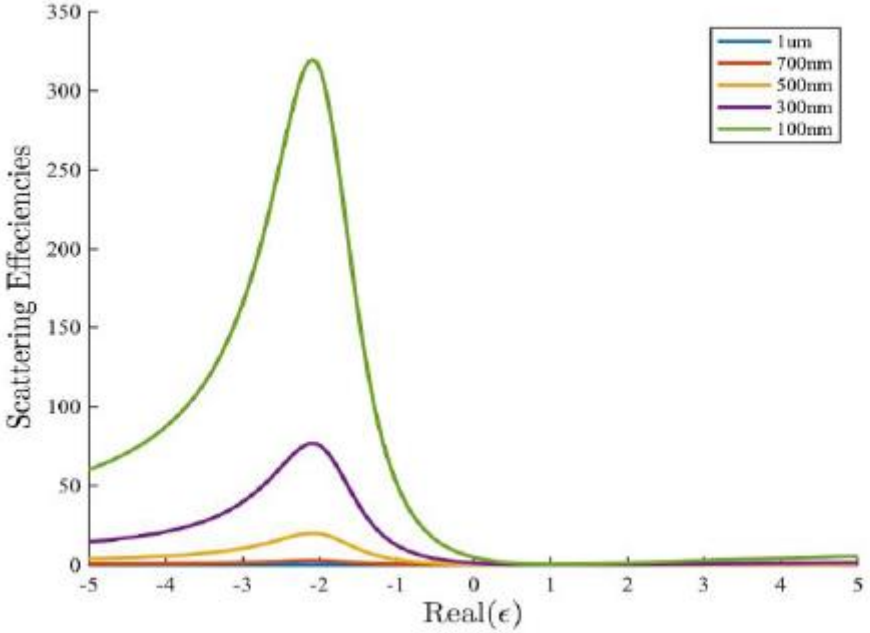

Figure 52 Scattering efficiencies for pSi in KBr with particles sizes: 100 nm, 300 nm, 500 nm, 700 nm and 1 um.

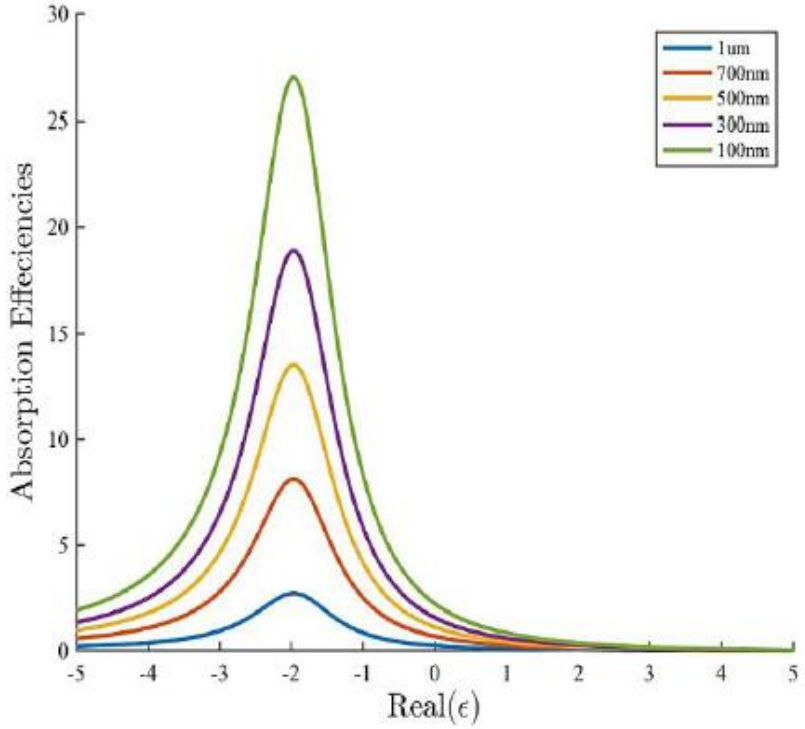

Figure 53 Absorption efficiencies for pSi in KBr with particles sizes: 100 nm, 300 nm, 500 nm, 700 nm and 1 um.

It is possible to control those efficiencies by controlling dielectric constant. In the case of ε=1, the sample is transparent as Qabs is 0. If ε=-2 , there is a strong extinction and the efficiencies go to infinity.

In summary, the Mie theory assumes that the particle is spherical. The following parameters have to be specified:

- Real refracted index-amount of scattering which takes place as a result of light interacting with the particle.
- Imaginary refractive index-amount of absorption, which takes place when the light enters the particle.
- Density-used to calculate the specific surface area.

The possible applications of Mie theory are found in meteorological optics, where ratios diameter of the particle and the wavelengths are the unit of order larger. Furthermore, the applications are in the optical scattering measurements. It is also used for cancer detections where the scattered light of the tissue is analysed using angle-resolved coherence interferometry.

Mie theory is also employed in the laser diffraction analysis where is it utilized to explore the particle sizing.

Appendices

Table 34 shows additional information about particle sizer (Mastersizer 2000).

Size range	0.02 to 2000 microns.
Measurement principle	Mie scattering
Light sources	Red light: Helium-neon laser. Blue light: Solid-state light source.
Optical alignment system	Automatic alignment of the system with dark-field optical reticle and multi-element alignment detector.
Sample dispersion unit interchange system	Automatically recognized, configured, and enabled on insertion of the measurement cell into the optical bench.

Table 34 Additional information about particle sizer (Mastersizer 2000).

MASTERSIZER 2000

Result Analysis Report

Sample Name:
Batch 66C

SOP Name:

Measured:
08 May 2017 12:22:13

Sample Source & type:

Measured by:
User

Analysed:
08 May 2017 12:22:14

Sample bulk lot ref:

Result Source:
Measurement

Particle Name: oxidised porous silicon

Particle RI:
1.300

Dispersant Name: Water

Accessory Name: Hydro 2000MU (A)

Absorption:
0.1

Dispersant RI:
1.330

Analysis model: General purpose

Size range:
0.020 to 2000.000

Weighted Residual:
4.380 % um

Sensitivity: Normal

Obscuration:
6.20 %

Result Emulation:
Off

Concentration:
0.0066 %Vol

Span :
2.169

Uniformity:
0.717

Result units:
Volume

Specific Surface Area:
1.11 m²/g

Surface Weighted Mean D[3,2]:
5.397 um

Vol. Weighted Mean D[4,3]:
13.028 um

d(0.1): 2.662 um **d(0.5):** 10.584 um **d(0.9):** 25.614 um

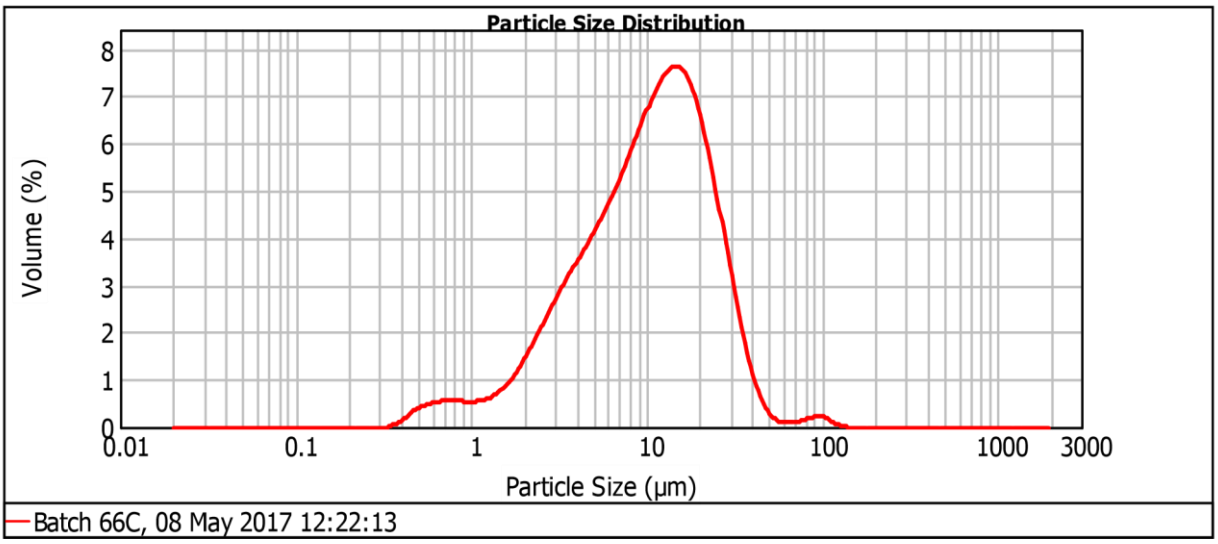

Size (µm)	Volume In %
0.050	
0.056	0.00
0.062	0.00
0.069	0.00
0.076	0.00
0.085	0.00
0.094	0.00
0.105	0.00
0.117	0.00
0.130	0.00
0.144	0.00
0.160	0.00
0.178	0.00
0.198	0.00
0.220	0.00
0.245	0.00
0.272	0.00
0.303	0.00

Size (µm)	Volume In %
0.303	
0.337	0.00
0.374	0.02
0.416	0.08
0.463	0.17
0.515	0.26
0.572	0.31
0.636	0.36
0.707	0.38
0.786	0.39
0.874	0.39
0.972	0.38
1.080	0.37
1.201	0.39
1.335	0.42
1.485	0.49
1.651	0.60
1.835	0.75

Size (µm)	Volume In %
1.835	
2.040	0.93
2.268	1.14
2.522	1.36
2.804	1.59
3.117	1.81
3.466	2.03
3.853	2.25
4.284	2.46
4.763	2.67
5.295	2.88
5.887	3.10
6.545	3.33
7.277	3.59
8.090	3.87
8.995	4.17
10.000	4.49
11.118	4.79

Size (µm)	Volume In %
11.118	
12.361	5.04
13.742	5.22
15.279	5.30
16.986	5.23
18.885	5.01
20.996	4.65
23.343	4.15
25.953	3.54
28.854	2.88
32.079	2.20
35.665	1.57
39.652	1.04
44.085	0.62
49.013	0.33
54.492	0.16
60.583	0.08
67.355	0.06

Size (µm)	Volume In %
67.355	
74.884	0.08
83.255	0.11
92.562	0.14
102.909	0.16
114.413	0.11
127.202	0.05
141.421	0.01
157.230	0.00
174.806	0.00
194.347	0.00
216.071	0.00
240.225	0.00
267.078	0.00
296.933	0.00
330.126	0.00
367.029	0.00
408.057	0.00
	0.00

Size (µm)	Volume In %
408.057	0.00
453.672	0.00
504.385	0.00
560.767	0.00
623.453	0.00
693.145	0.00
770.628	0.00
856.772	0.00
952.546	0.00
1059.025	0.00
1177.408	0.00
1309.024	0.00
1455.352	0.00
1618.038	0.00
1798.910	0.00
2000.000	

An example of the typical *Results Report* is provided on the previous page. A brief description of each section is as follows:

- *The residual*-an indication of the quality of the fitted data in comparison to the measurement data. If the residual value is below 1%, a good fit is established. The value above 1% directs to the incorrect usage of refractive index, absorption value.
- *Distribution statistics*-calculations from the derived diameters. It is a method for defining mean values of particle size:
  - D (0.5) is the size in microns at which 50% of the sample is smaller and 50% is larger. This is known as the mass median diameter or the median of the volume distribution.
  - D (0.1) is the size of the particle below which 10% of the sample is located.
  - D (0.9) is the size of the particle below which 90% of the sample lies.
- *The span*-the measurement of the width of the distribution. If the distribution is narrower, the smaller the span is.
- *Concentration*-is the volume concentration calculated by Beer-Lambert's Law.
- *Obscuration*-amount of the laser light which is lost due to the sample introduction into the laser beam. An ideal range is from 3% to 20% depending on the sample used.
- *Distribution*-the type of the distribution which analysis uses.
- *Uniformity*-a measure of the absolute deviation from the median.
- *Specific Surface Area (SSA)*-the total particle area divided by the total weight.

4.4. Conclusions

The Malvern Mastersizer 2000 laser diffraction testing instrument is used to evaluate particle size distribution. This method has been used extensively in many industries including pharmaceutical, environmental, food, health, beauty, and others. The sample material is passed through a laser beam resulting in the laser light scattered at a wide range of angles. Detectors measure the intensity of light scattered at each position. A mathematical model (Mie or Fraunhofer Theory) is applied to generate a particle size distribution (Wang 2013). The final result is reported on an Equivalent Spherical Diameter Volume basis.

4.5. References

Barret EP, Joyner LG, Halenda PB (1951) The determination of pore volume and area distributions in porous substances, Journal of the American Chemical Society, 73(1), pp. 373-380.

Canham LT, in: L.T. Canham (Ed.) (2014) Handbook of Porous Silicon, Springer International Publishing.

Dian J, Macek A, Niznansk D, Nemec I, Vrkoslav V, Chvojka T, Jelínek I (2004) SEM and HRTEM study of porous silicon—relationship between fabrication, morphology and optical properties, Applied Surface Science, 238(1-4), pp. 169-174.

Goldstein JI, Newbury D, Echlin E, Joy P, Lyman DC, Lifshin CE, Linda Sawyer E, and Michael JR (2003) "Scanning Electron Microscopy and X-Ray Microanalysis", Kluwer Academic, New York.

Elia P, Nativ-Roth E, Zeiri Y and Porat ZE (2016) Determination of the average pore-size and total porosity in porous silicon layers by image processing of SEM micrographs, Microporous and Mesoporous Materials, (225), pp. 465-471.

McMullan D (1995) Scanning electron microscopy 1928–1965, Scanning, 17(3), pp. 175-185.

Newbury DE (1995) "Quantitative Electron Probe Microanalysis", National Institute of Standards and Technology, Gaithersburg, USA.

Nixon W (1998) History and Early Developments of the Scanning Electron Microscope within Cambridge University, Electron Microscopy, pp. 27-28.

Sailor MJ (2011) Porous Silicon in Practice Preparation, Characterization and Applications, first ed., Wiley-VCH.

Smith RL and Collins SD (1992) Porous silicon formation mechanisms, Journal of Applied Physics, 71(8), pp. R1-R22.

Stratton JA (2007) Electromagnetic theory, John Wiley & Sons, (33).

Wang XD, Cui ZX, Zhang HJ, Zheng X, Chen B and Wang ZS (2013) A new proof of Mie effect in light scattering, Optik, 124(23), pp. 6194-6196.

Chapter 5 Conclusions and Future work

5.1. Conclusions

This doctoral thesis studied synthesis, processing, and morphological properties of highly porous silicon (pSi) nanostructures, fabricated via anodisation and processed mainly by supercritical drying, followed by its possible applications.

Chapter 1 provided an introduction to the topic together with background information of the covered matter. The discovery of porous silicon by Uhlir at Bell Laboratories was accidental in the mid-1950s. He was trying to develop an electrochemical machine and instead formed pores in the silicon wafer. In the late 1980s, photoluminescence of porous silicon was then discovered by Leigh Canham at the Defense Research Agency in England. Furthermore, different formation routes of porous silicon were reported. This thesis focused on the "top-down" approach via electrochemical anodisation which enables high tunability of pore size and pore volume/porosity. On the other hand, large challenges are also presented, in porous silicon production, particularly the achievement of lateral homogeneity of the pSi layer. Based on the literature (Properties of pSi, Leigh Canham) it was found that the double anodisation cell, as used in this thesis, deliver the most uniform results. Last but not least, porous silicon offers very attractive properties for a variety of applications. In particular, this thesis focused on the types of porous silicon most useful for drug delivery applications, using a high pore volume of pSi and on the types for gas sensing, based on high surface areas of pSi.

In *Chapter 2*, the emphasis is on the fabrication and processing of porous silicon, with results, analysis and discussion. *The first section* provided information about the synthesis of pSi, based on electrochemical etching. In particular, the electrochemical etching and drying conditions that achieve both ultrahigh porosity and thick membrane structures suitable for silicon aerocrystal particle generation were identified. The main reason for implementing electrochemical etching is to achieve tunable properties of porous silicon. Mesoporous membranes with porosities exceeding 90% and surfaces areas in the range 425-549m^2/g have been achieved under these specific anodisation conditions, or via a two-step process of

anodisation plus subsequent chemical etching. Supercritical drying with carbon dioxide has shown to be beneficial over air-drying in preserving the highest pore volumes and surface areas generated by particular etching conditions. We have reported the highest pore volumes (4-5ml/g) achieved to date in mesoporous silicon membranes. Moreover, it was demonstrated that such silicon aerocrystals should support very high drug payloads in future microparticle and nanoparticle-based drug delivery formulations. This improves capabilities, improve patient comfort etc. Such drug loading studies are currently in progress.

The second section focused on the generation of pSi microparticles. Previous studies demonstrated that perforation etching can significantly improve the speed of comminution and yields of pSi nanoparticle generation from layers using BM or USF. Previously reported data suggested that ball milling (BM) is vastly superior to ultrasonication (USF) with regard to material throughput. Parameters such as pore size, surface area and pore volume had not however been previously investigated before and after processing. In this thesis, ball milling, a greater deterioration of these properties has been found in comparison to much more gentle processing, ultrasonication. It was shown that after a certain period of ultrasonication (hours), yields of porous silicon particles are increased at ultrahigh porosities, above 85 %. USF would therefore appear particularly attractive for applications, such as gas sensing that need silicon nanoparticles of very high surface areas (>500m^2/g).

The third section is dedicated to the effects of drying and humidity variations during storage. We established here that repeated drying steps during fabrication can significantly lower pore volume and thereby drug payloads. It was established here that if repeated drying steps are necessary during a fabrication process, such as ball-milling and ultrasonication, pore volume could be significantly lowered and thereby drug payload also. Differing from a gentle size filtering/selection sedimentation procedure, lengthy storage in the air can cause significant degradation of porosity due to the effect of humidity and air-drying. In this doctoral thesis, it was shown that the following order of fabrication/processing steps: anodisation-sonication-sedimentation-drug loading enables complete avoidance of drying and humid air storage induced structural damage, before drug loading.

Sedimentation and ultrasonic fragmentation are both feasible techniques for size-selecting/filtering classifying microparticles. Such “wet” techniques align best with applications that utilize SCD pSi suspensions. In this way, the harmful effects of drying or other

processing issues can be avoided. One such processing issue encountered was that the drying of SCD pSi suspension using the critical point drier the particles are smaller than the sample chamber mesh and during flushing, they are expelled from the system, resulting in a significant loss of material. The alternative option with the sedimentation of pSi suspension is the ability to claim the material and to preserve the porosity and surface area. The material is reclaimed via evaporation of the liquid. Furthermore, sedimentation in solvents, unlike metal sieve filtration, is a technique of size selection that can be used without the need to dry porous silicon particles created by wet electrochemical etching. In conclusion, filtration using metal sieve can introduce the contaminations of the sample as well as the loss of the material. Sedimentation is a moderate procedure which preserves the porosity and surface areas.

In this doctoral thesis, sedimentation for the size selection of microparticles below 10 microns is shown in both ethanol and DI water. Qualitative analysis of sedimentation has not been presented in any previous studies. Stokes' Law was implemented for calculations of the settling times and therefore compared to the experimental values. Findings were that sedimentation can provide a much tighter microparticle size distribution. This was especially achievable for oxidised pSi material after only 2 hours of processing.

Chapter 3 presents supercritical fluids and supercritical drying, the main drying technique used in this doctoral thesis. Shrinking and cracking happen when porous silicon is dried in air. The main property of interest in this chapter is the critical thickness of porous silicon: the maximum thickness that a layer of specific porosity and pore size distribution can withstand solvent evaporation without cracking. This can be calculated using the formula derived from the Kelvin equation, previously provided. Critical thickness depends on the following parameters: surface tension of the liquid, mechanical properties, porosity and pore size. This chapter studied the cracking of highly porous silicon layers (>90%) during drying. Layer thickness and also the drying liquid used has been examined, and have been demonstrated to be directly related to surface tension. Overall, SCD is a technique, which avoids the problems associated with the liquid to gas phase changes that are present in other methods.

Chapter 4 provides details on the characterisation techniques applied to porous silicon nanostructures, fabricated in this thesis. *Section 1*-Gas adsorption is the main characterisation

technique used to investigate pore size, pore volume/porosity and surface area. It is exclusively suited to the small pore structures: between 1 nm and 100 nm (Klobes et al. 2006). The values for pore size and pore volume/porosity obtained by gas adsorption are compared to the gravimetric method and software used such as JMicrovision 1.2.7. and ImageJ.

Section 2- elaborates on electron microscopy for pore morphology investigation of highly porous silicon nanostructures as well as the effect of air-drying and supercritical drying. It was concluded that the nanostructures can be thoroughly investigated and studied by SEM imaging as the pore structures and the surfaces can be explored. In this work, plan-view images were mainly used for studying the pores and cross-sectional images were used to estimate thicknesses of the membranes and compare it to gravimetric values.

Section 3- Image processing of SEM plan-view images can be utilized for the determination of pore size and porosity. The values obtained using the software are compared to the BET method as well as the gravimetric method.

Section 4-Particle size measurements. The Malvern Mastersizer 2000 laser diffraction testing instrument is used to evaluate Particle Size Distribution (PSD). The sample material is passed through a laser beam resulting in the laser light being scattered at a wide range of angles. The intensity of light scattered at that position is measured by detectors. A mathematical model (Mie or Fraunhofer Theory) is applied to generate a particle size distribution. The final result is reported on an Equivalent Spherical Diameter Volume basis. The results summarise that the particle size distribution has been shown as a function of the volume provided by the software. The further processing has provided a much tighter distribution. It was found that using a vortex-mixer improved the stability of the suspension before the measurement.

Chapter 6 contains Standard operating procedures (SOPs) regards process flows and principles of analysis.

5.2. Future work (Outlook)

This doctoral thesis provided a detailed approach to the fabrication of porous silicon membranes as well as the improvements and tunability of the nanostructures. The fabricated materials have been characterised using a variety of techniques and the possible applications have been proposed.

One of the future work ideas is based on using different silicon wafer doping such as n^+ wafers. Some of that work has already been started but not completed. In the case of these wafers, similar supercritical drying vs. air-drying is proposed to be performed. The main goal would be to split each sample into two and one half to subject to air-drying, where the second half was subjected to supercritical-drying. The aim is to achieve an ultrahigh porosity sample. BET analysis will be then performed to obtain the values for pore size, pore volume/porosity and surface area of both types of drying method.

Related to supercritical drying, the possible future work would be pore impregnation using supercritical fluid, liquid carbon dioxide. This would need further work on the chamber of the critical point dryer to achieve the desired size of the mesh, to be smaller than the particle size to stop them from escaping the chamber during the flushes.

Furthermore, pore impregnation of drugs into mesoporous silicon is planned to be performed. The used method would be melt loading and the chosen drug ibuprofen. It was already shown when pores are not impregnated, the porosity/pore volume and surface area are diminished during the ball-milling procedure. Contrary to this, if the pores are previously filled with a drug of choice and subsequently ball milled, porosity and surface area will be preserved as it was predicted.

Different surface chemistry modifications can also be done on the fabricated porous silicon membranes and they can be characterised using FTIR and EDX techniques. Furthermore, they can be investigated using a pump-probe spectroscopy/technique, such as exploring different optical properties such as transmittance, reflectance and to investigate the recombination times.

Chapter 6. Appendices

SEM microscopy

Process flow and principles of analysis:

- Ensure the Z stage (working distance) is set to 10.0
- Select 'in/out' on the SEM screen
- Select 'Data bar' and then ensure that 'spot size' has been selected on the SEM screen
- If using 25kV choose beam spot 3 (standard setting is beam spot 4)
- On edx monitor – open Inca software icon.
- Choose the 'point & ID' icon at bottom of the screen
- Go to Acquisition set up.
- Parameters: Live time=60 seconds; Process time=5; Spec range=0-20kV (if using 20kV, if using 10kV choose 0-10 range)
- Microscope set up.
- Look to see what the acquisition rate is.
- If either the acquisition rate or deadtime is out of spec you may need to change the spot size or AEM aperture. Try the spot size to start with e.g. to get the acquisition rate up to increase the spot size (If this then increases the dead time too much, adjust the spot size back down and try lowering the aperture setting(It is usually set on 6 for imaging – hence turn to 5.

  N.B. Ideally you need a total of around 240,000 counts for good reading. If the acquisition rate reads you may want to go back to the lifetime and adjust the time to compensate.
- Once the signal is optimised press the red stop button.
- To perform an EDX measurement: Choose 'Sample' and enter a sample name. N.B. If your sample has been pre-coated, ensure you tick the relevant box and specify the coating material.
- Choose 'Site of interest' Press the green go button and allow to run.